universiteit
▶▶hasselt
KNOWLEDGE IN ACTION

2015 | Faculty of Sciences

DOCTORAL DISSERTATION

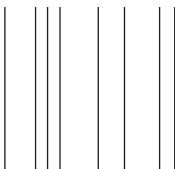# Single phase and composite multiferroic thin films and heterostructures from aqueous chemical solution deposition

Doctoral dissertation submitted to obtain the degree of
Doctor of Science: Chemistry, to be defended by

Nikolina Pavlovic

Promoter: Prof. Dr Marlies K. Van Bael | UHasselt
Co-promoters: Prof. Dr An Hardy | UHasselt
                      Prof. Dr Joke Hadermann | UAntwerpen

D/2015/2451/46

Chairman

Prof. dr. Karin CONINX

Dean Faculty of Sciences, UHasselt

Promoter

Prof. dr. Marlies K. VAN BAEL, UHasselt

Co-promoters

Prof. dr. An HARDY, UHasselt

Prof. dr. Joke HADERMANN, UAntwerpen

Members of the Jury

Prof. dr. Kristiaan TEMST, KULeuven

Prof. dr. Sebastiaan VAN DIJKEN, Aalto University

Dr. Alexander VOLODIN, KULeuven

Prof. dr. Jan D'HAEN, UHasselt

Acknowledgements

Words of gratitude... difficult to express in a moment like this. On the one hand it is because the gratitude is so big, words fall short. Gratitude because the thesis is finished, gratitude because your hard work and efforts have paid off and have not been in vain, gratitude because a new chapter in your life awaits you, and finally gratitude for all the help you received during your PhD. And herein lies the second problem with expressing my gratitude at this moment. There is the fear to forget people or to give people insufficient credit for what they have contributed, for the sociologist William Bruce Cameron said it well: "Not everything that counts can be counted, and not everything that can be counted counts." Therefore my gratitude towards you cannot, should not and may not be measured only in the amount of pages you read and corrected, the number of samples you analysed for me or the amount of times we sat together and discussed my results, although those things certainly directly contributed to this thesis. More important, yet so often forgotten, are the small words of encouragement when I felt down, the birthday parties we celebrated together, the drinks and ice creams we enjoyed on warm summer evenings, the quiet evenings we spent playing board games or eating copious amounts of food. They allowed me to continue my work with renewed vigour the next day and although no specific chapter or paragraph can be ascribed to them, exactly because of this, every sentence written in this thesis is the fruit of their encouragement. This thesis is a sentence longer, a graph nicer or a thought richer for every one of them!

First of all, I would like to thank my promoter prof. dr. Marlies Van Bael and copromoter prof. dr. An Hardy. As a complete foreigner the first steps in any new lab are always very difficult but Marlies, thanks to your gentle enthusiasm, your positivism and guidance this transition period was short and effortless and I quickly felt at home. An, words of gratitude are also in order for you, for I will never forget your critical thinking and your audacity to ask the most pertinent questions, as the search for answers to such questions always improves the research and the thesis. I would also like to thank you both for the input during

the many meetings we had, after such a session it was clear to me in which direction my research should proceed.

Secondly, I would like to thank the members of my PhD jury: prof. dr. Joke Hadermann, prof. dr Kristiaan Temst, prof. dr. Sebastiaan van Dijken, dr. Alexander Volodin and prof. dr. Jan D'Haen for their interest, useful suggestions and critical comments on my work. I greatly acknowledge the collaboration and help from prof. dr. Joke Hadermann with TEM characterization of my composite specimens. I would also like thank prof. dr. Kristiaan Temst for his constructive comments and fruitful discussions related to physical characterization of the materials. My deepest gratitude goes to prof. dr. Sebastiaan van Dijken for giving me the opportunity to stay at Aalto University to carry out SQUID measurements on my composite films. I would also like to thank Dr. Alexander Volodin for introducing me (C)AFM, PFM and MFM techniques and for his help with measurements. Big thanks are due to Prof. dr. Jan D'Haen for his collaboration during my PhD studies, especially for his critical comments and fruitful discussions on the experiments, papers and thesis.

I also acknowledge the financial support from COST Action SIMUFER to participate at many COST workshops organized during past years as well as my STSM at Aalto University. Thanks are also due to Prof. dr. Liliana Mitoseriu for her support and the way she led the SIMUFER project which resulted in one of the most successful COST Actions in its domain.

This brings me to my colleagues from the ICP group. Linny and Lize, thank you for enjoyable moments during dancing lessons and spa treatments. Christopher, thank you for interesting chats during conferences, travelling and AFM sessions and for your constructive criticism on the related work. Daan, Ken, Bertie, Kevin, Nick and Hanne I would like to thank you for your help, support and lab activities. Anke, I appreciate very much your straightforward attitude. Thanks for giving me a hand during the lab issues and your support. Sven, thanks for the time we spent on Balkan trip and the COST Workshop in Novi Sad. And above all, thank you for being a colleague and friend. Maarten, it was a pleasure to discuss with you on different topics: from politics and economics to research and everyday life and to hear your critical opinion. Thomas, technologically up-dated IPC group is your result. Ellen, thanks for the nice moments during the

COST workshops in Italy. Jonathan, thank you for chats about history, traveling and stories from Kenya. Giedrius and Andrius, I admire your pragmatic approach to life. Boaz, Gilles and Wouter, with your arrival a new era has begun in ICP group. You broke the mode with your positive attitude, motivation and approach to research, the lively atmosphere and team spirit which you maintain in the group. Fulya, Alexander and Dries, I wish you all a lot of success with your PhD!

The team from IMO. Bart, thank you for many SEM sessions and HT(-XRD) measurements, your patience to listen and explain. Thanks to Hilde and Christel, for their help with the sample preparations.

I would also like to express my gratitude to the TOES people, especially Elsy and Grete for their help with ICP measurement as well as to Ivo and Guy for their kind help and talks during everyday lab life.

Acknowledgements are also due to the colleagues outside of UHasselt for their involvement and contribution to this thesis. Hiwa, thank you very much for AES, RBS and SQUID measurements and long discussions on related results. Robert, I appreciate a lot your effort that you put in TEM characterization. Thanks to Dr. Qin for his help with SQUID measurements during my staying at Aalto University.

I would also like to express my sincere gratitude to prof. dr. Vladimir Srdic who was my supervisor at University of Novi Sad as well as to my colleagues. Thank you for having faith in me and for your continuous support all these years.

PhD life would have been very difficult in Diepenbeek without friends. I was great to be a part of international community with the "headquarter" in famous Nierstraat 8 (Like New York, just smaller!-as Filippo once said). And the list is long… Fortunato, Filippo, Emanuele, Donato, Consu, Lidia, Wiebke, Reza, Pia, Ariel, Amparo, Martin, Mirco, Ambily, Shreosi, Sammy, Aida, Farnoosh, Tanya, Wibren, Eva, Jimmy, Rafaela, Sarah, Lorenzo, Ahmad, Hamza, Roberto, Michele, Benjamin, Kayte, Iva, Jordan and many others. Thank you all guys for memorable moments, lovely dinners, birthday parties, BBQ time, excursions around Belgium, long walks, interesting talks…

List of abbreviations

AES	Auger electron spectroscopy
AFM	Atomic force microscopy
APM	Ammonia peroxide mixture
BFO	$BiFeO_3$
BSE	Back scattered electron
BTO	$BaTiO_3$
CFO	$CoFe_2O_4$
CSD	Chemical solution deposition
CVD	Chemical vapour deposition
DSO	$DyScO_3$
EBSD	Electron backscattered diffraction
FFT	Fast Fourier Transform
HAADF-STEM	High angle annular dark field STEM
LAO	$LaAlO_3$
LSAT	$(LaAlO_3)_{0.3}(SrAl_{0.5}Ta_{0.5}O_3)_{0.7}$
MBE	Molecular beam epitaxy
ME	Magnetoelectric
PLD	Pulsed laser deposition
RBS	Rutherford backscattering spectrometry
ICP-AES	Inductively coupled plasma atomic emission spectroscopy
RHEED	Reflection high energy electron diffraction
SEM	Scanning electron microscopy
SPM	Sulfuric acid peroxide mixture
STO	$SrTiO_3$
STEM	Scanning transmission electron microscopy
TEM	Transmission electron microscopy
T_C	Curie temperature
T_N	Néel temperature
HAADF-STEM	High angle annular dark field STEM
UHV	Ultra high vacuum
XRD	X-ray diffraction
YAO	$YAlO_3$
YMO	$YMnO_3$

Outline

Magnetoelectric multiferroics as materials with coexistence of two or more ferroic properties and coupling between the ferroic orders present not only the vast playground for different areas of fundamental research but they also have a great potential for memory and logic device applications. Offering possibilities towards miniaturization of electronic devices and at the same time increasing their performances, these multifunctional materials, especially in thin film form, have received enormous interest from the scientific community in the past decade.

However, multiferroic materials with room temperature functionalities still remain a challenge. Besides the weak magnetoelectric coupling, bismuth ferrite (BiFeO$_3$), currently the only known intrinsic multiferroic at room temperature is also facing issues with phase formation and thermal stability. Contradictory reports on phase purity and thermal stability of this compound have resulted in many open questions whereby some of them are related to the processing conditions of BiFeO$_3$ thin films at elevated temperature. On the other hand, the composite multiferroics combining ferroelectric and ferri/ferromagnetic phases are considered as a promising alternative to single-phase multiferroic, although the new compositions and structures that would result in a material with enhanced magnetoelectric properties are still appealing.

The question that we address throughout this work is how we can correlate synthesis, processing, structure and final properties of multiferroic materials.

The main aim of the work presented in this thesis was to deposit and investigate different single phase as well as composite multiferroic thin films and heterostructures using the aqueous chemical solution deposition method as cost-effective and easily accessible way. Furthermore, the additional aim was to contribute to understanding the phase formation and stability of BiFeO$_3$ film depending on different processing parameters where particular emphasis was placed on the appropriate choice of the underlying substrate. The second part of the conducted work aims for creating self-organized composite heterostructures with various constituent phases using the flexibility of solution chemistry and

further to investigate the potential of such solution-derived nanostructures in the field of multiferroics.

Chapter 1 gives a general introduction to multiferroic phenomena and materials. The first part of the chapter elucidates the basic aspects of magnetism and ferroelectricity, as parent properties of multiferroicity. Further discussion continues on different groups of single-phase (intrinsic) multiferroics and their characteristics with particular emphasis on $BiFeO_3$. At the end of the chapter, an overview of different forms of composite multiferroic structures and related properties is given.

Chapter 2 describes the most common techniques used for deposition of multiferroic thin films and heterostructures. Attention has been put on chemical solution deposition, since it was the main processing technique used to obtain thin films in Chapters 3, 4 and 5. A number of additional topics such as epitaxial film growth and self-assembly of composite multiferroic thin films are discussed.

Chapter 3 presents results on thermal stability of $BiFeO_3$ thin films obtained by aqueous chemical solution deposition. Effects of different processing parameters are investigated by varying annealing temperature and time, film thickness, Bi addition and Ti substitution. The film (in)stability at elevated temperatures is evaluated from the perspective of decomposition of $BiFeO_3$ phase and resulting secondary phase formation supported by a thorough structural and microstructural characterization.

Further study on the thermal stability of $BiFeO_3$ films presented in Chapter 4 discusses the role of various substrates and buffer layers in the $BiFeO_3$ phase stability at elevated temperatures in terms of film/substrates interactions and epitaxial phase stabilization. Furthermore, results of ferromagnetic measurements on epitaxial $BiFeO_3$ films are also presented and discussed.

Chapter 5 focuses on solution-gel derived self-assembled heterostructures of a two-phase system consisting of ferroelectric ($BaTiO_3$ or $BiFeO_3$) and magnetic ($CoFe_2O_4$) phases. A thorough structural and morphological investigation is correlated with the electrical and magnetic properties of the obtained films.

Contents

Contents

Chapter 1

Single phase and composite multiferroics

1.1 Introduction

Multiferroics are materials with a simultaneous presence of two or more ferroic properties (functionalities) in the same phase, i.e., ferromagnetism, ferroelectricity and ferroelasticity, as originally defined in 1994 [1]. Thus, multiferroics possess a spontaneous magnetization that can be switched by an applied magnetic field, while its spontaneous polarization can be switched by an applied electric field. Furthermore, interaction between the magnetic and electric polarization leads to additional functionalities of the material such as the magnetoelectric (ME) effect where an applied electric field controls the magnetization and vice versa, the polarization is controlled by a magnetic field [2]. The original definition of multiferroics is nowadays extended to one more ferroic functionality called ferrotoroidic order as well as to the materials with antiferroic behaviour and to multiphase materials such as composite multilayers and heterostructures [2-4]. Combining several properties and achieving additional functionalities multifunctional materials lead towards miniaturization of electronic devices in which a single component can perform more than one task [5].

In order to understand the phenomena underlying the multiferroic behavior, it is necessary to gain insight(s) in the ferroic orders as the parent properties of multiferroic materials. Although by the broader definition multiferroics can have several ferroic orders as illustrated in Figure 1, this section gives a general overview on two most important ones, (ferro)magnetism and ferroelectricity.
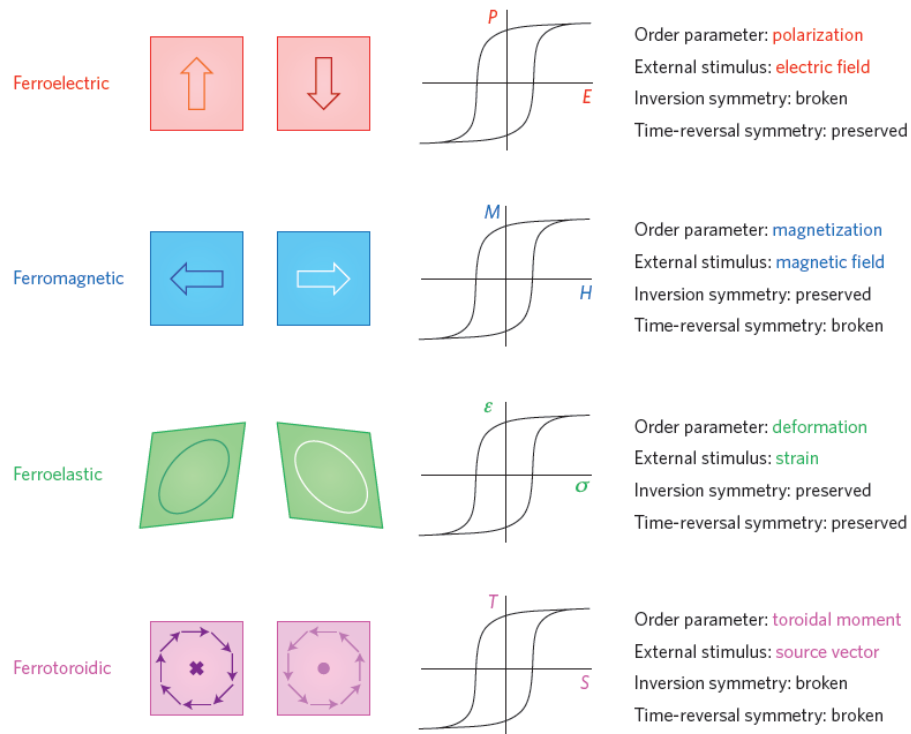
Figure 1.1: Schematic representation and hysteresis loops of four primary ferroic orders [6].

1.2 (Ferro)magnetism

Magnetic materials are those materials that can be attracted or repelled by a magnet and be magnetized themselves. The magnetic properties of materials are of atomic origin. Actually, magnetism in a material comes from the orbital motion and spin angular momentum of the electrons in the atoms. When a magnetic field H is applied to a material, the response of the material is called its magnetic induction, B. The relationship between B and H is a property of the material. The equation relating B and H is (in centimeter-gram-second (cgs) units)

$$B = H + 4\pi M \tag{1.1}$$

where M is the magnetization of the medium. The magnetization M is defined to be the magnetic moment per unit volume,

$$M = \frac{m}{V} \qquad \frac{emu}{cm^3} \tag{1.2}$$

M is a property of the material and depends on both individual magnetic moments of the constituent ions, atoms or molecules, and on how these dipole moments interact with each other [7]. However, the properties of a material are defined not only by the magnetization, or the magnetic induction, but also how these quantities vary with the applied magnetic field.

Now, with the very basics of magnetism introduced, it is possible to continue further with the characteristics of ferromagnetic materials. Ferromagnets and ferrimagnets are the materials that we usually call magnetic and which are attracted to a piece of iron or a permanent magnet. The strongest type of magnetism found in materials is ferromagnetism [8]. A ferromagnetic material undergoes a phase transition from a high-temperature phase that does not have a macroscopic magnetic moment to a low-temperature phase that has a spontaneous magnetization within one domain even without an external applied magnetic field.

The macroscopic magnetization is caused by the magnetic dipole moments of the atoms tending to align in the same direction, as shown in Figure 1.2. Above a certain critical temperature called the Curie temperature (T_C) ferromagnetic materials lose their spontaneous magnetization and become paramagnetic. In this high-temperature phase magnetic moments of the atoms are aligned randomly. As-prepared samples of ferromagnets usually have no net magnetization since the sum of all spontaneous magnetization vectors in the various distinctive areas or domains of the ferromagnet is zero due to their orientation in different directions.
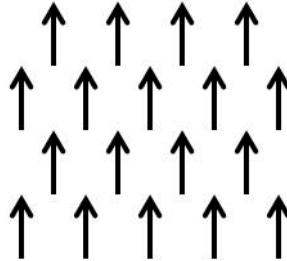
Figure 1.2: Ordering of the magnetic dipoles in ferromagnetic materials.

Ferromagnetism is found in the three transition metals such as Fe, Co, and Ni, alloys or intermetallic compounds containing Fe, Co and Ni and in a relatively few alloys which do not contain any ferromagnetic elements [9].

1.2.1 Domains

When a ferromagnet is cooled from a temperature above its Curie temperature in the absence of an applied magnetic field (H=0), the sample will initially seem to be non-magnetic and there will be very little evidence of it having large magnetization values. However, when an external magnetic field is applied, it is possible to change the magnetization from an initial value of zero to a saturation value by the application of a rather small magnetic field. The fact that the initial magnetization of a ferromagnet is zero, was explained by Weiss as domain formation [9]. In one single domain of magnetized crystal, where all magnetic moments line up in the same direction, the magnetization creates an internal field that tends to magnetize the sample in the opposite direction from its own magnetization, as in Figure 1.3a. This demagnetizing field (H_d) causes considerable magnetostatic energy. Magnetostatic energy can be reduced if crystal splits into several or many magnetic domains whereby with each division into smaller domains the magnetostatic energy of the crystal is decreasing, Figure 1.3b-c. Between adjacent domains there are boundaries or domain walls in which the local magnetization has different directions [9]. In bulk ferromagnetic materials they are about 100 nm in thickness and across this distance the direction of magnetization changes usually by either 180 or 90

degrees [7]. However, this splitting into smaller and smaller domains cannot continue indefinitely, because each wall formed in the crystal has a boundary energy per unit area, which adds energy to the system. Eventually an equilibrium domain size will be reached [9].
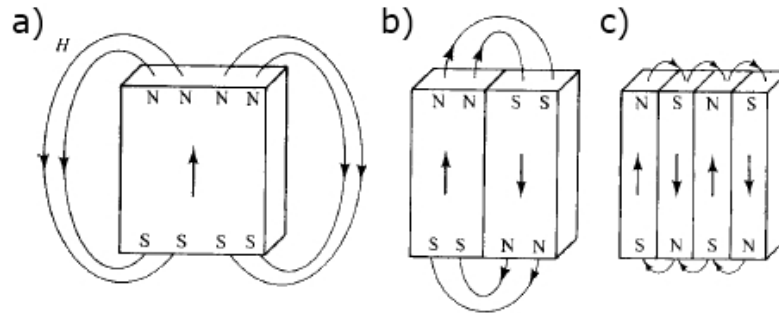
Figure 1.3: Division of a crystal into domains. Adapted from reference [9].

In these small regions of ferromagnetic materials all the magnetic dipoles are aligned parallel to each other resulting in net magnetization even without an external field. This magnetization is known as spontaneous magnetization. However, the magnetization vectors in different domains have different orientations, and the total magnetization averages to zero when a ferromagnetic material is in its demagnetized state. Application of an external magnetic field then causes all the domains to orient in the same direction.

1.2.2 Hysteresis loop

It is possible to determine the property of the material by studying the way in which magnetization varies with the magnetic field applied to the sample. The obtained B or M (H) curves are characteristic of the type of material.

Figure 1.4 shows the schematic of the general shape of the hysteresis loop for a ferromagnet. The key features are that the curve is not linear and the behavior is not reversible. At the beginning, the magnetic material starts at the origin in an unmagnetized state and no external magnetic field (i.e. $B = 0$ and $H = 0$). In this initial state, domains are arranged such that the magnetization averages to zero. With the gradually increasing external magnetic field in the positive

direction, magnetic induction follows the curve from $B=0$ to B_s. During this stage, those domains, in which spontaneous magnetization has the same orientation of the applied magnetic field, grow at the expense of the other magnetic domains with the displacement of the domain walls inside the material. For very low magnetic fields these displacements are reversible which explains the initial linear slope of the curve. At the point when induction reaches its maximum value, the saturation induction B_s, the induction is collinear with the applied magnetic field. In this condition all the magnetic dipoles within the material are aligned in the direction of the magnetic field. After saturation, magnetization M_s is constant and represents an intrinsic property of ferromagnet that is the same for any piece of particular compound, while B continues to increase because $B = H + 4\pi M$. When the external magnetic field H is decreased after saturation, the magnetic induction B follows a curve with higher values than the original curve owing to the irreversibility of the domain walls' motion. During this stage the moments will first return to the preferred crystallographic direction and as the field is decreased further, the domain wall will reform (or nucleate) and try to move. However, the induction of the ferromagnet does not return to zero by reducing H to zero since the residual induction B_r or retentivity remains inside of the material. Only by applying a sufficiently large magnetic field in the opposite direction known as the coercive field H_c, the induction can be returned to zero. Further application of a higher magnetic field causes saturation in the reverse direction and finally, reversing the external magnetic field once more leads to the completion of the B-H curve. The initial condition of zero magnetization at zero field can be achieved again by heating the materials past the Curie temperature to generate a new system of random magnetic domains [10].

.
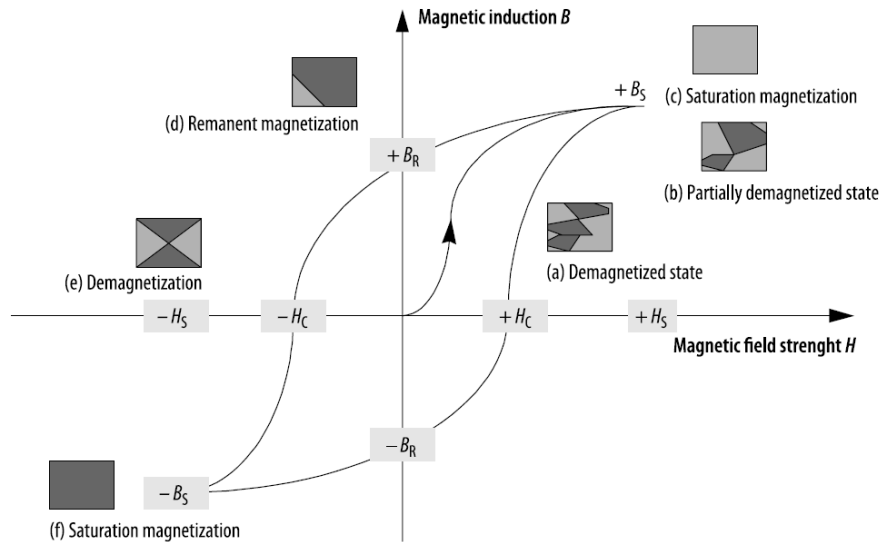
Figure 1.4: *B-H* hysteresis loop and change in domain structure during magnetization of a ferromagnetic material [10].

In ferromagnetic crystals there is a tendency of magnetization to align along certain preferred crystallographic orientations which can be explained by magnetocrystalline anisotropy. The preferred directions are called the 'easy' axes, since it is easiest to magnetize a demagnetized sample to saturation if the external field is applied along such a preferred direction. In both cases, easy axes and hard axes, the same saturation magnetization is achieved, but a much larger applied field is required to reach saturation along a hard axis than along an easy axis. Therefore, a lower energy configuration results from the magnetocrystalline anisotropy.

1.2.3 Ferromagnets vs. anti- and ferrimagnets

As discussed at the beginning of this chapter, more loose convention applies the term 'multiferroic' to materials that combine (anti)ferroelectricity not only with ferromagnetism but also with different types of magnetism. Thus, it is important for further discussion on multiferroic material to point to basics of

other types of magnetism (anti- and ferrimagnetism) and their relation with ferromagnetism.

Antiferromagnets

In antiferromagnetic materials, constituent atoms or ions possess magnetic dipole moments that are ordered in opposite directions to each other, as shown in Figure 1.6. In contrast to ferromagnets, here the moments on neighbouring atoms cancel each other. As a result, antiferromagnets have no net spontaneous magnetization. Their response to applied magnetic field is similar to that of paramagnetic materials, however the origin of the $M(H)$ is quite different from that of the Curie paramagnets, since the antiferromagnetic state is a long range ordered state. The term "weak ferromagnetism" is used to describe antiferromagnets with a small canting of the spins away from their antiparallel alignment. This results in a small net magnetization, usually at low temperature [11]. The spin arrangement of antiferromagnetic materials is not stable above a critical temperature, called the Néel temperature (T_N).

For instance, some of antiferromagnetic materials are chromium and manganese as well as transition metal oxides such as MnO, FeO, NiO, CoO, α-Fe_2O_3 and Cr_2O_3 [9].
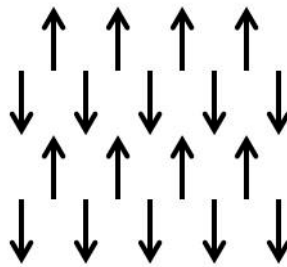
Figure 1.6: Ordering of the magnetic dipoles in antiferromagnetic materials.

Ferrimagnets

Ferrimagnetic materials are similar to antiferromagnetics at the atomic level because of dipoles aligned in opposite directions. What makes ferrimagnets different from antiferromagnets is that ferrimagnets have a net magnetization.

Ferrimagnets consist of two interpenetrating sublattices with opposite alignment of magnetic moments whereby the magnetization of one sublattice is greater than that of the oppositely oriented sublattice. The larger of the two moments tends to align with the applied magnetic field while the smaller moment aligns opposite to the field direction, see Figure 1.7. As a result, magnetic moments cancelation is incomplete in such a way that there is net magnetization that can be switched by an applied magnetic field, what makes them similar to ferromagnets. Ferrimagnetic materials become paramagnetic above a certain Curie temperature.

Most ferrimagnets are ionic solids. Ferrimagnetic materials include the cubic ferrites such as Fe_3O_4, $CoFe_2O_4$, $NiFe_2O_4$ but also γ-Fe_2O_3 (maghemite) and some garnets and alloys [9].
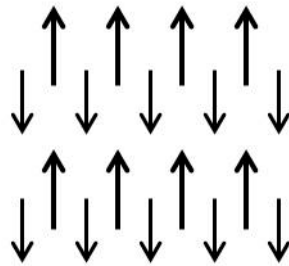
Figure 1.7: Ordering of the magnetic dipoles in ferrimagnetic materials.

Figure 1.8a schematically shows magnetization of para- and antiferromagnetic materials as a function of the externally applied field. For all these materials the $M(H)$ curves are linear. Quite large applied fields are required to cause rather small changes in magnetization, and no magnetization is retained after removal of the applied field.

Magnetization curves for ferri- and ferromagnets are schematically plotted in Figure 1.8b. Compared to the image in Figure 1.8a, it can be observed that in the case of ferri- and ferromagnets, much larger magnetization is obtained on the application of a much smaller external field. Here, as described before, magnetization saturates above a certain applied field. Furthermore, decreasing the field to zero does not reduce the magnetization of the material to zero due to remanent magnetization.
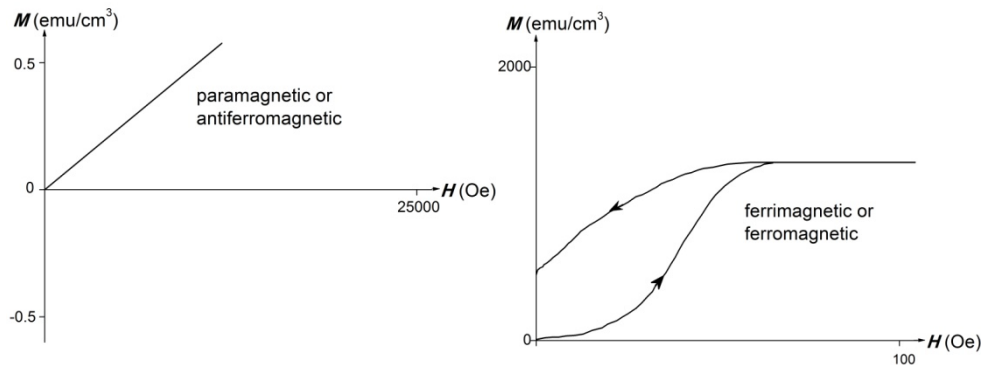
Figure 1.8: Magnetization curves for para- and antiferromagnets (left) and ferri- and ferromagnets (right). Adapted from reference [7].

The suitability of ferro- and ferrimagnetic materials for particular applications is determined largely from characteristics shown in their hysteresis loops. Thus, materials that are characterized by high saturation magnetization and large coercivity exhibiting square-shaped hysteresis loops are desirable for permanent magnets and magnetic recording and memory devices. The origin of the square shape is the large magnetocrystalline anisotropy [7]. In the case of magnetic date storage, advantages of the square hysteresis loops are that the remanent magnetization is close to the saturation magnetization, and that a well-defined applied field slightly greater than the coercive field will switch the magnetization direction. On the other hand, materials with high saturation magnetization and low coercivity exhibit narrow hysteresis loop that is easily cycled between two magnetization states. These materials are suitable for electromagnets and transformer cores where they must be able to reverse their direction of magnetization rapidly[7].

1.2.4 Magnetostriction

Magnetostriction describes the reversible dimensional change of a ferro/ferrimagnetic material when it is magnetized. The elastic change can be due to the motion and rotation of domain walls or coherent rotation of magnetization. Spontaneous magnetostriction occurs at the Curie temperature due to the reordering of magnetic moments. Field–induced magnetostriction consists of a change in volume or in shape during the process of magnetization,

or in the case of inverse magnetostriction, magnetization changes with an applied mechanical stress (tension or compression). In order to quantitatively characterize the magnetostrictive properties of the material, the dimensionless coefficient of linear change (fraction change in length) is used at a given magnetic field:

$$\lambda = \frac{\Delta l}{l} \qquad\qquad (1.3)$$

As the values for selected materials show, the magnetostriction at saturation can be positive, negative, or in some alloys at some temperature zero: magnetite $(+40 \times 10^{-6})$, permalloy (0), $CoFe_2O_4$ (-110×10^{-6}), $SmFe_2$ (-1560×10^{-6}), $TbFe_2$ $(+1753 \times 10^{-6})$, Terfenol D $(Tb_{0.3}Dy_{0.7}Fe_{1.93})$ $(+2000 \times 10^{-6})$ [9, 10].

1.3 Ferroelectrics

There is a lot of analogy between ferroelectric and ferromagnetic materials and their properties. The very name "ferroelectric" has been derived from this similarity, even though there is no ferro, i.e. iron constituent, in ferroelectrics as a major component. Thus the electric polarization, P, corresponds to the magnetization, M; the electric field, E, corresponds to the magnetic field, H and the electric displacement, D, corresponds to the magnetic flux density, B. A ferroelectric material has a spontaneous polarization which direction can be switched by an applied electric field, Figure 1.9. Like ferromagnets, ferroelectrics also have domains which correspond to regions of uniform and homogeneous spontaneous polarization. The appearance of these domains is to minimize the free energy when ferroic materials undergo a phase transition from a high-temperature symmetric phase to a low-temperature phase with a low symmetry. Furthermore, the hysteresis loop (polarization versus applied electric field) is very similar to the magnetic loop (magnetization versus applied magnetic field) one obtains for a ferromagnetic material. As a result, they also find applications in data storage [12, 13].
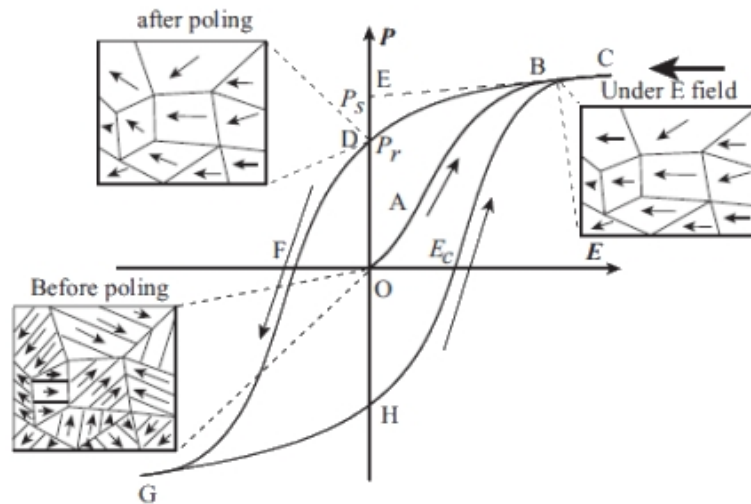
Figure 1.9: A typical ferroelectric hysteresis loop and corresponding domain reversal (polarization rotation). Adapted from reference [13].

Early work on ferroelectric materials was focused primarily on Rochelle salt, $KNa(C_4H_4O_6) \cdot 4H_2O$ [14]. Nowadays, the most studied family of ferroelectric oxides are the perovskites (from the mineral perovskite $CaTiO_3$). This is a very large family of materials which all have a composition of ABO_3, where A and B each represent a cation element or a mixture of two or more of such elements or vacancies. One of the first perovskite oxides identified as ferroelectric was $BaTiO_3$, Figure 1.10. At high temperatures, it has a paraelectric cubic perovskite structure characterized by Ba^{2+} as A cations, at the unit cell corners, a small cation Ti^{4+} (B cation) at the center of the cube and an oxygen ion at the center of each cubic face. At 393 K there is a structural distortion to a lower-symmetry tetragonal phase. This transformation is accompanied by the displacement of the Ti ion relative to the oxygen octahedron network. The shift of the Ti^{4+} ion from a centro-symmetric position creates the electric dipole moment which in turn generates the spontaneous polarization. Switching the spontaneous polarization by an applied electric field takes place on scales longer than the unit-cell scale and includes growth and shrinkage of domains through the domain walls' motion [15].
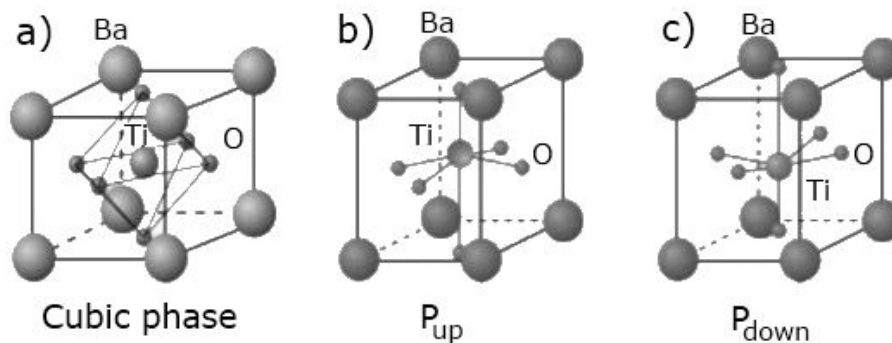
Figure 1.10: Crystal structure of the perovskite ferroelectric $BaTiO_3$: a) High-temperature, paraelectric, cubic phase; b) and c) Room-temperature, ferroelectric, tetragonal phases, showing the up and down polarization *P* variants [16].

Ferroelectrics form a subset of piezoelectric materials. Piezoelectricity in the materials is associated with two effects. Direct effect refers to the phenomenon when electric polarization is produced by mechanical strain whereas the converse effect is associated with the mechanical movement generated by the application of an electrical field. A lack of a center of symmetry is all-important for the presence of piezoelectricity. When the material lacks a center of symmetry, a net movement of the positive and negative ions with respect to each other (as a result of the stress) produces electric dipoles, i.e. polarization. The piezoelectric effect is linear and reversible, and the magnitude of the polarization is dependent on the magnitude of the stress and the sign of the charge produced is dependent on the type of stress (tensile or compressive) [12]. Some of piezoelectric materials with ferroelectric properties are $BaTiO_3$ and $Pb(Zr,Ti)O_3$ (PZT).

1.4 Single-phase multiferroics

1.4.1 History of multiferroics

The pioneering work on magnetoelectric and multiferroic materials dates back to the 50s and 60s of the twentieth century.

In 1957, the linear magnetoelectric effect was predicted to occur in antiferromagnetic Cr_2O_3 which was followed by experimental confirmation in the 1960s [2, 17, 18].

An early example of magnetoelectric switching was reported 50 years ago for nickel iodine boracites, $Ni_3B_7O_{13}I$, in which weak magnetic and electrical order set in simultaneously below 60 K [19]. Nickel iodine boracite is considered as a classical example (or the "Rochelle salt") of magnetic ferroelectrics on which many original ideas were tested.

Smolensky's group from Russia studied weakly ferromagnetic mixed perovskite oxides in which some of the d^0 B cations were replaced by magnetic d^n cations. The first synthetic ferromagnetic ferroelectric material was $(1-x)Pb(Fe_{2/3}W_{1/3})O_3$-$xPb(Mg_{1/2}W_{1/2})O_3$ in which the paramagnetic Mg^{2+} and W^{6+} ions cause ferroelectricity and the Fe^{3+} ions are responsible for magnetic properties [20].

1.4.2 Requirements for multiferroicity

The "renaissance" in the field of multiferroics arrived with the publication by Nicola Hill titled "Why are there so few magnetic ferroelectrics?" [11]. Here, the author analyzes the scarcity of ferromagnetic ferroelectric coexistence from the viewpoint of fundamental physics. In her analysis, emphasis is on oxide perovskites and it is not related to magnetic ferroelectric fluorides and oxyflourides which are not so rare in nature [Scott11].The paper triggered an enormous research effort on multiferroics, theoretical as well as practical (experimental) in physics, chemistry and materials science where the discovery of the novel materials with enhanced multiferroic properties became the goal. In order to understand the requirements for some materials to be multiferroic and more importantly, to be able to tailor a new one, it was necessary to gain insight into the structure and crystalline chemistry of these materials.

There are hundreds of magnetic materials with a perovskite structure and there are hundreds of ferroelectric perovskites but materials with coexistence of these two orders are very rare [21]. As mentioned in the previous section, polarization in ferroelectric perovskite materials is mainly the result of a displacement of the B cations relative to the oxygen cage. One thing that is common for the majority of perovskite ferroelectrics is the fact that the B cations are in their d^0 state. As

the lowest unoccupied energy levels, d states tend to hybridize with O $2p$ ions resulting. This may be beneficial to shift the B cation from the center of the oxygen cage towards one (or three) oxygen(s) to form strong covalent bonds with this particular oxygen(s).Some of the examples of the B cation being in the d^0 state in perovskite ferroelectrics are Ti^{4+}, Zr^{4+}, Nb^{5+}, W^{6+}, etc. On the other hand, the origin of magnetism lies in the presence of localized electrons, mostly in the partially filled d or f shells of transition-metal or rare-earth ions, which have a corresponding magnetic moment whose interaction leads to different magnetic orderings. Thus, it looks like coexistence of ferroelectricity and ferromagnetism in perovskites is hardly achievable since the prerequisites are mutually exclusive. Since the microscopic origin of magnetism is essentially the same in all magnets it is the origin of the ferroelectricity that conditions different types of multiferroics.

In order to circumvent the mutual exclusion described above, various attempts have been made to introduce ferroelectricity into magnetic materials. Based on different sources of ferroelectricity, most researchers have adopted four main approaches to try and make better magnetoelectric materials: the lone pair effect, charge ordering, geometric frustration or magnetic ordering [4, 21-23]. Generally, in multiferroics in which one of the first three mechanisms (lone pair effect, charge ordering, geometric frustration) occurs, ferroelectricity and magnetism now have a different origin and some of these materials have phase transition temperatures above room temperature which is important from an application point of view. However, the coupling between their ferroelectricity and magnetism is usually rather weak. Therefore, the materials challenge for these three groups of multiferroics is to keep all their positive features, but enhance this coupling [21]. In the next paragraphs, a short overview of the main characteristics of each of the four mechanisms as well as representative multiferroic compounds is given.

Multiferroics with lone pairs are materials with Bi^{3+} and Pb^{2+} cations which have two outer $6s$ electrons that do not participate in chemical bonds. These electrons known as lone pairs give high polarizability to the corresponding ions which is the condition required for ferroelectricity in the classical description. From a microscopical point of view, ordering of these lone pairs in one direction may

create local dipoles as illustrated in Figure 1.11, which can explain the origin of ferroelectricity in compounds such as $BiFeO_3$ or $BiMnO_3$ [11, 24, 25].

The 'geometric' mechanism of inducing ferroelectricity is explained with the example of hexagonal $YMnO_3$ [26]. Here, the tendency to reach closer packing causes tilting of rigid MnO_5 polyhedra with a magnetic Mn^{3+} remaining at the center, Figure 1.11. This tilting leads to the formation of dipoles by Y-O pairs and a net electric polarization.

In multiferroics with charge ordering certain 'non-centrosymmetric' arrangements of ions induce ferroelectricity in magnetic materials. This mechanism is often observed in transition metal compounds, especially those containing transition metal ions with different valences. In these systems the coexistence of inequivalent sites with different charges, and inequivalent (long and short) bonds, leads to ferroelectricity, Figure 1.11 [27]. An example of a multiferroic material that belongs to this group is $LuFe_2O_4$ [28].
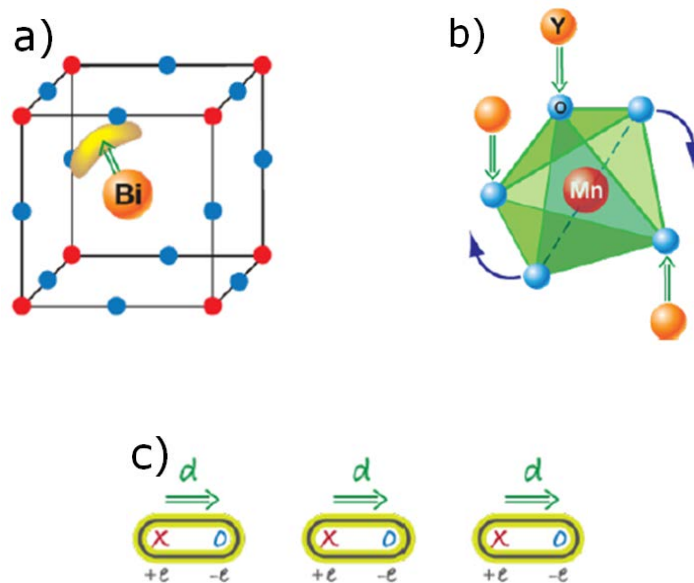
Figure 1.11: Different microscopic mechanisms found in multiferroics. a) Lone pair effect in $BiFeO_3$ where the ordering of lone pairs (yellow "lobes") of Bi^{3+} ions (orange), contributes to the polarization (green arrow). b) The "geometric" mechanism of generation of polarization in $YMnO_3$ where Y-O bonds form dipoles (green arrows). c) In charge ordered systems, the coexistence of inequivalent sites with different charges, and inequivalent (long and short) bonds, leads to ferroelectricity [29].

In the last, fourth group of multiferroics, ferroelectricity is induced by the magnetic ordering with the broken inversion symmetry [22]. Compared with materials in the previous three groups, polarization in these materials is much smaller but coupling between ferroelectricity and magnetism is stronger. Multiferroics with ferroelectricity due to magnetic ordering are $TbMnO_3$ and $TbMn_2O_4$ [30, 31].

1.4.3 Single-phase multiferroics and magnetoelectrics

From a technological point of view, besides the simultaneous presence of ferroelectric and magnetic ordering in single-phase multiferroic materials, the coupling between these two orderings is even more interesting. Magnetoelectric coupling (ME) typically refers to the linear magnetoelectric effect manifested as the control of polarization P through an applied magnetic field H (direct ME effect) or the control of magnetization M through an applied electric field E (converse ME effect) [2].

The magnetoelectric coefficient a for single-phase materials can be expressed as:

$$\alpha = \frac{P}{H} = \frac{M}{E} \tag{1.4}$$

However, magnetoelectric coupling is a more general and widespread phenomenon that can occur in any material which is both magnetically and electrically polarizable, for example in paramagnetic ferroelectrics [4]. It may arise directly between the two order parameters, or indirectly via strain. Strain-mediated indirect magnetoelectric coupling can occur in two-phase systems, where the magnetic and electrical order parameters appear in two separate but intimately connected phases which will be discussed later.

The overlap between different physical properties leading to magnetoelectric multiferroics is shown schematically in Figure 1.12. Only a small subgroup of all magnetically and electrically polarizable materials is either ferromagnetic or ferroelectric and fewer still simultaneously exhibit both order parameters forming subgroup of multiferroics. However, only in some multiferroic materials

electric field can control magnetization or magnetic field can change polarization which classifies them as magnetoelectric multiferroics.
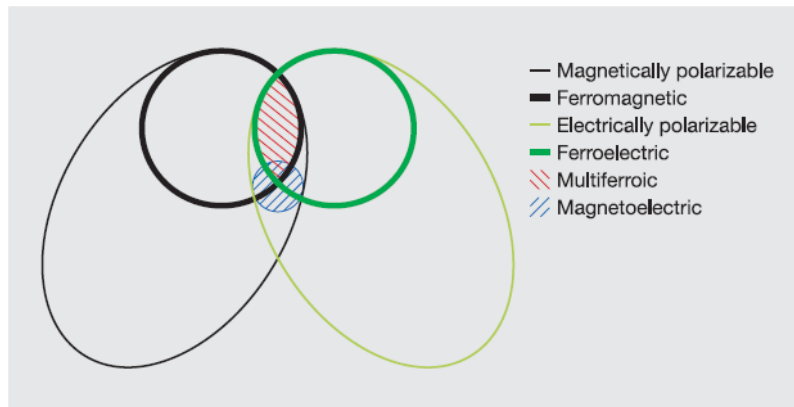
Figure 1.12: The relationship between multiferroic and magnetoelectric materials [4].

1.4.4 Bismuth ferrite BiFeO$_3$

BiFeO$_3$ is probably the only room temperature multiferroic (ferroelectric and antiferromagnetic) discovered so far which can explain the enormous interest in this material and the very intensive research in the past decade [32]. The bulk single crystal of BiFeO$_3$ has a rhombohedral unit cell, built with two distorted perovskite blocks connected along their body diagonal or pseudocubic [111] and belongs to the space group $R3c$, Figure 1.13 [33]. In this structure the two oxygen octahedra of the cells connected along the ⟨111⟩ are rotated clockwise and counterclockwise around the ⟨111⟩ by ±13.8° and the Fe-ion is shifted by 0.135 Å along the same axis away from the oxygen octahedron center position. Lattice parameters are determined to be a_{hex}=5.57874 Å and c_{hex}=13.8688 Å at room temperature [33]. The structure can also be described in terms of a simple cubic perovskite cell with a rhombohedral distortion, having a pseudo-cubic lattice constant of a_c=3.965 Å and a distortion angle of α=0.6° [33, 34].

The ferroelectric state is realized by the hybridization between the two 6s electrons in Bi with the surrounding oxygen ions leading to a large displacement of the Bi cations relative to the oxygen octahedral. As a result of this atomic

arrangement, the polarization lies along the ⟨111⟩ leading to the formation of eight possible polarization variants [33, 34]. The ferroelectric order of $BiFeO_3$ has a transition temperature well above room temperature, i.e. T_C~1103K [35]. The early ferroelectric measurements of bulk samples yielded to rather small polarization of 6.1 µC cm^{-2} [36].
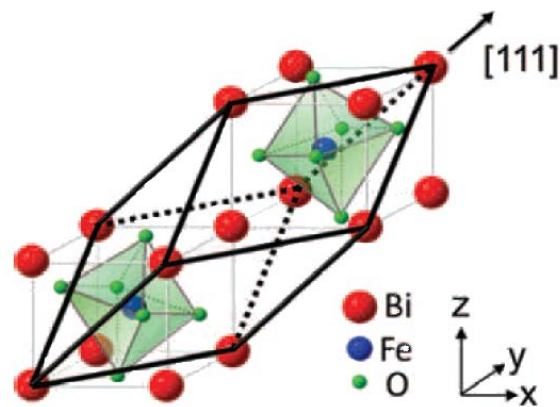
Figure 1.13: Schematic drawing of the crystal structure of $BiFeO_3$ (space group: *R*3*c*). Two distorted perovskite blocks are connected along [111] direction to build rhombohedral unit cell [37].

In terms of magnetic properties bismuth ferrite is a G-type antiferromagnet with a Néel temperature of ~ 673K [38]. The G-type spin configuration is schematically illustrated in Figure 1.14a where the Fe magnetic moments are coupled ferromagnetically within the pseudocubic (111) planes and antiferromagnetically between adjacent planes showing the nearest neighbour Fe moments aligned antiparallel to each other. However, theoretical calculations showed that symmetry permits a small canting of the moments in the structure in $BiFeO_3$ films resulting in a weak net ferromagnetic moment, see Figure 1.14b [39]. On the other hand, $BiFeO_3$ possesses a spiral spin structure in which the antiferromagnetic axis rotates through the crystal with a period of ~620 Å [40]. This spin structure was found to be incommensurate with the structural lattice and superimposed on the antiferromagnetic order leading to a cancellation of the macroscopic magnetization [39].
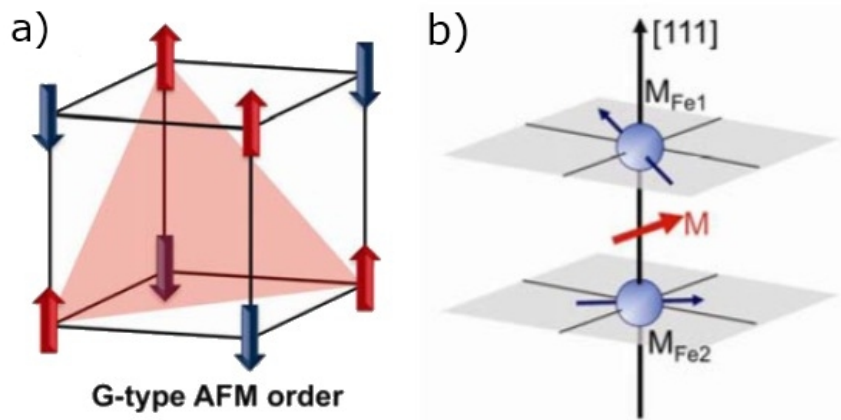
Figure 1.14: a) A schematic illustration of the G-type antiferromagnetic order in BiFeO₃. b) A predicted small canted moment emerges as a consequence of a spin–orbit interaction: two iron magnetic moments rotate in the (111) plane so that there is a resulting spontaneous magnetization, M [41].

A trigger for the enormous research on $BiFeO_3$ films was the paper published by Wang et al. in 2003 where enhanced properties of heteroepitaxially constrained thin films of BFO [42] were reported. Structural analysis of the films suggested differences between films (with a monoclinic structure) and bulk single crystals (with a rhombohedral structure). Furthermore, they reported enhancement of the polarization up to ~60 μC cm^{-2} at room temperature and enhanced thickness-dependent magnetism compared to bulk samples ascribing them to epitaxial strain [42].

However, some studies proposed a different origin of this enhanced magnetism like the presence of magnetic secondary phases (γ-Fe_2O_3) which was further elaborated by linking processing parameters during the growth of the BFO thin films with secondary phase appearance [43, 44]. Besides the magnetic origin that is still debatable due to contradictory results in the literature, phase formation and phase stability of BFO, especially issues with formation of secondary phases and thermal stability, is a field with many open questions [45-47].

Furthermore, the high electrical conductivity of $BiFeO_3$ materials is one of the obstacles for its practical application [32]. The origin of the high leakage current has been attributed to the presence of secondary phases like mullite type

$Bi_2Fe_4O_9$ and sillenite type $Bi_{25}FeO_{40}$, and to the defects in the crystal structure, such as oxygen vacancies caused by reduction of Fe^{3+} to Fe^{2+} ions and volatilization of Bi_2O_3 [48-51]. One of the approaches that have been adopted to stabilize BFO phase is partial substitution of A or B-site in the perovskite structure [48]. Thus, La substitution for the Bi site or Ti substitution of the Fe site has been proven to reduce conductivity in bismuth ferrite ceramics and thin films [48, 51, 52].

$BiFeO_3$ phase stability

Secondary phases like $Bi_2Fe_4O_9$ and $Bi_{25}FeO_{39}$ or $Bi_{46}Fe_2O_9$ usually accompany bismuth ferrite [45-47, 53]. Although a lot of research has been carried out on the BFO system and issues with secondary phases are often reported, the various literature reports dealing with the thermal stability of bismuth ferrite and the reasons for the appearance of these parasitic phases are still contradictory [45-47, 53-57]. Early works on the solid state synthesis of bismuth ferrite suggest that its decomposition into the starting oxides Bi_2O_3 and Fe_2O_3 [54] or $Bi_2Fe_4O_9$ [53] during thermal treatment is the consequence of the evaporation of bismuth oxide [53, 54]. In more recent papers, Morozov et al. [45] associate difficulty to obtain a single phase material to the changing equilibrium composition of bismuth ferrite upon temperature increase, while Palai et al. [56] emphasize that the $BiFeO_3$ phase is thermodynamically metastable in air. The latter authors [56] as well as Arnold et al. [58] report decomposition around 820°C into an iron rich $Bi_2Fe_4O_9$ and a liquid phase suggesting that the rate of decomposition can be affected by several different parameters including the ratio of surface to bulk volume, the annealing time at constant temperature, heating rate, surface defects, porosity and grain size, etc. During neutron diffraction measurements Palewicz et al. [59] noticed that part of the BFO sample transformed to the new $Bi_2Fe_4O_9$ phase at 700°C. In their comprehensive study of BFO phase stability, Valant et al. [47] pointed out that the purity of the starting materials is a crucial parameter for obtaining single phase bismuth ferrite since the presence of small amounts of impurities leads to the formation of a significant amount of secondary phases. According to the latter, Al_2O_3 or SiO_2 impurities enhance the formation of secondary phases during solid-state synthesis, since Al_2O_3 and SiO_2 have a higher solubility in $Bi_2Fe_4O_9$ and $Bi_{25}FeO_{39}$, respectively than in $BiFeO_3$. Selbach et al. [46] report that $BiFeO_3$

21

decomposes into $Bi_{25}FeO_{39}$ and $Bi_2Fe_4O_9$ in a temperature interval from 450° to 770°C under ambient atmosphere while above this interval till 930°C $BiFeO_3$ is thermodynamically stable and corroborate their findings with thermodynamic explanations. Decomposition at temperatures higher than 770°C is therefore related to chemical incompatibility between $BiFeO_3$ and the supporting materials it is in contact with during processing, like Al_2O_3 or SiO_2 based substrates [57]. In this case, alumina or silicon substrate at the contact surface with BFO sample can act like impurities [47] initiating an interface reaction which results in a higher amount of Bi-rich and Fe-rich secondary phases in $BiFeO_3$ ceramics [57] as evidenced during some experimental studies [60, 61].

The aforementioned studies have mainly focused on the conventional solid state synthesis, as a method for the preparation of single crystals, powders and ceramics. However, the different processing conditions between bulk ceramics and thin films could cause differences in phase stability, decomposition behavior and formation of secondary phases. Furthermore, synthesis parameters known to influence the phase formation and stability of the material differ between preparation methods and state of matter. Therefore, here we study thin films.

1.5 Composite multiferroics

Practical application of single phase multiferroics is limited by their scarcity at room-temperature and very weak magnetoelectric (ME) coupling (typical values in SI units are ca. 10^{-9}–$10^{-11}\,sm^{-1}$) [2, 62]. In order to circumvent the limitations of intrinsic multiferroics, an alternative approach is found in the form of composite materials which combine ferroelectric (e.g. perovskite $BaTiO_3$ [63-68], $PbTiO_3$ [69], $Pb(Zr,Ti)O_3$ [70-73], $BiFeO_3$ [74-78] and the ferri/ferromagnetic phase (e.g., spinel $CoFe_2O_4$ [63-65, 67-70, 74, 75, 77, 78] and $NiFe_2O_4$ [66, 71, 73]). In multiferroic composites, neither of the constituent phases has magnetoelectric behaviour, but the interaction between constituent phases can generate remarkable magnetoelectric effects, Figure 1.14 [2, 79].
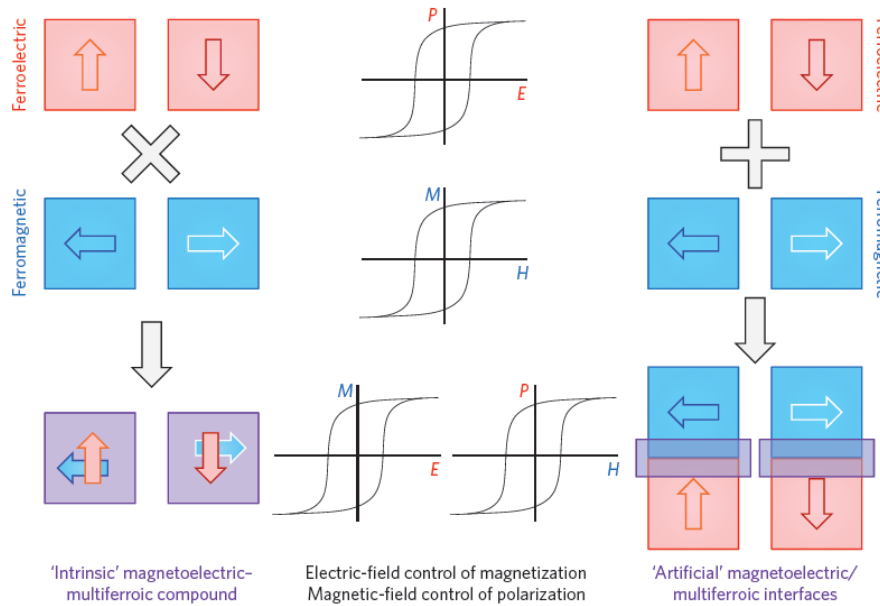
Figure 1.14: Schematic representation of an 'intrinsic' (that is, single phase) multiferroic compound (left) and an 'artificial' multiferroic interface (right). In both systems, ferromagnetic and ferroelectric orders may coexist and influence each other through a magnetoelectric coupling [6].

According to the original definition, the composite ME effect is a result of the product of the magnetostrictive effect (magnetic/mechanical effect) in the magnetic phase and the piezoelectric effect (mechanical/electrical effect) in the ferroelectric phase [79, 80]:

$$\text{Direct ME effect} = \frac{\text{magnetic}}{\text{mechanical}} \times \frac{\text{mechanical}}{\text{electrical}} \qquad (1.5)$$

$$\text{Converse ME effect} = \frac{\text{electrical}}{\text{mechanical}} \times \frac{\text{mechanical}}{\text{magnetic}}$$

In these systems indirect magnetoelectric coupling occurs via a strain mechanism between the ferroelectric and ferromagnetic materials. To ensure better strain-mediated magnetoelectric coupling through more intimate contact between the constituents, two-phase multiferroics with different geometries

23

have been developed. Based on dimensional self-connectivity of constituent phases, classification of multiferroic composites includes three main forms: composites denoted as 0-3 when particles (0D) of one phase are embedded in the matrix (3D) of another phase, then 2-2 composites which include layered structures and 1-3 composites which comprise of vertical heterostructures (1D) embedded in a matrix (3D), Figure 1.15 [81]. Multiferroic particulate composites are typical for bulk ceramics obtained by solid state synthesis [82, 83]. Composite multiferroic films mainly appear in the form of multilayers or self-organized nanostructures. Multilayer heterostructures consist of layers of ferroelectric and ferro/ferrimagnetic phases alternately deposited. Multilayers exhibit weak magnetoelectric coupling due to the clamping effect (in-plain constraint effect) of the single-crystal substrate on the ferroelectric phase. In this in-plane interfacial geometry the ferroelectric phase can impart only a limited amount of strain resulting in lower magnetic induced polarization [84, 85].
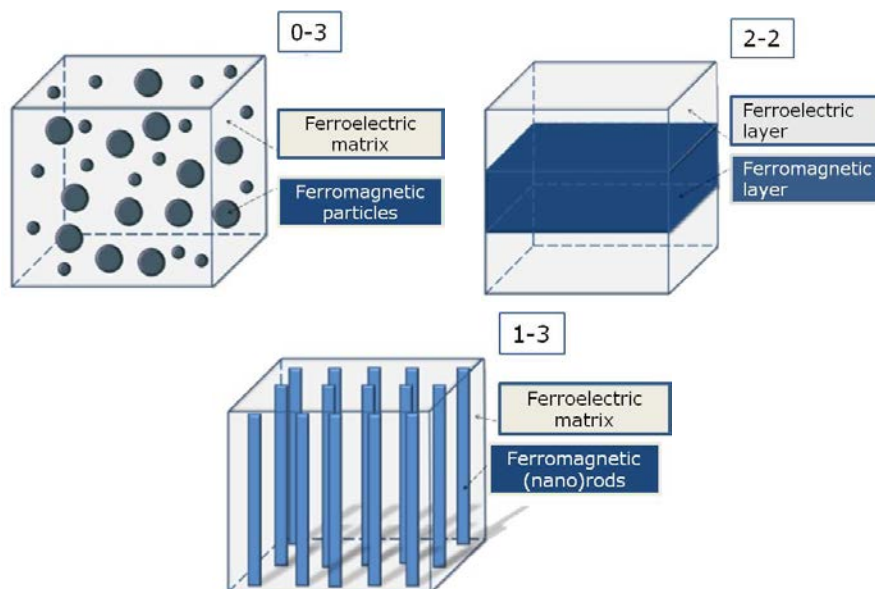
Figure 1.15: Schematic representation of 0-3, 2-2 and 1-3 type connectivity in composite materials. Adapted from [83].

In the case of self-assembled heterostructures, one material spontaneously forms nanodots and/or nanopillars (nanorods) or nanoparticles embedded in a matrix of another material [65, 66, 68, 75, 77, 86, 87]. The theoretical as well as experimental results revealed that 1-3 type vertical heterostructures could exhibit large ME response which is even larger than that in their bulk counterparts if there is no leakage current problem [68, 85]. Magnetoelectric coupling and the properties of the self-assembled films with three-dimensional epitaxy strongly depend on the morphologies and elastic interaction between the FE and the FM phases [68, 77, 88, 89].

In terms of the magnetoelectric effect, composites in laminate thick-film geometry obtained a magnetoelectric voltage coefficient up to 4680 mV cm^{-1} Oe^{-1} while the 2-2 thin film composites were not able to produce magnetoelectric voltage coefficients above a few tens of mV cm^{-1} Oe^{-1}. Vertical nanostructured composites exhibit an ME coefficient, α_E, up to 100 V cm^{-1} Oe^{-1} [90].

Magnetoelectric thin films with direct ME effect i.e. when the magnetic field controls electric polarization have potential applications as micro-devices in sensors, transducers, filters, oscillators, phase shifters, and so on. On the other hand, controlling magnetization switching or domain structure in a magnetic material directly by applying an electric field can offer interesting possibilities for novel potential ME devices such as memories, spintronic devices and electrically tunable microwave devices [80, 90, 91].

References

[1] H. Schmid, Multi-ferroic magnetoelectrics, Ferroelectrics, 162 (1994) 317-338.

[2] M. Fiebig, Revival of the magnetoelectric effect, Journal of Physics D-Applied Physics, 38 (2005) R123-R152.

[3] H. Schmid, in: M. Fiebig, V. Eremenko, I.E. Chupis (Eds.) Magnetoelectric Interaction Phenomena in Crystals, Kluwer Academic Publishers, Dordrecht, Netherlands, 2004.

[4] W. Eerenstein, N.D. Mathur, J.F. Scott, Multiferroic and magnetoelectric materials, Nature, 442 (2006) 759-765.

[5] N.A. Spaldin, M. Fiebig, The renaissance of magnetoelectric multiferroics, Science, 309 (2005) 391-392.

[6] M. Bibes, Nanoferronics is a winning combination, Nat. Mater., 11 (2012) 354-357.

[7] N.A. Spaldin, Magnetic Materials: Fundamentals and Device Applications, in, Cambridge University Press, United Kingdom, 2003.

[8] M. McElfresh, Fundamentals of Magnetism and Magnetic Measurements, in, Quantum Design, 1994.

[9] B.D. Cullity, C.D. Graham, Introduction to Magnetic Materials, second ed., Wiley, New Jersey, 2009.

[10] F. Cardarelli, Magnetic Materials, in: Materials Handbook, Springer, 2008.

[11] N.A. Hill, Why are there so few magnetic ferroelectrics?, J. Phys. Chem. B, 104 (2000) 6694-6709.

[12] G.H. Haertling, Ferroelectric ceramics: History and technology, J. Am. Ceram. Soc., 82 (1999) 797-818.

[13] L. Jin, F. Li, S.J. Zhang, Decoding the Fingerprint of Ferroelectric Loops: Comprehension of the Material Properties and Structures, J. Am. Ceram. Soc., 97 (2014) 1-27.

[14] J. Valasek, Piezoelectric and Allied Phenomena in Rochelle Salt, Physical Review, 17 (1921) 475-481.

[15] K.M. Rabe, M. Dawber, C. Lichtensteiger, C.H. Ahn, J.M. Triscone, Modern Physics of Ferroelectrics: Essential Background, in: K.M. Rabe, C.H. Ahn, J.M. Triscone (Eds.) Physics of Ferroelectrics: A Modern Perspective, Springer Berlin Heidelberg, 2007, pp. 1-30.

[16] C.H. Ahn, K.M. Rabe, J.M. Triscone, Ferroelectricity at the nanoscale: Local polarization in oxide thin films and heterostructures, Science, 303 (2004) 488-491.

[17] D.N. Astrov, The magnetoelectric effect in antiferromagnetics, Sov. Phys. JETP, 11 (1960) 708-709.

[18] I.E. Dzyaloshinskii, On the magneto-electrical effects in antiferromagnets, Sov. Phys. JETP, 10 (1959) 628-629.

[19] E. Ascher, H. Rieder, H. Schmid, H. Stossel, Some properties of ferromagnetoelectric nickel-iodine boracite $Ni_3B_7O_{13}I$, J. Appl. Phys., 37 (1966) 1404-&.

[20] G.A. Smolenskii, V.A. Isupov, A.I. Agranovskaya, New ferroelectrics of complex composition of the type A22+(BI3+BII5+)O-6 .1, Soviet Physics-Solid State, 1 (1959) 150-151.

[21] D.I. Khomskii, Multiferroics: Different ways to combine magnetism and ferroelectricity, J. Magn. Magn. Mater., 306 (2006) 1-8.

[22] S.W. Cheong, M. Mostovoy, Multiferroics: a magnetic twist for ferroelectricity, Nat. Mater., 6 (2007) 13-20.

[23] R. Ramesh, N.A. Spaldin, Multiferroics: progress and prospects in thin films, Nat. Mater., 6 (2007) 21-29.

[24] P. Baettig, C. Ederer, N.A. Spaldin, First principles study of the multiferroics $BiFeO_3$, Bi_2FeCrO_6, and $BiCrO_3$: Structure, polarization, and magnetic ordering temperature, Physical Review B, 72 (2005).

[25] R. Seshadri, N.A. Hill, Visualizing the role of Bi 6s "Lone pairs" in the off-center distortion in ferromagnetic $BiMnO_3$, Chem. Mater., 13 (2001) 2892-2899.

[26] B.B. Van Aken, T.T.M. Palstra, A. Filippetti, N.A. Spaldin, The origin of ferroelectricity in magnetoelectric $YMnO_3$, Nat. Mater., 3 (2004) 164-170.

[27] D.V. Efremov, J. Van den Brink, D.I. Khomskii, Bond-versus site-centred ordering and possible ferroelectricity in manganites, Nat. Mater., 3 (2004) 853-856.

[28] N. Ikeda, H. Ohsumi, K. Ohwada, K. Ishii, T. Inami, K. Kakurai, Y. Murakami, K. Yoshii, S. Mori, Y. Horibe, H. Kito, Ferroelectricity from iron valence ordering in the charge-frustrated system $LuFe_2O_4$, Nature, 436 (2005) 1136-1138.

[29] D.I. Khomskii, Classifying multiferroics: Mechanisms and effects, in: Physics, American Physical Society, 2009.

[30] N. Hur, S. Park, P.A. Sharma, J.S. Ahn, S. Guha, S.W. Cheong, Electric polarization reversal and memory in a multiferroic material induced by magnetic fields, Nature, 429 (2004) 392-395.

[31] T. Kimura, T. Goto, H. Shintani, K. Ishizaka, T. Arima, Y. Tokura, Magnetic control of ferroelectric polarization, Nature, 426 (2003) 55-58.

[32] G. Catalan, J.F. Scott, Physics and Applications of Bismuth Ferrite, Adv. Mater., 21 (2009) 2463-2485.

[33] F. Kubel, H. Schmid, Structure of a ferroelectric and ferroelastic monodomain crystal of the perovskite $BiFeO_3$, Acta Crystallographica Section B-Structural Science, 46 (1990) 698-702.

[34] F. Zavaliche, S.Y. Yang, T. Zhao, Y.H. Chu, M.P. Cruz, C.B. Eom, R. Ramesh, Multiferroic BiFeO3 films: domain structure and polarization dynamics, Phase Transitions, 79 (2006) 991-1017.

[35] G.A. Smolenskii, I.E. Chupis, SEGNETOMAGNETICS, Uspekhi Fizicheskikh Nauk, 137 (1982) 415-448.

[36] J.R. Teague, R. Gerson, W.J. James, Dielectric hysteresis in single crystal $BiFeO_3$ Solid State Commun., 8 (1970) 1073-&.

[37] H. Naganuma, Multifunctional Characteristics of B-site Substituted $BiFeO_3$ Films, in: M. Lallart (Ed.) Ferroelectrics - Physical Effects, InTech 2011.

[38] P. Fischer, M. Polomska, I. Sosnowska, M. Szymanski, Temperature-dependence of the crystal and magnetic-structures of $BiFeO_3$, Journal of Physics C-Solid State Physics, 13 (1980) 1931-1940.

[39] C. Ederer, N.A. Spaldin, Weak ferromagnetism and magnetoelectric coupling in bismuth ferrite, Physical Review B, 71 (2005).

[40] I. Sosnowska, T. Peterlinneumaier, E. Steichele, Spiral magnetic-ordering in bismuth ferrite, Journal of Physics C-Solid State Physics, 15 (1982) 4835-4846.

[41] L. Martin, S.P. Crane, Y.H. Chu, M.B. Holcomb, M. Gajek, M. Huijben, C.H. Yang, N. Balke, R. Ramesh, Multiferroics and magnetoelectrics: thin films and nanostructures, Journal of Physics-Condensed Matter, 20 (2008).

[42] J. Wang, J.B. Neaton, H. Zheng, V. Nagarajan, S.B. Ogale, B. Liu, D. Viehland, V. Vaithyanathan, D.G. Schlom, U.V. Waghmare, N.A. Spaldin, K.M.

Rabe, M. Wuttig, R. Ramesh, Epitaxial $BiFeO_3$ multiferroic thin film heterostructures, Science, 299 (2003) 1719-1722.

[43] H. Bea, M. Bibes, A. Barthelemy, K. Bouzehouane, E. Jacquet, A. Khodan, J.P. Contour, S. Fusil, F. Wyczisk, A. Forget, D. Lebeugle, D. Colson, M. Viret, Influence of parasitic phases on the properties of $BiFeO_3$ epitaxial thin films, Appl. Phys. Lett., 87 (2005).

[44] W. Eerenstein, F.D. Morrison, J. Dho, M.G. Blamire, J.F. Scott, N.D. Mathur, Comment on "Epitaxial $BiFeO_3$ multiferroic thin film heterostructures", Science, 307 (2005) 1203-1203.

[45] M.I. Morozov, N.A. Lomanova, V.V. Gusarov, Specific features of $BiFeO_3$ formation in a mixture of bismuth(III) and iron(III) oxides, Russ. J. Gen. Chem., 73 (2003) 1676-1680.

[46] S.M. Selbach, M.A. Einarsrud, T. Grande, On the Thermodynamic Stability of $BiFeO_3$, Chem. Mater., 21 (2009) 169-173.

[47] M. Valant, A.K. Axelsson, N. Alford, Peculiarities of a solid-state synthesis of multiferroic polycrystalline $BiFeO_3$, Chem. Mater., 19 (2007) 5431-5436.

[48] H. Ishiwara, Impurity substitution effects in $BiFeO_3$ thin films-From a viewpoint of FeRAM applications, Curr. Appl Phys., 12 (2012) 603-611.

[49] A. Lahmar, K. Zhao, S. Habouti, M. Dietze, C.H. Solterbeck, M. Es-Souni, Off-stoichiometry effects on $BiFeO_3$ thin films, Solid State Ionics, 202 (2011) 1-5.

[50] N.A. Spaldin, S.-W. Cheong, R. Ramesh, Multiferroics: Past, present, and future, Phys. Today, 63 (2010) 38-43.

[51] J. Zhang, Z. Duan, H. Zhang, M. Han, Y. Li, Z. Hu, J. Chu, Improved electric behaviors of the $Pt/Bi_{1-x}La_xFe_{0.92}Mn_{0.08}O_3/n(+)$-Si heterostructure for nonvolatile ferroelectric random-access memory, Journal of Materials Chemistry C, 1 (2013) 6252-6258.

[52] K. Kalantari, I. Sterianou, S. Karimi, M.C. Ferrarelli, S. Miao, D.C. Sinclair, I.M. Reaney, Ti-Doping to Reduce Conductivity in $Bi_{0.85}Nd_{0.15}FeO_3$ Ceramics, Adv. Funct. Mater., 21 (2011) 3737-3743.

[53] Achenbac.Gd, W.J. James, R. Gerson, Preparation of single-phase polycrystalline $BiFeO_3$, J. Am. Ceram. Soc., 50 (1967) 437-&.

[54] V.S. Filip'ev, N.P. Smolyaninov, E.G. Fesenko, I.N. Belyaev, Synthesis of $BiFeO_3$ and determination of the unit cell, Kristallografiya, 5 (1960) 958.

[55] A. Maitre, M. Francois, J.C. Gachon, Experimental study of the Bi_2O_3-Fe_2O_3 pseudo-binary system, J. Phase Equilib. Diffus., 25 (2004) 59-67.

[56] R. Palai, R.S. Katiyar, H. Schmid, P. Tissot, S.J. Clark, J. Robertson, S.A.T. Redfern, G. Catalan, J.F. Scott, beta phase and gamma-beta metal-insulator transition in multiferroic $BiFeO_3$, Physical Review B, 77 (2008).

[57] S.M. Selbach, T. Tybell, M.A. Einarsrud, T. Grande, Phase transitions, electrical conductivity and chemical stability of $BiFeO_3$ at high temperatures, J. Solid State Chem., 183 (2010) 1205-1208.

[58] D.C. Arnold, K.S. Knight, F.D. Morrison, P. Lightfoot, Ferroelectric-Paraelectric Transition in $BiFeO_3$: Crystal Structure of the Orthorhombic beta Phase, Phys. Rev. Lett., 102 (2009).

[59] A. Palewicz, R. Przenioslo, I. Sosnowska, A.W. Hewat, Atomic displacements in $BiFeO_3$ as a function of temperature: neutron diffraction study, Acta Crystallographica Section B-Structural Science, 63 (2007) 537-544.

[60] J.D. Bucci, Robertso.Bk, W.J. James, Precision determination of lattice parameters and coefficients of thermal expansion of $BiFeO_3$, J. Appl. Crystallogr., 5 (1972) 187-&.

[61] T. Rojac, A. Bencan, B. Malic, G. Tutuncu, J.L. Jones, J.E. Daniels, D. Damjanovic, $BiFeO_3$ Ceramics: Processing, Electrical, and Electromechanical Properties, J. Am. Ceram. Soc., 97 (2014) 1993-2011.

[62] J.F. Scott, Room-temperature multiferroic magnetoelectrics, Npg Asia Materials, 5 (2013).

[63] I. Fina, N. Dix, J.M. Rebled, P. Gemeiner, X. Marti, F. Peiro, B. Dkhil, F. Sanchez, L. Fabrega, J. Fontcuberta, The direct magnetoelectric effect in ferroelectric-ferromagnetic epitaxial heterostructures, Nanoscale, 5 (2013) 8037-8044.

[64] D. Ghosh, H. Han, J.C. Nino, G. Subhash, J.L. Jones, Synthesis of $BaTiO_3$-20wt%$CoFe_2O_4$ Nanocomposites via Spark Plasma Sintering, J. Am. Ceram. Soc., 95 (2012) 2504-2509.

[65] B. Liu, T. Sun, J.Q. He, V.P. Dravid, Sol-Gel-Derived Epitaxial Nanocomposite Thin Films with Large Sharp Magnetoelectric Effect, ACS Nano, 4 (2010) 6836-6842.

[66] H.M. Luo, H. Yang, S.A. Bally, O. Ugurlu, M. Jain, M.E. Hawley, T.M. McCleskey, A.K. Burrell, E. Bauer, L. Civale, T.G. Holesinger, Q.X. Jia, Self-

assembled epitaxial nanocomposite $BaTiO_3$-$NiFe_2O_4$ films prepared by polymer-assisted deposition, J. Am. Chem. Soc., 129 (2007) 14132-+.

[67] S.Q. Ren, L.Q. Weng, S.H. Song, F. Li, J.G. Wan, M. Zeng, $BaTiO_3$/$CoFe_2O_4$ particulate composites with large high frequency magnetoelectric response, J. Mater. Sci., 40 (2005) 4375-4378.

[68] H. Zheng, J. Wang, S.E. Lofland, Z. Ma, L. Mohaddes-Ardabili, T. Zhao, L. Salamanca-Riba, S.R. Shinde, S.B. Ogale, F. Bai, D. Viehland, Y. Jia, D.G. Schlom, M. Wuttig, A. Roytburd, R. Ramesh, Multiferroic $BaTiO_3$-$CoFe_2O_4$ nanostructures, Science, 303 (2004) 661-663.

[69] J.H. Li, I. Levin, J. Slutsker, V. Provenzano, P.K. Schenck, R. Ramesh, J. Ouyang, A.L. Roytburd, Self-assembled multiferroic nanostructures in the $CoFe_2O_4$-$PbTiO_3$ system, Appl. Phys. Lett., 87 (2005).

[70] X.S. Gao, B.J. Rodriguez, L.F. Liu, B. Birajdar, D. Pantel, M. Ziese, M. Alexe, D. Hesse, Microstructure and Properties of Well-Ordered Multiferroic $Pb(Zr,Ti)O_3$/$CoFe_2O_4$ Nanocomposites, ACS Nano, 4 (2010) 1099-1107.

[71] H. Ryu, P. Murugavel, J.H. Lee, S.C. Chae, T.W. Noh, Y.S. Oh, H.J. Kim, K.H. Kim, J.H. Jang, M. Kim, C. Bae, J.G. Park, Magnetoelectric effects of nanoparticulate $Pb(Zr_{0.52}Ti_{0.48})O_3$-$NiFe_2O_4$ composite films, Appl. Phys. Lett., 89 (2006).

[72] J.G. Wan, X.W. Wang, Y.J. Wu, M. Zeng, Y. Wang, H. Jiang, W.Q. Zhou, G.H. Wang, J.M. Liu, Magnetoelectric $CoFe_2O_4$-$Pb(Zr,Ti)O_3$ composite thin films derived by a sol-gel process, Appl. Phys. Lett., 86 (2005).

[73] R.A. Islam, V. Bedekar, N. Poudyal, J.P. Liu, S. Priya, Magnetoelectric properties of core-shell particulate nanocomposites, J. Appl. Phys., 104 (2008).

[74] N. Dix, R. Muralidharan, J.M. Rebled, S. Estrade, F. Peiro, M. Varela, J. Fontcuberta, F. Sanchez, Selectable Spontaneous Polarization Direction and Magnetic Anisotropy in $BiFeO_3$-$CoFe_2O_4$ Epitaxial Nanostructures, ACS Nano, 4 (2010) 4955-4961.

[75] F. Zavaliche, H. Zheng, L. Mohaddes-Ardabili, S.Y. Yang, Q. Zhan, P. Shafer, E. Reilly, R. Chopdekar, Y. Jia, P. Wright, D.G. Schlom, Y. Suzuki, R. Ramesh, Electric field-induced magnetization switching in epitaxial columnar nanostructures, Nano Lett., 5 (2005) 1793-1796.

[76] S.M. Stratulat, X.L. Lu, A. Morelli, D. Hesse, W. Erfurth, M. Alexe, Nucleation-Induced Self-Assembly of Multiferroic $BiFeO_3$-$CoFe_2O_4$ Nanocomposites, Nano Lett., 13 (2013) 3884-3889.

[77] H. Zheng, Q. Zhan, F. Zavaliche, M. Sherburne, F. Straub, M.P. Cruz, L.Q. Chen, U. Dahmen, R. Ramesh, Controlling self-assembled perovskite-spinel nanostructures, Nano Lett., 6 (2006) 1401-1407.

[78] H.M. Zheng, F. Straub, Q. Zhan, P.L. Yang, W.K. Hsieh, F. Zavaliche, Y.H. Chu, U. Dahmen, R. Ramesh, Self-assembled growth of $BiFeO_3$-$CoFe_2O_4$ nanostructures, Adv. Mater., 18 (2006) 2747-+.

[79] C.W. Nan, Magnetoelectric effect in composites of piezoelectric and piezomagnetic phases, Physical Review B, 50 (1994) 6082-6088.

[80] J. Ma, J.M. Hu, Z. Li, C.W. Nan, Recent Progress in Multiferroic Magnetoelectric Composites: from Bulk to Thin Films, Adv. Mater., 23 (2011) 1062-1087.

[81] R.E. Newnham, D.P. Skinner, L.E. Cross, Connectivity and piezoelectric-pyroelectric composites, Mater. Res. Bull., 13 (1978) 525-536.

[82] L. Mitoseriu, V. Buscaglia, Intrinsic/extrinsic interplay contributions to the functional properties of ferroelectric-magnetic composites, Phase Transitions, 79 (2006) 1095-1121.

[83] G. Schileo, Recent developments in ceramic multiferroic composites based on core/shell and other heterostructures obtained by sol-gel routes, Prog. Solid State Chem., 41 (2013) 87-98.

[84] M.I. Bichurin, V.M. Petrov, G. Srinivasan, Theory of low-frequency magnetoelectric coupling in magnetostrictive-piezoelectric bilayers, Physical Review B, 68 (2003).

[85] C.W. Nan, G. Liu, Y.H. Lin, H.D. Chen, Magnetic-field-induced electric polarization in multiferroic nanostructures, Phys. Rev. Lett., 94 (2005).

[86] N. Dix, R. Muralidharan, B. Warot-Fonrose, M. Varela, F. Sanchez, J. Fontcuberta, Critical Limitations in the Fabrication of Biferroic $BiFeO_3$-$CoFe_2O_4$ Columnar Nanocomposites Due to Bismuth Loss, Chem. Mater., 21 (2009) 1375-1380.

[87] H. Zheng, J. Wang, L. Mohaddes-Ardabili, M. Wuttig, L. Salamanca-Riba, D.G. Schlom, R. Ramesh, Three-dimensional heteroepitaxy in self-assembled $BaTiO_3$-$CoFe_2O_4$ nanostructures, Appl. Phys. Lett., 85 (2004) 2035-2037.

[88] J. Slutsker, I. Levin, J.H. Li, A. Artemev, A.L. Roytburd, Effect of elastic interactions on the self-assembly of multiferroic nanostructures in epitaxial films, Physical Review B, 73 (2006).

[89] J.X. Zhang, Y.L. Li, D.G. Schlom, L.Q. Chen, F. Zavaliche, R. Ramesh, Q.X. Jia, Phase-field model for epitaxial ferroelectric and magnetic nanocomposite thin films, Appl. Phys. Lett., 90 (2007).

[90] L.W. Martin, Y.H. Chu, R. Ramesh, Advances in the growth and characterization of magnetic, ferroelectric, and multiferroic oxide thin films, Materials Science and Engineering: R: Reports, 68 (2010) 89-133.

[91] J.F. Scott, Data storage - Multiferroic memories, Nat. Mater., 6 (2007) 256-257.

Chapter 2

Deposition of thin films and nanostructures

2.1 Introduction

Thin films are specific due to their dimensions, where one dimension (thickness) is almost negligible in comparison to the other two dimensions. The properties of materials in thin film form are different compared with bulk or powders due to their 'two-dimensionality' and the influence of the substrate used for film deposition on the final film structure and morphology.

Film deposition parameters have a great impact on thin film morphology and structure. This relation, in turn, enables tailoring of material properties through control of these parameters during thin film processing [1]. Multiferroic thin films and nanostructures have been produced using a range of chemistry-based and physical deposition techniques including chemical solution deposition, chemical vapour deposition, pulsed laser deposition, sputtering, molecular beam epitaxy, and more [2]. In this chapter, details of some deposition routes are discussed in general as well as their advantages and drawbacks.

Besides growth techniques and their parameters, another important factor in the processing of thin films is the choice of an appropriate substrate. Depending on their purpose, application and goal they should achieve, metal oxide thin films have been fabricated on various substrates resulting in polycrystalline or epitaxial films [3-6].

2.2 Chemical solution deposition (CSD)

Chemical solution deposition is a technique that belongs to chemistry-based routes for deposition of thin films. In this route the solution is simply a vehicle to deposit the desired elements onto the substrate [7]. The process of thin film deposition comprises of several steps as Figure 2.1 illustrates: preparation of the precursor, film deposition on the substrate by spin coating, drying, pyrolysis and thermal treatment. The following sections discuss each of these steps in more detail.
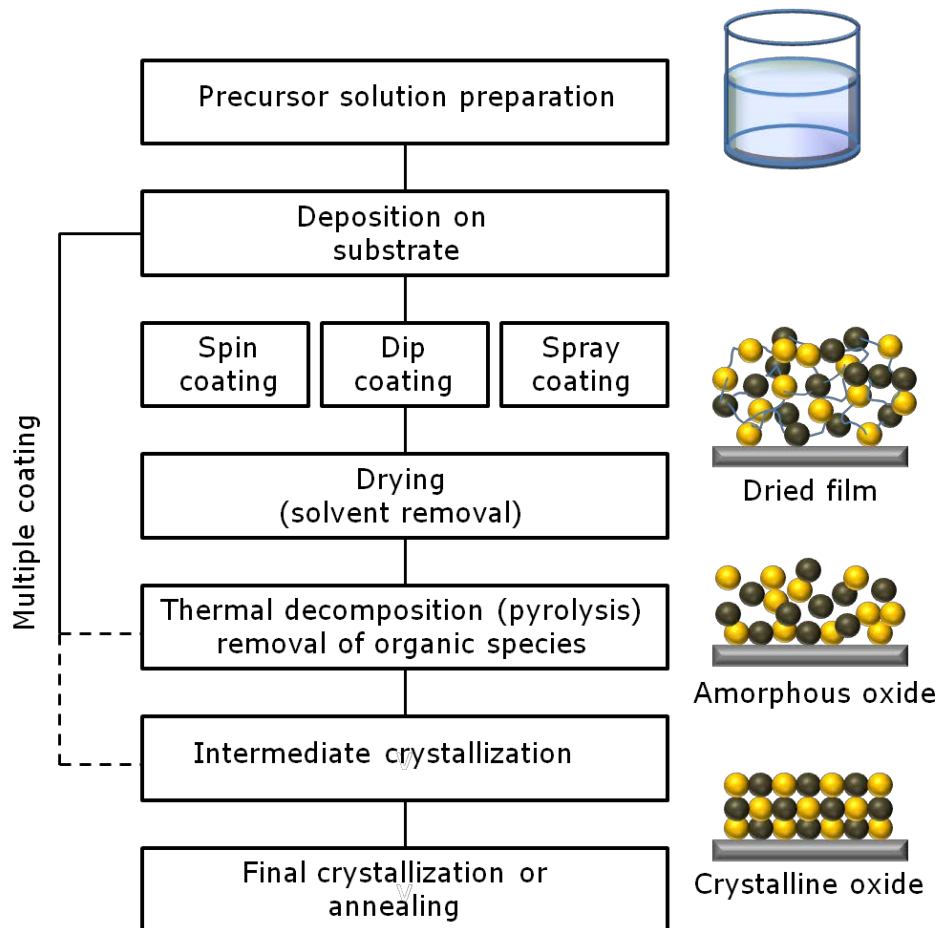
Figure 2.1: Schematic representation of the chemical solution deposition (CSD) process for the preparation of metal oxide thin films. Adapted from references [8] and [9].

2.2.1 Synthesis of the precursor solution(s)

Thin films of complex metal oxides like multiferroics can be produced from solutions that contain precursor molecules for the different elements in the desired multielement compound. The choice of solvent (aqueous or organic) and the chemical precursors used for the various cations as well as the way of precursor solution preparation determine the specific procedures for handling and storage of the solution. Furthermore, they also affect the final microstructure and the properties of the obtained films. Subsequent decomposition and thermal treatment and processing have to be adjusted in a way to ensure obtaining the microstructure that would lead to the optimal materials properties. This fine-tuning of processing conditions is closely connected with the specific chemistries and routes employed [3, 4].

Metallo-organic decomposition (MOD)

Metallo-organic decomposition routes work on the principle that one can simply dissolve every metallo-organic compound separately in an apolar solvent, usually xylene, and combine the solutions to yield the desired stoichiometry. As starting reagents, MOD employs low-reactivity metal carboxylate compounds with long aliphatic rest groups (e.g. 2-ethylhexanoate and neodecanoates) or β-diketonates (e.g. acetyl acetonates). Due to the fact that starting compounds are water-insensitive, they do not undergo any hydrolysis or condensation (polymerization) reactions which, together with the use of non-interactive solvents, results in solutions being a simple mixture of the starting compounds. Therefore in this synthesis route no gel formation occurs.

Although MOD synthesis is straightforward, certain limitations can appear during the processing of thin films. The presence of large organic ligands leads to excessive weight loss and possible shrinkage after deposition causing cracking during thermal treatment. In order to avoid these obstacles, in some cases more polar solvents and short-chain metallo-organic compounds (e.g. acetates or propionates) are used [3, 8, 9].

Sol-gel

In alkoxide sol-gel synthesis, molecular alkoxides polymerize forming a three-dimensional oxide network or gel. After removing the solvent from this wet gel

xerogel forms. For the synthesis of alkoxide-based gels, metal alkoxides M(OR)z or mixtures of metal salts and metal alkoxides are used as starting compounds. Difference in electronegativities of the metal and the oxygen atoms causes the polarity of the metal-oxygen bond in metal alkoxides, as shown in Figure 2.2 [10].
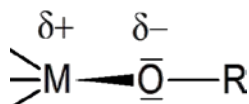
Figure 2.2: Schematic of the polar metal-oxygen bond in metal alkoxides. The different electronegativities of the metal and the oxygen atoms lead to positive and negative partial charges on these atoms as indicated by δ+ and δ-, respectively [10].

As a result of this polarity, metal alkoxides are very sensitive to the nucleophilic attack of water molecules. In presence of water, starting reagents hydrolyze readily resulting in partially hydrolyzed monomers as shown in (1).

$$\text{(1)}$$
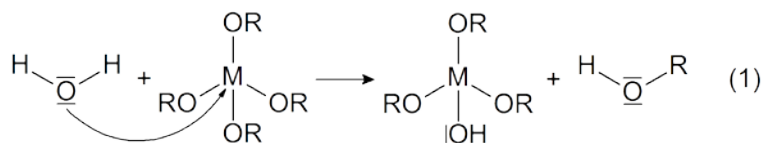
These partially hydrolyzed monomers undergo further condensation via alkolation (2), alkoxolation (3), olation (4) or oxolation (5) reactions resulting in oligomers, (Figure 2.3) [9, 11]. Growth of these oligomers continues further into larger clusters through further condensation reactions, and a three dimensional network or gel is formed after aggregation of elementary clusters. The structure of the formed gels depends on the hydrolysis and condensation rates of the constituent metal alkoxides. Contributions of each of these reactions depend on the exact nature of the metal ion (electrophilicity) and its ability to undergo coordination expansion, concentration of water for hydrolysis, using acid or base catalysis etc. The limitations of alkoxide sol-gel processes lie in the high sensitivity of alkoxide compounds in ambient conditions and often it requires work to be carried out in a protective atmosphere [10].
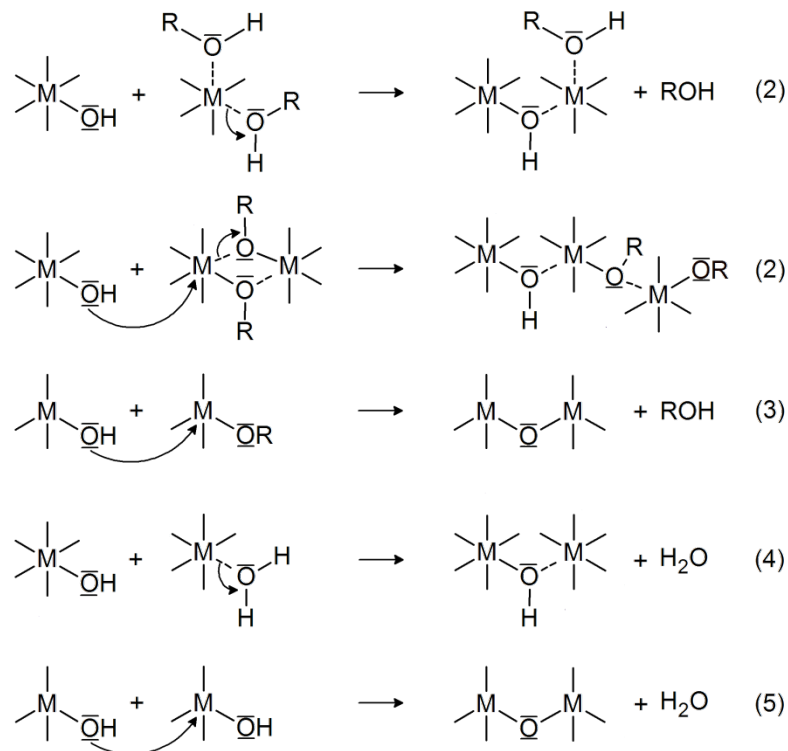
Figure 2.3: Partially hydrolyzed monomers undergo further condensation via alkolation(2), alkoxolation (3), olation (4) or oxolation (5) reactions resulting in oligomers

For chemical synthesis of perovskite material, sol-gel processes that use 2-methoxyethanol as a reactant and solvent are widely used. The widespread use of this solvent lies in its ability to solubilize a variety of different precursors offering a good stability, control and repro-ducibility of process chemistry and minimal aging effect. On the other hand, methoxyethanol is known teratogen and the toxicity of the solvent is a major health concern [8].

Aqueous solution-gel route

The basic principle of the aqueous solution-gel route is the reaction of the metal ions with chelating α-hydroxy-carboxylato ligands to form α-hydroxy-carboxylato metal complexes in water as the solvent. During evaporation of the solvent, concentration of the solution occurs and viscosity rises above a critical metal concentration. This solvent evaporation forces interactions between the

precursor species where crosslinking reactions lead to a high enough viscosity inhibiting precipitation of the α-hydroxy-carboxylato metal complexes. As a result of these interactions, a transparent, amorphous gel is obtained [9]. The gel structure ideally consists of metal carboxylate complexes linked to one another via metal-carboxylate, ammonium (NH_4^+-O) bridges [12].

In this way it is possible to obtain stable aqueous solutions of different metal ions suitable for gel formation and thus for further thin film deposition. Even very complex metal ions which are extremely sensitive towards hydrolysis and consequent condensation such as Ti(IV), Zr(IV), Nb(V) and Ta(V) were obtained as a stable ion species in water [13-16].

The use of citrato ligands is very common in aqueous solution-gel routes. This type of ligand lowers the partial charge on the central metal, thereby stabilizing the citrate-metal complex towards hydrolysis. Another important advantage of using the citrato ligand is its capability to crosslink several citrato-metal complexes with ionic bridges, further supporting the formation of a three dimensional network and preventing precipitation during gelation. Thus citrate-metal precipitation is inhibited by the intrinsic structure of the citrato-metal complex itself.

Compared with the alkoxide route, this approach offers some advantages such as: no need to work in a protective atmosphere, cost effective and more environmentally friendly due to the use of water as a solvent as well as the other issues with using toxic solvents such as methoxyethanol.

Polymer *complex controlled routes*
Polymer complex controlled routes involve *in situ* polymeric complexation methods (IPC) known as the "Pechini process" and "polymer complex solution method (PCS)".

In the Pechini process, starting compounds such as carboxylic acids (mostly citric acid) and metal carboxylate complexes (mostly citrate complexes) are dissolved in ethylene glycol. Molecular carboxylic acid as well as metal carboxylate reacts with ethylene glycol to form organic ester compounds. Ester polymerization increases the degree of cross linking between carboxylato-metal complexes. This *in situ* polymerization leads to a gel structure in which the

backbone consists of an organic polymer to which cations are attached [8, 9, 17].

In another approach with similar results, referred to as the polymer complex solution method, metalcoordinating polymers and metal salts are directly dissolved in an appropriate solvent (usually water). In this case, cations are attached to the organic polymer, although in situ polymerisation does not take place. Depending on the type of polymer, the metal ions can crosslink within the gel structure. Polyvinylalcohol, polyacrylic acid, polyethyleneimine as well as other polymers with appropriate functional groups are used [9, 17, 18].

Viscosity control through polymer addition
This approach is based on the addition of non-complexing polymers into a solution containing metal cations. Due to solvent evaporation viscosity increases which guarantees the spatial fixation and homogeneous distribution of the metal ions in the gel structure [9].

Colloidal, physical or particulate sol-gel routes
In this method colloidal particles with a diameter of 1-100 nm are dispersed in a liquid medium to form a sol. Formation of the gel is regulated by electrostatic and/or steric interactions between the colloidal particles in the sol. The particulate gels consist of aggregates of colloidal particles dispersed on the nanometer scale [9].

2.2.2 Spin coating

Spin coating is a widespread technique for the deposition of thin and uniform coatings on top of a flat substrate. Due to rapidly spinning the substrate, radial rotation forces are induced in the deposited liquid layer leading to its thinning. On the other hand, evaporation of the solvent induces an increase in film viscosity resulting in a gradual decrease of and finally suppressing the influence of radial forces on the layer thinning. Thus, the balance between centripetal and viscous forces induced in the layer during spinning affects the final layer thickness [19]. The deposition process comprises of four steps as illustrated in Figure 2.4 [8, 19, 20]. In the first step, an excess of precursor solution is

applied onto a cleaned substrate usually using a syringe with 0.2 μm filter. The second step is the acceleration of the substrate to the desired spinning rate. During this step, over 95% of the liquid is spun off from the substrate surface. The third step is a set time period (often 30-60 s) during which the substrate rotation rate is held constant. It is possible to distinguish two stages affecting the thinning of the layer. In the first stage, the film thins due to centripetal forces and fluid flow. Here, the thinning rate depends on the viscosity of the fluid and the rotation speed. In the second stage, the film thinning is primarily due to the solvent evaporation. After the set time has expired, the spin coating process has finished resulting in a uniform film with a reproducible thickness.
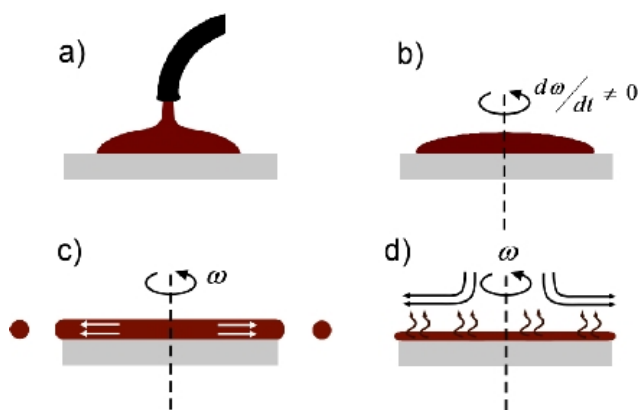
Figure 2.4: The different stages of spin coating process: a) dispensation, b) acceleration, c) flow dynamics domination, d) evaporation domination [20].

2.2.3 Thermal treatment and film crystallization

Immediately following the deposition, an as-deposited film is amorphous and contains significant amounts of organic species. The nature of the as-deposited films depends on the type of precursor interactions and the film gelation behavior. The gelation process in thin films is generally caused by evaporation of the solvent during or shortly after deposition [3]. Thus, thermal treatment is the next step in the film processing in which amorphous films are converted into the desired crystalline phase. Although crystallization of the films is possible by heating the film directly to its crystallization temperature, an approach in which

a pyrolysis step and subsequent crystallization anneal are separated is more common. It has been proposed that the two-step procedure allows for the removal of organic constituents prior to the collapse of the amorphous network which minimizes cracking and blistering. In this two-step processing, a film is first placed on the hot plates with a temperature range between 100°C to 400°C in order to remove solvents trapped inside the porous structure and the organic species originating from the gel network. During the rearrangement of the gel network M–O-C and M–O-H bonds are broken, and as the associated volatile species are removed followed by the formation of an M–O-M network [8].

With subsequent treatment at higher temperatures, pyrolyzed amorphous films are subjected to crystallization occurring through a nucleation-and-growth process. In general, the resulting microstructure of CSD derived films is a product of the different characteristics of between homogeneous and heterogeneous nucleation events. Thus, homogeneous nucleation within the amorphous matrix or heterogeneous nucleation at interfaces or at nucleation seeds inside the bulk have specific nucleation and growth rates. From nucleation and growth theory, the energy barriers for homogeneous and heterogeneous nucleation and their dependence on thermodynamic driving force ΔG_V (the energy difference between the amorphous and crystalline state) are described by

$$\Delta G^*_{homo} = \frac{16\pi\gamma^3}{3(\Delta G_V)^2} \tag{2.1}$$

$$\Delta G^*_{hetero} = \frac{16\pi\gamma^3}{3(\Delta G_V)^2} f(\theta) \tag{2.2}$$

where γ is the interfacial energy, and $f(\theta)$ is a function related to the contact angle of the nucleus with respect to the substrate, θ. For a hemispherical nucleus, $f(\theta)$ can be expressed as

$$f(\theta) = \frac{(2 - 3\cos\theta + \cos^3\theta)}{4} \tag{2.3}$$

If nucleation takes place at the substrate-film interface, the resulting film microstructure consists of oriented columnar grains while polycrystalline films with equiaxed grains are usually the result of nucleation occurring throughout the film. The heterogeneous nucleation barrier at the interface is generally lower than the homogenous barrier for crystallization in the bulk. However, the possible crystallization event is dependent on the driving force ΔG_V. The diagram in Figure 2.5 shows the difference in free energy between the crystalline phase and an amorphous solution-derived thin film. Considering the diagram in Figure 2.5, crystallization at low temperature results in a high crystallization driving force and therefore, there should be enough energy to surmount all energetic nucleation barriers. In this case, bulk nucleation becomes as probable as interface nucleation. On the other hand, if crystallization is postponed to higher temperature, the process proceeds with a lower driving force. Due to the contact angle term $f(\theta)$, $[f(\theta)<1]$, the energy advantage of heterogeneous nucleation at the substrate interface becomes significant [3].
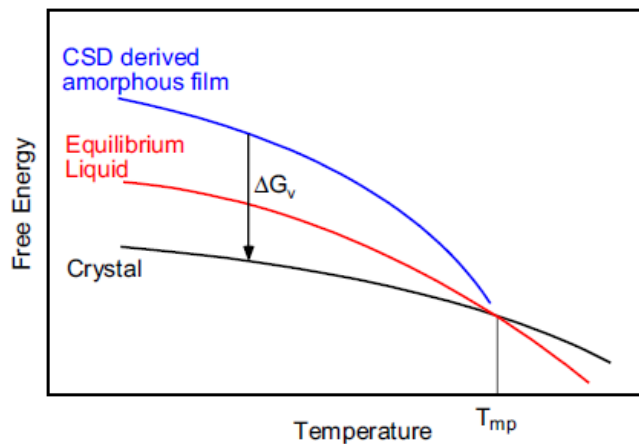
Figure 2.5: Schematic diagram of the free energies of a solution derived amorphous film, the ideal supercooled liquid, and the crystalline perovskite phase [8].

Control of heterogeneous nucleation at the interface plays an important role in the preparation of epitaxial and highly oriented (textured) films. Here, lattice matching with the substrate and thermal processing parameters are recognized as the key factors. If the substrate has structural and dimensional similarities with the film, the value of $f(\theta)$ is expected to decrease. According to equations

2.1 and 2.2, this decrease would lower the energy for heterogeneous nucleation at interface compared to nucleation within the bulk of the film. Furthermore, high heating rates during film processing postpone crystallization to higher temperatures. This causes nucleation to occur at a higher temperature. From the diagram in Figure 2.5, it can been seen that crystallization at higher temperatures involves lower driving force, and due to the $f(\theta)$ term, lower energy heterogeneous nucleation become more dominant in defining the film microstructure.

Preparation of epitaxial films via solution deposition when there is a high lattice matching and structural similarity between the film and substrate involves growth of nanometer sized epitaxial grains at the film/substrate interface. These grains grow along the interface and further towards the surface by consuming randomly oriented grains [7, 21].

2.3 Pulsed Laser Deposition (PLD)

Pulsed laser deposition (PLD) is one of the most widespread physical vapour deposition techniques for the growth of multicomponent oxide thin films. In PLD, high energy laser pulses hit a target, removing material from its surface. As a result of this ablation process, a transient, highly luminous plasma plume forms containing neutral species, ions, electrons, etc. [2]. The plasma plume expands from the target towards the substrate where the vaporized materials condense and film growth occurs. Using short pulse duration keeps generalized heating of the target low and minimizes thermal evaporation for the most volatile elements [22]. The PLD process for the growth of thin films is shown schematically in Figure 2.6. The system is made up of a vacuum chamber equipped with pumps, a target holder, rotator and substrate heater. The film can be deposited in a reactive environment, like in the case of oxides where oxygen, ozone or atomic oxygen with careful control of the gas partial pressure ensures the growth of fully oxidized films [2]. In general, growth of relatively high quality thin films can be achieved by a combination of reactive gas pressure and substrate temperature giving access to a wide range of thermodynamic conditions as well as maintaining complex stoichiometries from oxide targets in thin films [22]. However, some of the drawbacks of PLD as a deposition technique are the small

area of homogeneously deposited material ($\sim 1cm^2$), the presence of particulates of molten material in plume that can deteriorate films properties and the lack of fundamental understanding of the process since for novel materials, deposition parameters still to be obtained by empirical optimization [23].
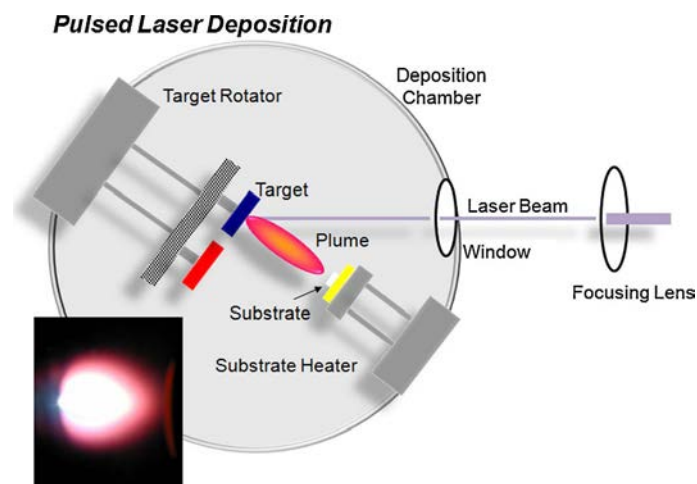
Figure 2.6: Scheme of a pulsed laser deposition system. The inset shows an actual photograph of the plume [2].

2.4 Sputter deposition

Sputtering is the ejection of species from a solid surface (target) which is subjected to bombardment by energetic gas ions. In this way, a vapour flux is created that subsequently deposits the film on a heated substrate [1]. In contrast to PLD, sputtering growth is widely used for large-scale production. A typical deposition rate of 1-10 nm/min is achieved for plasma sputter deposition. Major limitations involve the control of the film stoichiometry (due to different yield efficiencies and dissociation of components) of the components and the thickness uniformity over large areas. In order to assure the oxygen stoichiometry being close to the desired level, reactive gases such as pure O_2 or an Ar/O_2 mixture are used during the growth of oxide thin films [24]. Several

sputter deposition techniques have been used in the growth of oxide thin film including on-axis dc magnetron sputtering, cylindrical magnetron sputtering, ion-beam sputtering and off-axis sputtering [24, 25].

2.5 Epitaxial growth of thin films and nanostructures

The term epitaxy is composed of the Greek words *epi* meaning akin or upon, and *taxis* meaning arrangement or order. Thus, epitaxy refers to the growth of a single crystal film on top of a crystalline substrate with the same (or related) crystal arrangement. The structural and dimensional similarity between the film and substrate often leads to the formation of coherent or semicoherent interfaces. These interfaces have a significantly lower energy compared with noncoherent ones. Thus, the formed interface can have an effect on the choice of the nucleus crystallographic structure because the system tends to minimize its free energy to reach equilibrium [26].

It is possible to distinguish two major types of epitaxial growth, homoepitaxy and heteroepitaxy. In the case of homoepitaxial growth, the deposited film and substrate are the same material (for instance, growth of doped-Si on Si substrate) or film and substrate are different materials but have very similar lattice parameters. As Figure 2.7a illustrates, homoepitaxial growth leads to little disorderliness in the structure across the interface. Another type of epitaxial growth, heteroepitaxy refers to the case where the film and the substrate are different materials, but the substrate structure is similar to the structure of desired film what helps guide the growth of the films [2]. The other two figures, Figure 2.7b and 2.7c illustrate two possibilities of heteroepitaxial growth, so called strained-layer epitaxy and relaxed epitaxy, respectively. The latter occurs most frequently for very thin films on the substrate of the same crystal structure (e.g. perovskite on perovskite). In case of relaxed epitaxy, the lattice mismatch is somewhat larger, thus crystal structure of the resulting film and the underlying substrate might be different. This difference results in relaxation of film to its bulk structure through the formation of defects. The most common types of defects are dislocations that accommodate interfacial strain [27].
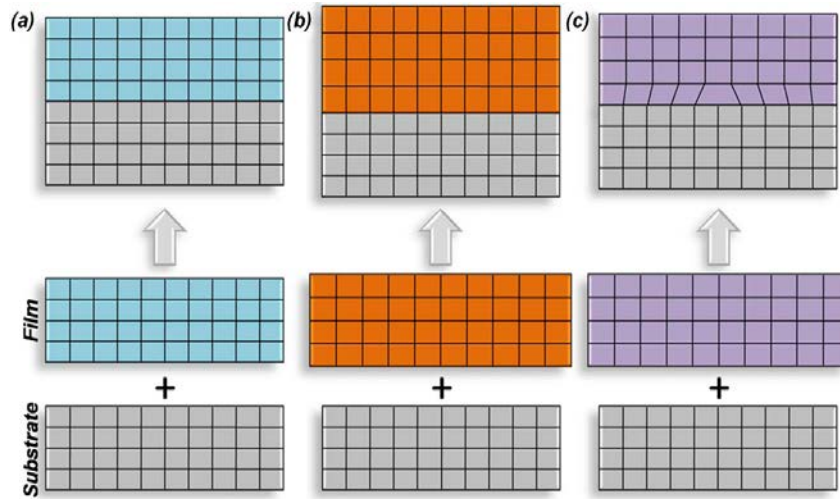
Figure 2.7: Schematic illustration of a) nearly perfect lattice match, b) strained and c) relaxed heteroepitaxial film growth [2].

Predictions for the growth of epitaxial films can be based on the lattice mismatch between the film and the substrate material *f*, which is defined as:

$$f = \frac{2(a_f - a_s)}{a_f + a_s} \sim \frac{a_f - a_s}{a_s} \sim \frac{a_s - a_f}{a_f} \tag{2.4}$$

where a_f and a_s are the lattice parameters of film and substrate, respectively. For $f < 0.1$ it is possible to expect epitaxial growth. On the other hand, for $f > 0.1$ only a few interfacial bonds between film and substrate are properly aligned so that the reduction in interfacial energy is not enough to result in epitaxial growth of the film. The *f* can also a be function of temperature when thermal expansion coefficients of film and substrate are very different (i.e. the growth of some oxides on silicon) [28].

Whether epitaxial growth of oxide films occurs or not essentially depends on several conditions. Influence of the substrate (lattice mismatch, surface orientation, lattice structure and thermal expansion), use of metallic electrodes or buffer layers, processing parameters (pressure and temperature), cation substitution, site engineering, film thickness, precursor chemistry etc. should be

taken into account in order to achieve layers with good crystallographic properties [24].

Epitaxial stabilization and role of the substrate

The formation of low energy interfaces due to structural similarity and lattice matching between film and substrate as well as substrate-induced epitaxial strain arising from the (low) lattice mismatch are exploited in 'epitaxial stabilization'. This phenomenon gives access to compounds or phases that are metastable or achievable only at high pressure or temperature or difficult to synthesize in powders or bulk but can form thin films [26]. Furthermore, epitaxially stabilized structures in thin films very often exhibit enhanced physical properties in comparison with the bulk forms [29-32]. Thus, the epitaxial strain in the films can have a significant effect on ferroelectric polarization in the perovskite oxide ferroelectrics [32-34]. The enhancement of polarization is related to some structural distortions linked to in-plane biaxial strain such as octahedral rotations [34, 35].

Research on epitaxial stabilization of oxides in thin films has included different metastable compounds with some examples such as $RNiO_3$, $BaCu_3O_4$, $NdMn_7O_{12}$ as well as some polymorph forms of $BaRuO_3$, $RMnO_3$, TiO_2 and Mn_3O_4 where the choice of the substrate played an important role [26]. The film-substrate lattice mismatch and film thickness are critical parameters for epitaxial stabilization of unstable compounds and polymorphs [26, 36].

In the field of multiferroics, the perfect example of the influence of epitaxial strain on the thin film structure is the formation of the metastable, orthorhombic perovskite phase of $YMnO_3$ (YMO) instead of the hexagonal phase on the appropriate substrates including $SrTiO_3$ (001) and $NdGaO_3$ (101) [37]. Another important example of compound stabilization that is not stable at atmospheric pressure is the growth of $BiMnO_3$ in thin films on single crystal $SrTiO_3$ (001) [38]. Multiferroic $TbMnO_3$ shows significantly enhanced ferroelectric properties compared to the orthorhombic bulk values when deposited in hexagonal phase or epitaxially stabilized on hexagonal substrate [31].

Through epitaxial strain imposed by the substrate, Zeches et al. stabilized a tetragonal polymorph of $BiFeO_3$ [35]. They corroborated their theoretical

predictions in Figure 2.8 with experimental work by depositing BFO films on a variety of substrates including (110) DyScO$_3$ (DSO) (a = 3.94Å), SrTiO$_3$ (STO) (a = 3.905 Å), (001) (LaAlO$_3$)$_{0.3}$(SrAl$_{0.5}$Ta$_{0.5}$O$_3$)$_{0.7}$ (LSAT) (a = 3.87 Å), LaAlO$_3$ (LAO) (a= 3.79Å), and YAlO$_3$ (YAO) (a= 3.69Å). Thus, BFO films on YAO consist of the tetragonal-like (T) phase, while films on LAO exhibit a mixed T and rhombohedral-like R phase, and films on LSAT, STO and DSO are rhombohedral-like in nature. Coexistence of the T and R phase in the sample is very interesting from an application point of view since formation of morphotropic phase boundary can lead to high piezoelectric responses [35, 39].
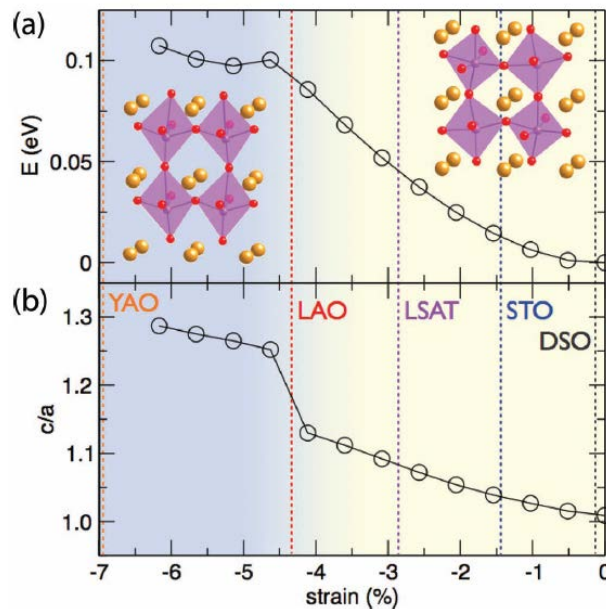
Figure 2.8: a) Evolution of total energy of the BFO structure as a function of in-plane strain. b) Evolution of the c/a lattice parameter ratio as a function of strain for BFO. The insets show two structural variants, both with monoclinic symmetry: on the left with the long c-axis is the tetragonal-like phase and on the right with the short c-axis is the rhombohedral-like phase. The lattice strains corresponding to a number of commonly used oxide substrates are shown as dashed lines [35].

2.6 Self-assembly and multiferroic nanocomposite thin film structures

Multiferroic composites with vertical nanostructures are usually self assembled/self-organized systems [40, 41]. These structures consist of two intermixed materials grown on the single crystal substrate, whereby the growth of the most thermodynamically stable phase or phases (taking into account epitaxial stabilization) occurs. According to MacManus-Driscoll, four basic conditions that determine the mechanism of forming self-assembled vertical nanostructure are: immiscibility of two phases, i.e. no solid solution may exist between AO_a and BO_a oxides, ii) miscibility of A, B and O, iii) miscibility at higher temperature with tendency toward clustering and iv) partial miscibility where the phase of lower symmetry precipitates in a matrix consisting of the phase with higher symmetry [42]. The three basic growth mechanisms are nucleation and growth, spinodal decomposition and pseudo-spinodal decomposition. When two phases form in the film by nucleation and growth, then size, orientation and phase distribution are dependent on the epitaxial constraints. The form of microstructure is influenced by a) the ratio of A:B, b) the crystallographic relations and the surface energies between the two phases, and between each phase and the substrate, and c) the growth kinetics. Thus in the case of films composed of two immiscible phases like $BiFeO_3$ and $CoFe_2O_4$ with the mixing ratio in the range 65:35-33:67 grown on single crystal (001) $SrTiO_3$ substrate it is found that (001) $BiFeO_3$ completely wets the STO substrate due to the low interfacial energy between these two crystallography matched perovskite surfaces. Contrary, the CFO phase only partially wets the substrate and grows as pillars embedded in the $BiFeO_3$ matrix and on top of the film forms islands bonded by four {111} surfaces, see also Figure 2.9a. When a (111) STO substrate is used, the situation is completely changed since now CFO completely wets the substrate producing planar films while BFO crystals grow in pyramidal form embedded in the CFO matrix [43]. Compared to $BiFeO_3$-$CoFe_2O_4$, similar microstructure on (001) STO substrate is observed for $BaTiO_3$-$CoFe_2O_4$ composites, with the difference in morphology of the CFO phase which form pillars of a cylindrical shape instead of pyramidal, see Figure 2.9b [44].
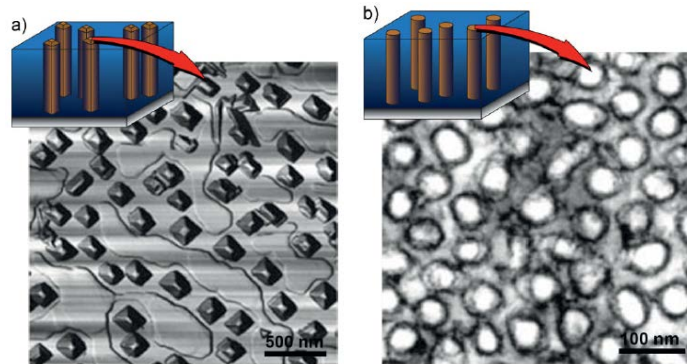
Figure 2.9: Top-view SEM images of $CoFe_2O_4$ crystallites embedded in the perovskite phase grown by PLD on (001) $SrTiO_3$ substrate. a) Pyramidal shaped $CoFe_2O_4$ islands in $BiFeO_3$ matrix; b) cylindrical $CoFe_2O_4$ nanopillars in $BaTiO_3$ matrix [42-44].

Differences in the morphology of the CFO phase can be explained by minimizing the overall energy. With the cylindrical shape the surface energy per unit volume decreases whereas highly faceted (e.g. cubic or pyramidal shape) pillars minimize the elastic strain energy. Concerning the relations between the two constituent phases and the shape of the CFO islands, there is a larger lattice misfit between $BiFeO_3$ ($a \approx 3.93$ Å) and $CoFe_2O_4$ ($a/2 \approx 4.13$Å) than in the case when CFO grows in BaTiO3 ($a \approx 4$ Å). Thus, a partial explanation for more faceted islands of CFO in BaTiO3 lies in more strain energy that has to be accommodated [42].

Spinodal decomposition upon cooling occurs in 50:50 $BiFeO_3:Sm_2O_3$ films with wide miscibility regions. The distinct phase separation results in ordered checkerboard structures of near $BiFeO_3$ and Sm_2O_3 compositions of less than 20nm in dimension, see Figure 2.10 [42, 45].
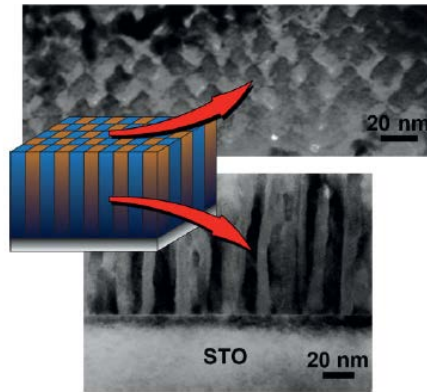
Figure 2.10: TEM image of $Bi_{0.5}Sm_{0.5}FeO_3$ film starting composition with regular checkerboard domains of near $BiFeO_3$ and Sm_2O_3 compositions (top) and TEM cross-section image of the same sample (bottom) [42, 45].

References

[1] Z.H. Barber, The control of thin film deposition and recent developments in oxide film growth, J. Mater. Chem., 16 (2006) 334-344.

[2] L.W. Martin, Y.H. Chu, R. Ramesh, Advances in the growth and characterization of magnetic, ferroelectric, and multiferroic oxide thin films, Materials Science and Engineering: R: Reports, 68 (2010) 89-133.

[3] R.W. Schwartz, Chemical solution deposition of perovskite thin films, Chem. Mater., 9 (1997) 2325-2340.

[4] N. Bassiri-Gharb, Y. Bastani, A. Bernal, Chemical solution growth of ferroelectric oxide thin films and nanostructures, Chem. Soc. Rev., 43 (2014) 2125-2140.

[5] G.L. Brennecka, J.F. Ihlefeld, J.P. Maria, B.A. Tuttle, P.G. Clem, Processing Technologies for High-Permittivity Thin Films in Capacitor Applications, J. Am. Ceram. Soc., 93 (2010) 3935-3954.

[6] L.W. Martin, D.G. Schlom, Advanced synthesis techniques and routes to new single-phase multiferroics, Current Opinion in Solid State & Materials Science, 16 (2012) 199-215.

[7] F.F. Lange, Chemical solution routes to single-crystal thin films, Science, 273 (1996) 903-909.

[8] R.W. Schwartz, T. Schneller, R. Waser, Chemical solution deposition of electronic oxide films, C.R. Chim., 7 (2004) 433-461.

[9] H. Van den Rul, M. Van Bael, A. Hardy, K. Van Werde, J. Mullens, Aqueous Solution-Based Synthesis of Nanostructured Metal Oxides, in: T.-Y. Tseng, H.S. Nalwa (Eds.) Handbook of Nanoceramics and Their Based Nanodevices: Synthesis and Processing, American Scientific Publishers, 2009.

[10] T. Schneller, Simple Alkoxide Based Precursor Systems, in: T. Schneller, R. Waser, M. Kosec, D. Payne (Eds.) Chemical Solution Deposition of Functional Oxide Thin Films, Springer Vienna, 2013, pp. 3-28.

[11] J. Livage, M. Henry, C. Sanchez, Sol-gel chemistry of transition-metal oxides, Prog. Solid State Chem., 18 (1988) 259-341.

[12] M. Van Bael, A. Hardy, J. Mullens, Aqueous Precursor Systems, in: T. Schneller, R. Waser, M. Kosec, D. Payne (Eds.) Chemical Solution Deposition of Functional Oxide Thin Films, Springer, 2013.

[13] A. Hardy, J. D'Haen, M.K. Van Bael, J. Mullens, An aqueous solution-gel citratoperoxo-Ti(IV) precursor: synthesis, gelation, thermo-oxidative decomposition and oxide crystallization, J. Sol-Gel Sci. Technol., 44 (2007) 65-74.

[14] D. Nelis, K. Van Werde, D. Mondelaers, G. Vanhoyland, M.K. Van Bael, J. Mullens, L.C. Van Poucke, Synthesis of $SrBi_2Ta_2O_9$ (SBT) by means of a soluble Ta(V) precursor, Journal of the European Ceramic Society, 21 (2001) 2047-2049.

[15] D. Nelis, K. Van Werde, D. Mondelaers, G. Vanhoyland, H. Van den Rul, M.K. Van Bael, J. Mullens, L.C. Van Poucke, Aqueous solution-gel synthesis of strontium bismuth niobate ($SrBi_2Nb_2O_9$), Journal of Sol-Gel Science and Technology, 26 (2003) 1125-1129.

[16] K. Van Werde, G. Vanhoyland, D. Mondelaers, H. Den Rul, M.K. Van Bael, J. Mullens, L.C. Van Poucke, The aqueous solution-gel synthesis of perovskite $Pb(Zr_{1-x},Ti_x)O_3$ (PZT), J. Mater. Sci., 42 (2007) 624-632.

[17] A.K. Burrell, T.M. McCleskey, Q.X. Jia, Polymer-Assisted Deposition, in: T. Schneller, R. Waser, M. Kosec, D. Payne (Eds.) Chemical Solution Deposition of Functional Oxide Thin Films, Springer, 2013.

[18] G.F. Zou, J. Zhao, H.M. Luo, T.M. McCleskey, A.K. Burrell, Q.X. Jia, Polymer-assisted-deposition: a chemical solution route for a wide range of materials, Chem. Soc. Rev., 42 (2013) 439-449.

[19] D. Birnie, Spin Coating: Art and Science, in: T. Schneller, R. Waser, M. Kosec, D. Payne (Eds.) Chemical Solution Deposition of Functional Oxide Thin Film, Springer, 2013.

[20] S.L. Hellstrom, Basic models of spin coating, in, http://large.stanford.edu/courses/2007/ph210/hellstrom1/, October 2007.

[21] A. Seifert, F.F. Lange, J.S. Speck, Epitaxial-growth of $PbTiO_3$ thin-films on (001)$SrTiO_3$ from solution precursors, J. Mater. Res., 10 (1995) 680-691.

[22] M.G. Blamire, J.L. MacManus-Driscoll, N.D. Mathur, Z.H. Barber, The Materials Science of Functional Oxide Thin Films, Adv. Mater., 21 (2009) 3827-3839.

[23] Introduction to Pulsed Lased Deposition, in: http://www.andor.com/learning-academy/pulsed-laser-deposition-an-introduction-to-pulsed-laser-deposition.

[24] J. Schwarzkopf, R. Fornari, Epitaxial growth of ferroelectric oxide films, Prog. Cryst. Growth Charact. Mater., 52 (2006) 159-212.

[25] D.P. Norton, Synthesis and properties of epitaxial electronic oxide thin-film materials, Materials Science and Engineering: R: Reports, 43 (2004) 139-247.

[26] O.Y. Gorbenko, S.V. Samoilenkov, I.E. Graboy, A.R. Kaul, Epitaxial stabilization of oxides in thin films, Chem. Mater., 14 (2002) 4026-4043.

[27] M. Ohring, Materials Science of Thin Films: Deposition and Structure, second ed., Academic Press, San Francisco, 2002.

[28] D.L. Smith, Thin-Film Deposition: Principles and Practice, McGraw Hill, San Francisco, 1995.

[29] M.D. Biegalski, K. Dorr, D.H. Kim, H.M. Christen, Applying uniform reversible strain to epitaxial oxide films, Appl. Phys. Lett., 96 (2010).

[30] A.P. Chen, H.H. Zhou, Z.X. Bi, Y.Y. Zhu, Z.P. Luo, A. Bayraktaroglu, J. Phillips, E.M. Choi, J.L. MacManus-Driscoll, S.J. Pennycook, J. Narayan, Q.X. Jia, X.H. Zhang, H.Y. Wang, A New Class of Room-Temperature Multiferroic Thin Films with Bismuth-Based Supercell Structure, Adv. Mater., 25 (2013) 1028-1032.

[31] J.H. Lee, P. Murugavel, H. Ryu, D. Lee, J.Y. Jo, J.W. Kim, H.J. Kim, K.H. Kim, Y. Jo, M.H. Jung, Y.H. Oh, Y.W. Kim, J.G. Yoon, J.S. Chung, T.W. Noh, Epitaxial stabilization of a new multiferroic hexagonal phase of $TbMnO_3$ thin films, Adv. Mater., 18 (2006) 3125-+.

[32] J. Wang, J.B. Neaton, H. Zheng, V. Nagarajan, S.B. Ogale, B. Liu, D. Viehland, V. Vaithyanathan, D.G. Schlom, U.V. Waghmare, N.A. Spaldin, K.M. Rabe, M. Wuttig, R. Ramesh, Epitaxial BiFeO3 multiferroic thin film heterostructures, Science, 299 (2003) 1719-1722.

[33] K.M. Rabe, M. Dawber, C. Lichtensteiger, C.H. Ahn, J.M. Triscone, Modern Physics of Ferroelectrics: Essential Background, in: K.M. Rabe, C.H. Ahn, J.M. Triscone (Eds.) Physics of Ferroelectrics: A Modern Perspective, Springer Berlin Heidelberg, 2007, pp. 1-30.

[34] J.M. Rondinelli, N.A. Spaldin, Structure and Properties of Functional Oxide Thin Films: Insights From Electronic-Structure Calculations, Adv. Mater., 23 (2011) 3363-3381.

[35] R.J. Zeches, M.D. Rossell, J.X. Zhang, A.J. Hatt, Q. He, C.H. Yang, A. Kumar, C.H. Wang, A. Melville, C. Adamo, G. Sheng, Y.H. Chu, J.F. Ihlefeld, R.

Erni, C. Ederer, V. Gopalan, L.Q. Chen, D.G. Schlom, N.A. Spaldin, L.W. Martin, R. Ramesh, A Strain-Driven Morphotropic Phase Boundary in $BiFeO_3$, Science, 326 (2009) 977-980.

[36] M.A. Novojilov, O.Y. Gorbenko, I.E. Graboy, A.R. Kaul, H.W. Zandbergen, N.A. Babushkina, L.M. Belova, Perovskite rare-earth nickelates in the thin-film epitaxial state, Appl. Phys. Lett., 76 (2000) 2041-2043.

[37] P.A. Salvador, T.D. Doan, B. Mercey, B. Raveau, Stabilization of $YMnO_3$ in a perovskite structure as a thin film, Chem. Mater., 10 (1998) 2592-2595.

[38] A.F.M. dos Santos, A.K. Cheetham, W. Tian, X.Q. Pan, Y.F. Jia, N.J. Murphy, J. Lettieri, D.G. Schlom, Epitaxial growth and properties of metastable $BiMnO_3$ thin films, Appl. Phys. Lett., 84 (2004) 91-93.

[39] J.X. Zhang, R.J. Zeches, Q. He, Y.H. Chu, R. Ramesh, Nanoscale phase boundaries: a new twist to novel functionalities, Nanoscale, 4 (2012) 6196-6204.

[40] F. Zavaliche, H. Zheng, L. Mohaddes-Ardabili, S.Y. Yang, Q. Zhan, P. Shafer, E. Reilly, R. Chopdekar, Y. Jia, P. Wright, D.G. Schlom, Y. Suzuki, R. Ramesh, Electric field-induced magnetization switching in epitaxial columnar nanostructures, Nano Lett., 5 (2005) 1793-1796.

[41] H. Zheng, J. Wang, S.E. Lofland, Z. Ma, L. Mohaddes-Ardabili, T. Zhao, L. Salamanca-Riba, S.R. Shinde, S.B. Ogale, F. Bai, D. Viehland, Y. Jia, D.G. Schlom, M. Wuttig, A. Roytburd, R. Ramesh, Multiferroic $BaTiO_3$-$CoFe_2O_4$ nanostructures, Science, 303 (2004) 661-663.

[42] J.L. MacManus-Driscoll, Self-Assembled Heteroepitaxial Oxide Nanocomposite Thin Film Structures: Designing Interface-Induced Functionality in Electronic Materials, Adv. Funct. Mater., 20 (2010) 2035-2045.

[43] H.M. Zheng, F. Straub, Q. Zhan, P.L. Yang, W.K. Hsieh, F. Zavaliche, Y.H. Chu, U. Dahmen, R. Ramesh, Self-assembled growth of $BiFeO_3$-$CoFe_2O_4$ nanostructures, Adv. Mater., 18 (2006) 2747-+.

[44] H. Zheng, J. Wang, L. Mohaddes-Ardabili, M. Wuttig, L. Salamanca-Riba, D.G. Schlom, R. Ramesh, Three-dimensional heteroepitaxy in self-assembled BaTiO3-CoFe2O4 nanostructures, Appl. Phys. Lett., 85 (2004) 2035-2037.

[45] J.L. MaCmanus-Driscoll, P. Zerrer, H.Y. Wang, H. Yang, J. Yoon, A. Fouchet, R. Yu, M.G. Blamire, Q.X. Jia, Strain control and spontaneous phase ordering in

vertical nanocomposite heteroepitaxial thin films, Nat. Mater., 7 (2008) 314-320.

Chapter 3

BiFeO$_3$ thin films via aqueous solution deposition: a study of phase formation and stabilization

In this chapter we investigate the influence of different processing parameters on the phase formation and thermal stability of BiFeO$_3$ (BFO) films obtained via chemical solution deposition. Films deposited from aqueous solutions were subjected to various processing conditions influencing the stability of the BiFeO$_3$ perovskite phase followed by a thorough microstructural investigation. The formation of secondary phases in bismuth ferrite thin films is studied as a function of annealing temperature and time, film thickness, Bi excess and Ti substitution. Annealing at higher temperatures induces decomposition leading to a significant amount of secondary phases, particularly the iron-rich Bi$_2$Fe$_4$O$_9$ phase. Qualitative microstructural analysis of the films is performed by electron backscattered diffraction (EBSD) which provides phase analysis of individual grains. Nucleation of Bi$_2$Fe$_4$O$_9$ grains probably occurs at the film/substrate interface, after which grain growth continues towards the surface of the film through the depletion of the BiFeO$_3$ phase. Addition of Bi excess or the substitution of Fe with Ti in the precursor solutions significantly reduces the formation of an iron-rich secondary phase.

3.1 Introduction

Previous reports on the phase stability of the BFO thin films mainly refer to PLD processing conditions where deposition pressure and temperature play an

59

important role in the phase formation process while issues with impurities like Fe_2O_3 and Bi_2O_3, as well as bismuth oxide evaporation were reported [1-4]. On the other hand, research on the thermal stability of BFO thin films obtained via CSD and on the influence of processing parameters is rather limited [5, 6]. Particularly in solution chemistry, the thermal budget (pyrolysis and annealing times and temperatures, heating rates) and possible film-substrate interactions are important aspects of solution deposition [5-8].

This chapter reports an experimental study of the thermal stability and decomposition of BFO thin films obtained via water-based CSD. We identified processing parameters affecting the decomposition of $BiFeO_3$ followed by a thorough microstructural analysis of the acquired thin films and determination of the phases present. We also propose approaches to inhibiting the formation of secondary phases and improvement of the stability of BFO phase.

3.2 Aqueous chemical solution deposition of $BiFeO_3$ films

3.2.1 Solution synthesis

One of the main steps in chemical solution deposition of $BiFeO_3$ films is the synthesis of the precursor solution where selection of solvent and chemical reagents dictate further solution handling and thermal processing and finally microstructure and properties of the films. Many synthesis methods of BFO precursors depend on 2-methoxy-ethanol as a solvent which is very flexible for solubilization of a variety of compounds but it is also a highly teratogenic compound. [6, 9] On the other hand, water-based chemical solution deposition combines the advantages of chemical solution deposition and water as a solvent what makes it relatively low-cost and environmentally friendly method. Furthermore, intensive research based on this method in our research group proves its high versatility for creation of wide range of compositions and microstructures [10-15].

The synthesis of the $BiFeO_3$ precursor solution applied here is adopted from the procedure previously reported by Hardy et al. [16]. The general approach is that monometal ion starting materials are used as a source of each constituent metal

ion in the desired oxide. However, the preparation of stable aqueous metal ions solutions is not always straightforward since metal ions tend to hydrolyse and condensate forming precipitation. This phase segregation can prevent mixing of monometal ion solution in desired molar ratio and affect the final composition of the metal oxide. Stabilization of metal ions in aqueous solution is possible to achieve through complexation of metal ions what often requires strong electron donor ligand, such as citrate ligand. Furthermore, citric acid has the ability to act as a bridge between different metal ions [17]. By adjusting the pH value to 7, deprotonation of carboxylate groups of citric acid is expected to enhance the ion complaxation. Upon evaporation of water from the solution, which is the case during thin films deposition, a gelation process occurs via formation of ammonium bridges between carboxylate groups of the complexes and the excess of the citrates. As a result, a three dimensional network forms, trapping metal ions and in that way prevents their precipitation.

In this sense, aqueous BiFeO$_3$ precursor solutions are prepared by mixing stable citrate precursors of Bi(III) and Fe(III) in the desired molar ratio and increasing the pH to 7 by addition of ammonia, Figure 3.1. This resulted in a clear, stable dark solution in which the ratio of citric acid to total amount of metal ions was 1:1.
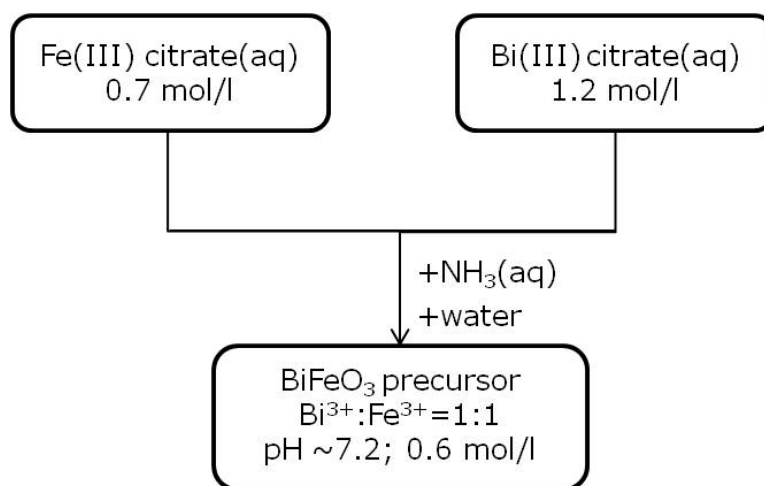
Figure 3.1: Schematic of BiFeO$_3$ synthesis route.

3.2.2 Thin film deposition and phase formation

Bismuth ferrite films were deposited from an aqueous solution-gel precursor on platinized silicon substrates, (Pt (80 nm)/TiO_x (30nm)/SiO_2/Si). Platinized silicon is widely used for ferroelectric oxide thin films as a substrate. This is due to relatively low cost and availability of Si, as well as its widespread technological application while platinum is used as bottom electrode as an inert material with a suitable thermal expansion coefficient. TiO_x is an adhesion layer between the Pt electrode and the silicon substrate

The $BiFeO_3$ precursor solution was spin coated on Pt/TiO_x/SiO_2/Si and each deposition step was followed by a hot plate treatment at 110°C (1 min), 260°C (2 min) while the final temperature was varied: 460°C, 470°C or 480°C (2 min). These hot plate steps were chosen based on the decomposition profile of $BiFeO_3$ precursor discussed in [16]. The thickness of the obtained films is controlled by the number of deposited layers.

X-ray diffraction (XRD) analysis reveals that $BiFeO_3$ films already crystallize around 470°C after a short thermal treatment of 2 minutes, as shown in Figure 3.2. This result is in agreement with Tyholdt et al. who reported the crystallization of 2-methoxyethanol-based BFO films between 460°C and 480°C [6]. The fact that crystallization from solution based precursors already starts at a lower temperature, in comparison with solid state methods (~600°C) [18], is intrinsically ascribed to the wet chemical method enhancing the mixing of metal ions at the molecular level, thereby decreasing diffusion distances and facilitating a low crystallization temperature [9].
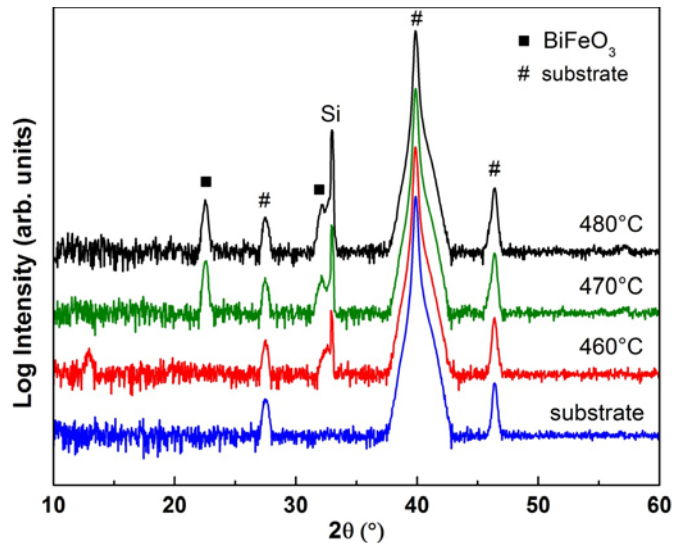
Figure 3.2: XRD results of the three-layered films after hot plate treatment. All three samples were treated at 110°C (1 min) and 260°C (2 min) while the final hot plate temperature was different for each of them: 460°C, 470° or 480°C for 2 minutes.

Based on these results, hot plate steps of 110°C (1 min), 260°C (2 min) and 480°C (2 min) were selected for the further processing of BFO films.

3.3 Influence of annealing temperature

In order to get insight into phase formation, growth and thermal stability of the stoichiometric BFO films, three-layered films were further annealed at 600°C, 650°C or 700°C for 1 hour in dry air. XRD results shown in Figure 3.3 confirm that the BFO phase with rhombohedral structure (JCPDS 86-1518) is present in all three films treated under these different thermal conditions. Films annealed at 600°C crystallized into the bismuth ferrite phase without any other secondary phase detectable within the instrumental sensitivity. An increase of temperature by 50°C did not introduce significant differences in the pattern.
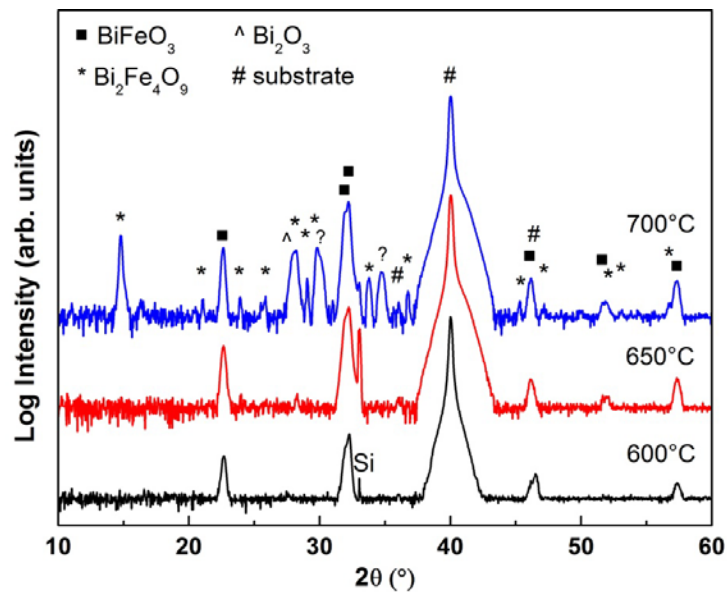
Figure 3.3: XRD patterns of the three-layered BFO films annealed at 600, 650 or 700°C for 1 hour in dry air.

Drastic changes in phase composition occurred after heat treatment at 700°C: a large portion of the iron rich $Bi_2Fe_4O_9$ has formed as a secondary phase. Furthermore, beside the phases detected above, additional peaks at $2\theta \approx 27.9°$ and $\approx 30°$ appearing as shoulders to the main reflections of $Bi_2Fe_4O_9$ ($2\theta = 28.21°$ and $29.7°$), as well as a peak at $2\theta \approx 34.8°$ point to the presence of other secondary phases in the films. Of these, the first two reflections could be correlated to a bismuth rich Bi_2O_3 or $Bi_{25}FeO_{39}$ phase. However, the reflection around $30°$ could also have its origin in some form of a Pt-Bi alloy, Pt-Bi-O compound or even in a $Bi_2Ti_2O_7$ phase together with the peak at $2\theta \approx 34.8°$ (marked with ?) [7, 19]. Figure 3.4 illustrates the effect of the annealing temperature on the film morphology. The film annealed at 600°C is polycrystalline with equiaxed grains, uniform, relatively smooth, with a low porosity and without cracks. However, after thermal treatment at 650°C, the SEM images reveal dark areas having a different morphology compared to the rest of the film which can probably be related to the onset of the BFO decomposition process. The morphological change is the most drastic in the

sample annealed at 700°C, where large, elongated grains of around 5 µm are embedded in the matrix of small, equiaxed grains.

Electron backscattered diffraction (EBSD) is used in conjunction with SEM imaging to perform a qualitative microstructural analysis of the films annealed at 700°C/1h, Figure 3.5a-c. According to the Kikuchi pattern (Figure 3.5b) obtained from the matrix (position 1), this part of the film is identified as BiFeO$_3$, while the patterns from the big, elongated grains (position 2 and 3) correspond to iron-rich Bi$_2$Fe$_4$O$_9$ (Figure 3.5c). The phase map in Figure 3.5d shows the bismuth ferrite grains in red, and the Bi$_2$Fe$_4$O$_9$ in blue. Inverse Pole Figure (IPF) maps for each phase separately are in reference to the normal direction where each individual orientation of crystals is colored differently, Figure 3.5e-f.
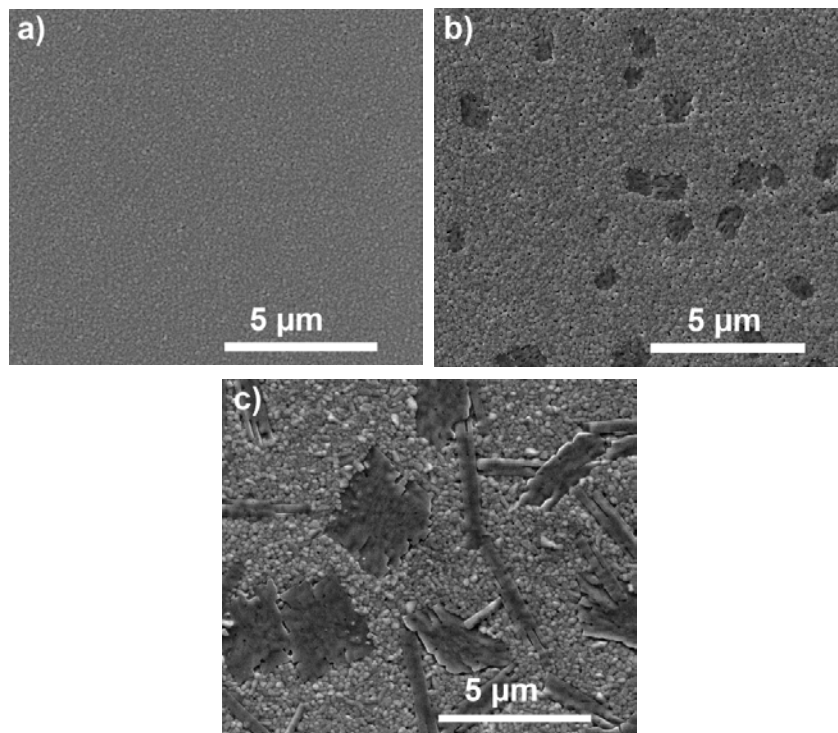
Figure 3.4: SEM images of the stoichiometric three-layered films annealed at a) 600°C, b) 650°C or c) 700°C for 1 hour.

Color coding for the orientations is presented in a Standard Stereographic Triangle (SST) [20]. The small grains are randomly oriented indicating the polycrystalline nature of the BFO film while the large grains of $Bi_2Fe_4O_9$ are single crystals that mainly exhibit (001) orientation (red-orange colour in the SST). Despite this thorough microstructure analysis, there is no evidence of Bi-rich phases although bismuth-rich compounds are detected by XRD analysis as one of the formed phases during the decomposition process (Figure 3.3). Furthermore, the detection limit of the diffraction analysis for Bi-rich phases should be lower since the concentration of heavy Bi ions is much higher in Bi_2O_3 or $Bi_{25}FeO_{39}$ than in compounds with the lighter Fe ion, such as $Bi_2Fe_4O_9$. It is possible that the Bi-rich phase is spread in the films as very fine grains or is segregated as a separate layer below the film, on the interface with the substrate [21].
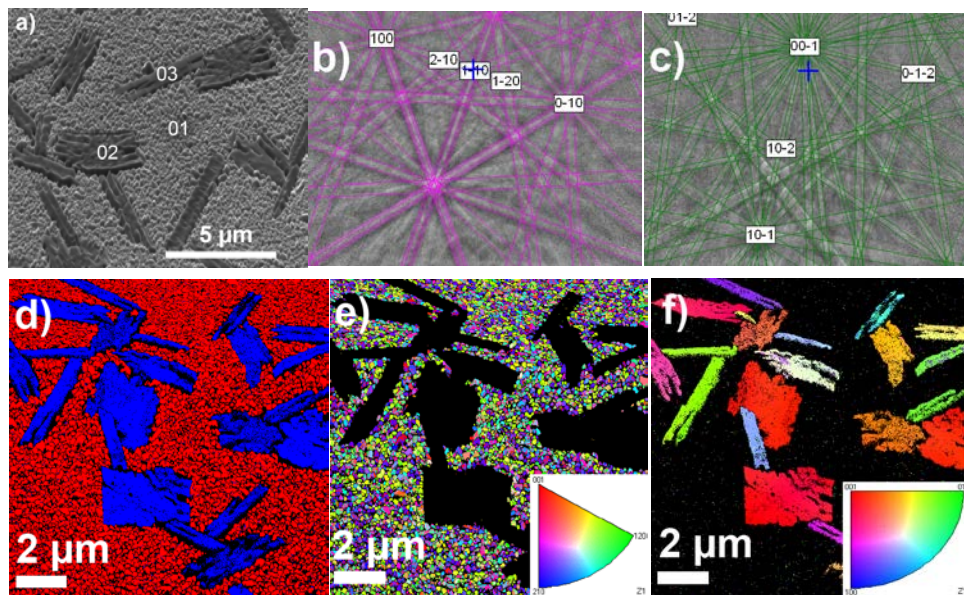
Figure 3.5: EBSD results of the three-layered BFO film after annealing at 700°C/1h: a) SEM image of the sample, b) Kikuchi pattern obtained at position 01: $BiFeO_3$, c) Kikuchi pattern obtained at position 02: $Bi_2Fe_4O_9$; d) phase map (red: $BiFeO_3$, blue: $Bi_2Fe_4O_9$), e) and f) are Inverse Pole Figure (IPF) maps for the $BiFeO_3$ and $BiFe_2O_4$ phase, respectively, in reference to normal direction with the color codes for individual orientations of crystals presented in Standard Stereographic Triangle (SST).

According to several reports where Bi-based films were deposited on substrates with a Pt bottom electrode, diffusion of Bi from the film into the substrate and its interaction with the platinum electrode result in the formation of an interfacial layer at the electrode-film interface [19, 22]. It is known that Bi reacts with Pt forming very stable intermetallic compounds [23] thus an interdiffusion layer between a Bi-based film and a Pt electrode can readily form at elevated temperatures [7, 19, 22]. A similar phenomenon was observed in case of Pb-based thin films obtained by CSD where different Pt-Pb intermetallic phases formed at elevated temperature [24, 25].

Based on the SEM and EBSD results in Fig. 3.4 and 3.5, respectively, it can be concluded that the decomposition process already starts at 650°C, where the dark areas in the SEM images (Figure 3.4b) are sites where nucleation of the iron rich Bi$_2$Fe$_4$O$_9$ phase starts and from where its large grains develop at 700°C. The observed decomposition onset of BFO films at 650°C is consistent with the BFO temperature metastable range around 450°C-770°C reported by Selbach et al. [26] for BFO bulk ceramics. The partial decomposition of the BFO phase into Bi-rich and Fe-rich phases in this temperature range can be explained by the more thermodynamically stable secondary phases in comparison to the BFO phase [26]. Further evidence of the instability of the BFO phase is the fact that decomposition is enhanced by increasing the annealing temperature to 700°C. Detection of large Bi$_2$Fe$_4$O$_9$ grains by SEM and EBSD in this study suggests a Bi deficiency occurring in the films during processing. In case of BFO ceramic, large Bi$_2$Fe$_4$O$_9$ grains observed at temperatures as high as 880°C are related to Bi$_2$O$_3$ loss due to evaporation during sintering [27] and are different from the Bi$_2$Fe$_4$O$_9$ grains that appear together with Bi-rich grains due to diffusion limitations during solid state synthesis [28, 29].

In order to get insight into and possibly extend the stability window of the BFO films towards 700°C, several experiments are performed taking into consideration the film thickness, annealing time, Bi excess and usage of an aliovalent substituent as parameters that could influence the phase stability of the obtained films.

3.4 Influence of film thickness

Due to the specific geometry of thin films *i.e.* their high surface to volume ratio and large exposed surface area, bismuth oxide, being a volatile compound, can evaporate much easier from a thin film than from bulk material during heat treatment. According to the phase diagram of $BiFeO_3$ (Figure 3.6), a Bi deficiency in the material could lead to the destabilization of the $BiFeO_3$ phase and the formation of iron-rich $Bi_2Fe_4O_9$ [30].
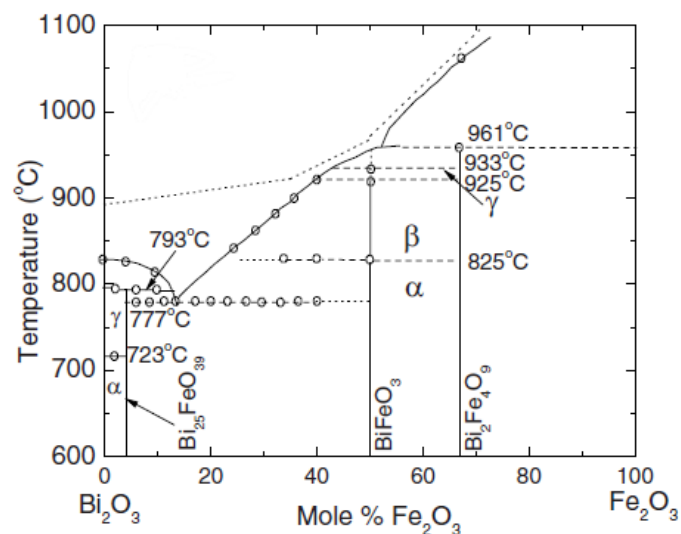
Figure 3.6: Phase diagram of Bi_2O_3-Fe_2O_3 system [30].

By changing the film thickness, the ratio of surface to volume is varied in order to explore their influence on the phase stability of BFO. For this study, one-, three-, six- and eight-layered films were deposited, annealed at 700°C for 1 hour and mutually compared. The thicknesses of the obtained films, measured in cross-sectional view with a scanning electron microscope, are around 30 nm, 80 nm, 150 nm and 220 nm for one-, three-, six- and eight-layered films, respectively. XRD patterns presented in Figure 3.7a show that, regardless of the film thickness, substantial amounts of secondary phases form. However, the most drastic change in phase composition occurs in the one-layered films, where $Bi_2Fe_4O_9$ appears as the primary phase with a preferred (001) orientation. At the same time, the decomposition is not complete since a few peaks of bismuth

ferrite are still present. Reflections at *2θ* ≈27.9° corresponding to a Bi-rich phase are only visible for the thicker films, while reflections from a possible Pt-Bi alloy are detected at a *2θ*≈30°, marked with (?) in Figure 3.7b.
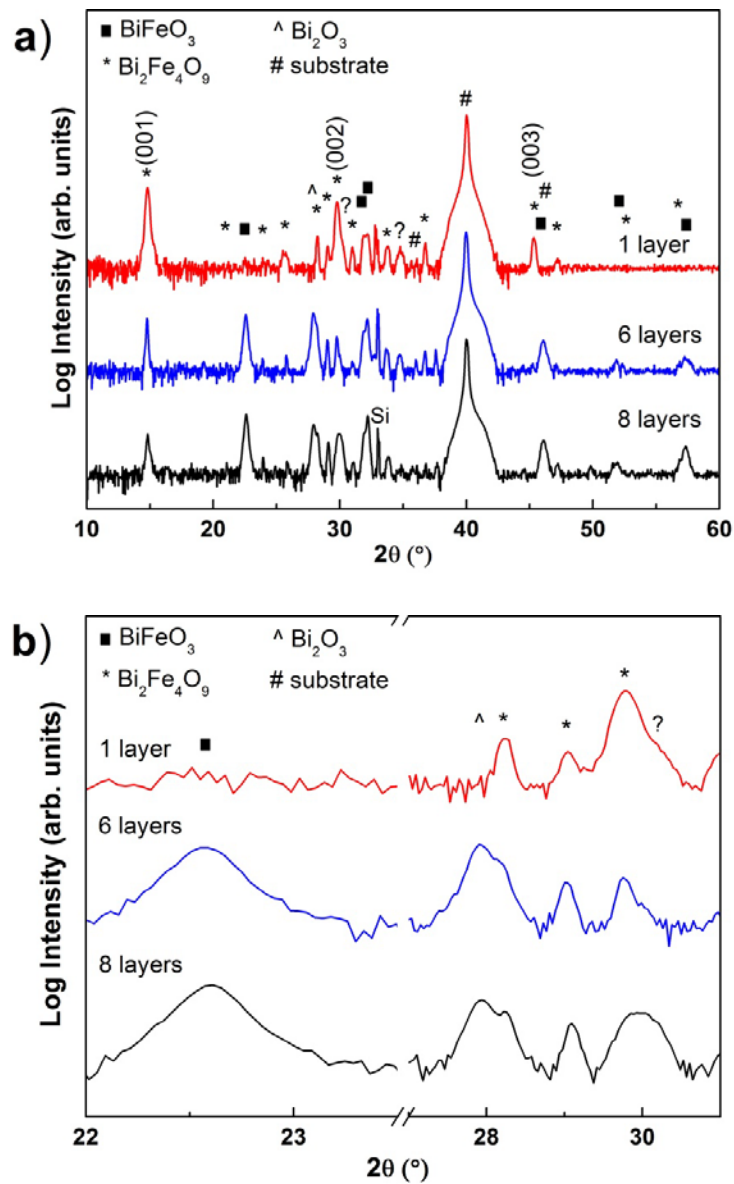
Figure 3.7: a) XRD patterns of BFO films obtained from one, six and eight layers, annealed at 700°C; b) Detail from the diffractograms in a).

A thicker film slightly stabilizes the BFO phase but also has a large impact on the morphology, as illustrated in Figure 3.8. The SEM micrograph of the one-layered film reveals a broken up layer consisting of small, equiaxed grains and larger structures differing in shape and size, which could be associated with the decomposition process and the formation of $Bi_2Fe_4O_9$. Such a heterogeneous morphology is in agreement with the XRD results (Figure 3.7). The secondary phase is also present in the microstructure of the six-layered samples in the form of plate-like grains roughly square in shape with an edge length up to 1 μm. In the case of eight-layered films, smaller and thicker plates of the iron rich phase are embedded in the BFO matrix. In general, well-defined $Bi_2Fe_4O_9$ grains of different morphologies are formed with a tendency towards a decreasing grain size with an increase of film thickness. Besides, the increasing thickness results in a gradual change of (001) preferred orientation of $Bi_2Fe_4O_9$ in one layered films to more randomly oriented grains after deposition of 8 layers. In the cross-sectional SEM images of the six- and eight-layered films in Figure 3.8, one observes that single-crystalline grains of the iron-rich phase grow through the whole film, and are not only present on the film surface. Nucleation of these $Bi_2Fe_4O_9$ grains probably occurs at the film/substrate interface, after which grain growth continues towards the film surface through the depletion of the bismuth ferrite phase. According to literature, $Bi_2Fe_4O_9$ crystals have a variable morphology and can be either sheet-, plate-, cube-, rod- or fiber-like depending on the processing parameters during the synthesis [31-35]. The possible explanation for this variety of crystal shapes can be found in the crystal structure of $Bi_2Fe_4O_9$ [31, 36]. Previous studies on orthorhombic $Bi_2Fe_4O_9$ showed that the dominating facets of $Bi_2Fe_4O_9$ crystal are (001), (110) and ($\bar{1}$10). Crystal growth occurs easily along the (001) plane, resulting in a sheet-like morphology with large facet (001). If the growth on (110) and ($\bar{1}$10) facets is suppressed and enhanced on the (001) facet, the growth rate difference between these facets decreases or disappears. As a result, the morphology of the $Bi_2Fe_4O_9$ crystal changes to a plate-like or to a cubic form.

In the same images, the interface between the Pt and the TiO_x adhesion layer beneath it can be studied. The thicknesses of the platinum and TiO_x layers vary locally along the sample. Furthermore, the interface between Pt and TiO_x is very rough in comparison with the bare $Pt/TiO_x/SiO_2/Si$ substrate itself (Figure 3.8f),

which could be the result of possible interactions of these layers with the BFO film, the formation of a Pt-Bi alloy or even the accumulation of Bi beneath the platinum layer. To corroborate our hypothesis and to be able to draw a conclusion from the interaction between Bi and the Pt substrate at elevated temperatures, we deposited an aqueous Bi citrate precursor with a 0.7 M concentration on the same substrate and repeated the same thermal treatment with the final annealing at 700°C for 1 hour.
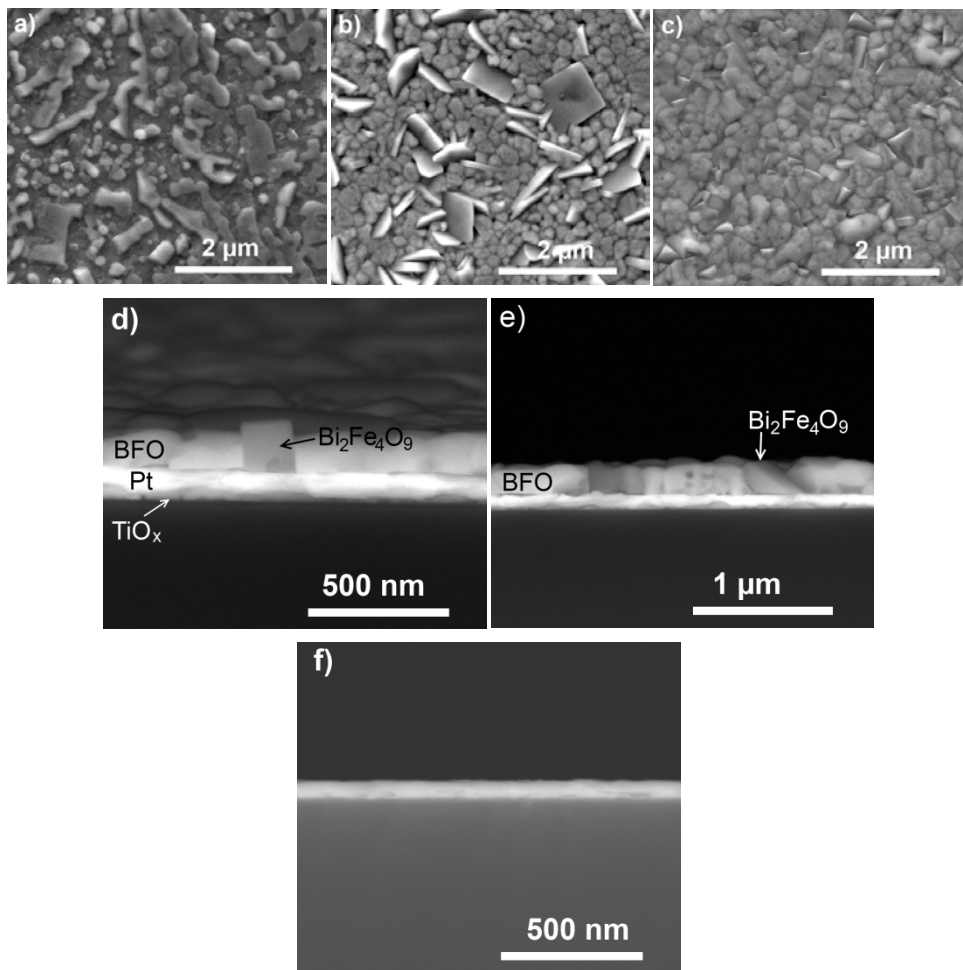
Figure 3.8: SEM surface images of BFO films annealed at 700°C with a) one, b) six or c) eight layers; Backscattered electron images of cross section of d) six- or e) eight-layered films and f) the Pt/TiO$_x$/SiO$_2$/Si substrate treated at 700°C.

A SEM micrograph of the obtained film and a backscattered electron image of the cross section are given in Figure 3.9. A discontinuous layer with island shaped structures of bismuth oxide and open, crater-like features on the Pt electrode are clearly visible in the plane-view SEM image, Figure 3.9a. These features indicate the strong interaction between the Pt electrode and the film and probably appear due to severe diffusion of bismuth through the electrode and its accumulation beneath the platinum, as shown in the cross-sectional image in Figure 3.9b.
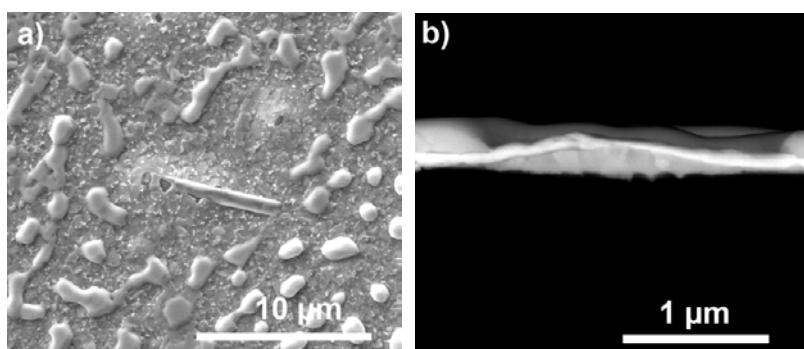
Figure 3.9: Film obtained from a Bi-citrate precursor (0.7 M) deposited on Pt/TiO$_x$/SiO$_2$/Si using the same thermal treatment at 700°C/1h as for the BFO films: a) Plane-view SEM micrograph; b) Cross-sectional backscattered image where the very bright layer is Pt electrode and dark area underneath is Bi-rich phase.

3.5 Influence of annealing time

To study the influence of the annealing time on the decomposition process, we exposed the stoichiometric, three-layered BiFeO$_3$ films to 700°C for different times (5, 10, 30, 60, 90 or 120 min) and afterwards analyzed the phase composition by X-ray diffraction. As Figure 3.10a shows, only a small amount of the Bi$_2$Fe$_4$O$_9$ secondary phase is present in the film after 10 min of heat treatment. With longer annealing times, the intensities of the Bi$_2$Fe$_4$O$_9$ (001) and (002) reflections at 2θ =14.7° and 29.7°, respectively show the most prominent increase. In addition to Bi$_2$Fe$_4$O$_9$, as a product of the BFO decomposition process, other secondary phases are also present in the samples as shown by
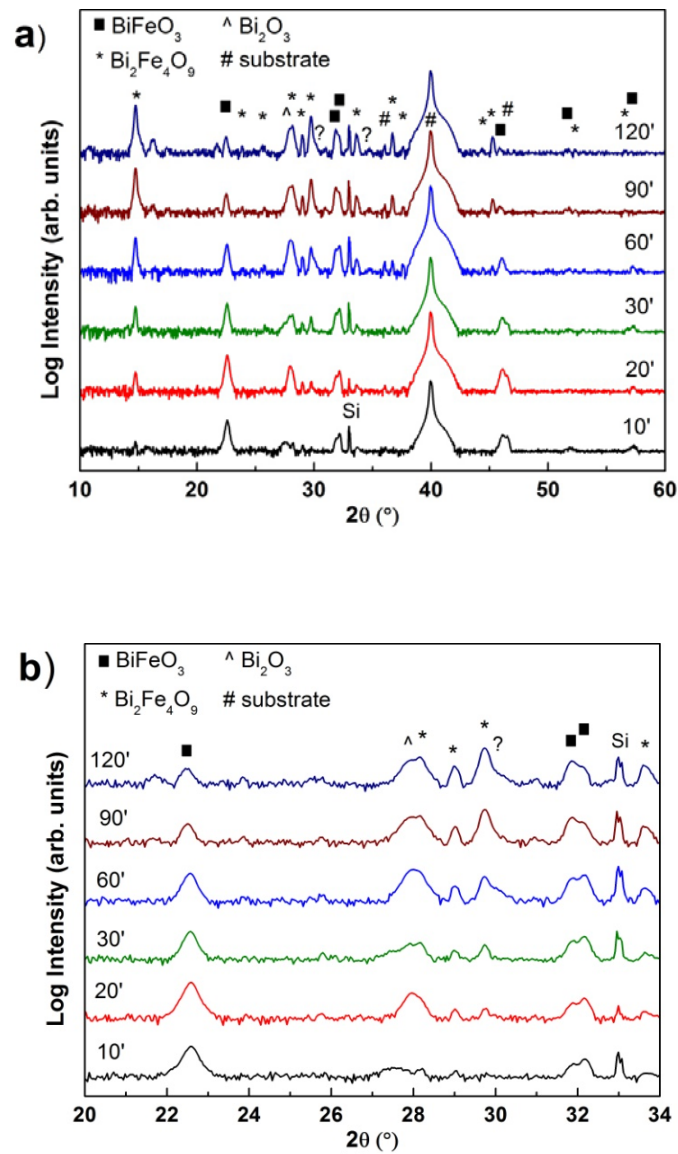
Figure 3.10: a) XRD patterns of three-layered BFO films annealed at 700°C for different times (10, 20, 30, 60, 90 or 120 minutes); b) Detail from the diffractogram in a).

the peaks in the *2θ* range 20°-34° in Fig. 3.10b. A closer examination of this pattern shows double peaks at *2θ* ≈28°, as well as a shoulder at ≈30° which probably arise from Bi-rich phases and the Pt-Bi alloy, respectively, as discussed above. As the annealing time increases, the integral intensities of the BiFeO$_3$ reflections decrease while the ones belonging to the iron rich Bi$_2$Fe$_4$O$_9$ phase

73

increase. According to these results, longer annealing times at 700°C enhance the decomposition process and thus the formation of secondary phases in the BFO films, as expected.
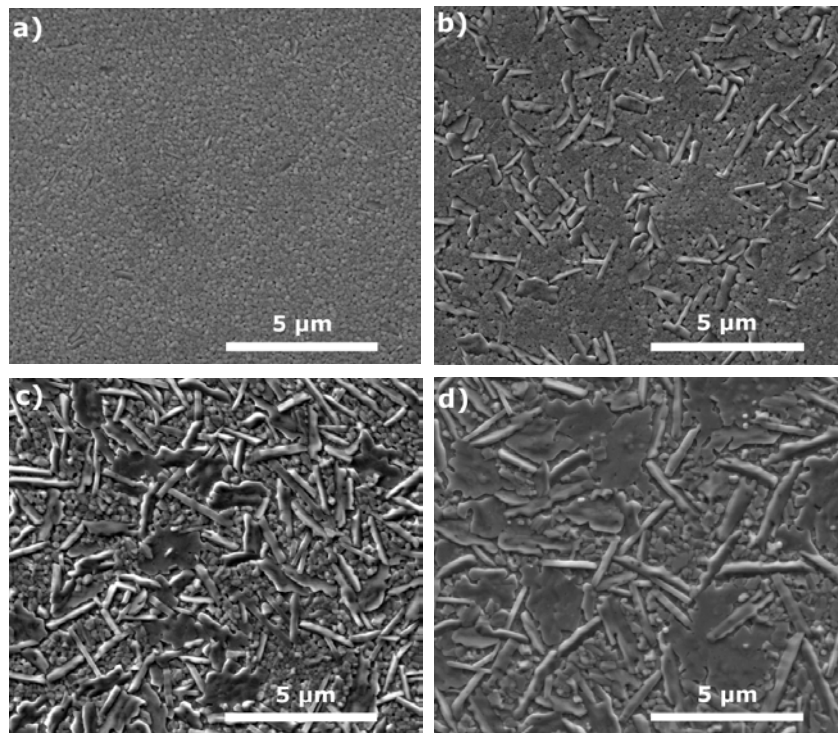
Figure 3.11: SEM images presenting the evolution of the film morphology with annealing time at 700°C: a) 10, b) 30, c) 90 or d) 120 minutes.

The fact that decomposition is enhanced by lengthening the annealing time at 700°C is a further evidence of the BFO phase instability. The observed influence of this parameter on phase stability is in agreement with the reports where the rate of BFO decomposition is determined by extended annealing time [30, 37].

3.6 Influence of Bi excess

Considering Bi evaporation from the film or Bi diffusion/reaction with the underlying Pt layer/TiO$_x$ layer as the origin for the secondary phase formation, a bismuth excess in the precursor is a possible step to prevent the decomposition of BFO [6, 38, 39]. According to Tyholdt et al., a bismuth excess of 10 at% Bi improves not only the stability of the BFO phase at elevated temperatures (700°C) but also the quality of the films in terms of density and porosity [6]. In our study, a significant amount of Bi$_2$Fe$_4$O$_9$ is present in the three-layered films with a 10 mol% Bi excess (Figure 3.12). On the other hand, applying 20 mol% or 30 mol% Bi excess in the precursor solutions, it is possible to suppress, at 700°C, the formation of the iron-rich phase of which reflections are no longer detected in the XRD patterns after heat treatment, as shown in Figure 3.12. However, peaks of other secondary phases, probably a Bi-rich phase and some form of Pt-Bi alloy (marked with ?) are still detected.
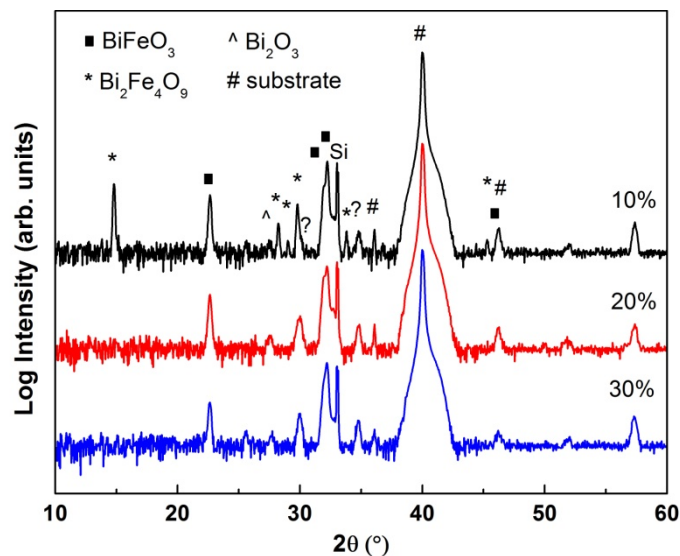
Figure 3.12: XRD patterns of three-layered films with a different Bi excess annealed at 700°C/1h.

The film with a 10% Bi excess has a very heterogeneous microstructure due to the decomposition leading to the formation of the iron-rich secondary phase, Figure 3.13a. Figures 3.13b and 3.13c show a remarkable improvement of the

microstructural homogeneity which is in accordance with the XRD results. In case of the films with 20 mol% and 30 mol% Bi excess the SEM images reveal more dense microstructures, although a few square-shaped grains, rich in iron, are still visible in films with a 20 mol% Bi excess.
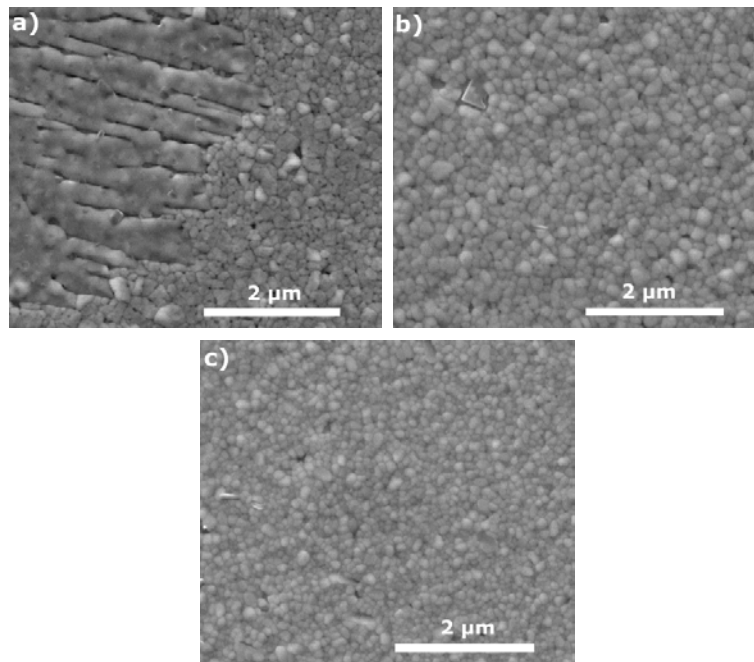
Figure 3.13: SEM micrographs of three-layered films with a) 10%, b) 20% or c) 30% Bi excess annealed at 700°C/1h.

For the films studied here the Bi_2O_3 deficiency is probably conditioned by the specific thin film geometry where both Bi_2O_3 diffusivity into the substrate and evaporation can occur during the thermal treatment in a gas flow [40]. We believe once the decomposition of BFO films is triggered within the temperature instability range of the $BiFeO_3$ phase it becomes further enhanced by diffusion of Bi^{3+} ions towards the substrate. Since higher diffusion rates of bismuth at elevated temperatures or prolonged annealing time increase Bi deficiency in the film, large amounts of secondary phases forms whereby Bi-rich phase segregates inside the substrate and Fe-rich phase remains in the films. Therefore, incorporation of Bi excess up to 30% in the precursor solution to compensate for the Bi_2O_3 loss resulted in a significantly lower amount of

secondary phases and improved BFO stability. This is in accordance with previous studies on Bi excess in chemical solution-deposited BFO films [5, 6] although the amount of Bi excess reported here is significantly higher.

3.7 Influence of substitution of Fe by Ti

Chemical substitution into perovskite BFO has mainly been used to improve electrical and magnetic properties of the material [41-46]. The substitution of Fe^{3+} by aliovalent Ti^{4+} results in a reduced leakage current. It is reported that titanium with a higher valence Ti^{4+} ion than Fe^{3+}, acts as a donor decreasing the concentration of oxygen vacancies [41, 47-49]. In our work, the effect of the addition of different amounts of Ti on the phase stability of bismuth ferrite films (BiFe$_{1-x}$Ti$_x$O$_3$, x=0.05, 0.1, 0.15 or 0.20) is studied. Noteworthy changes in the XRD patterns in Figure 3.14 are visible as the amount of Ti increases.
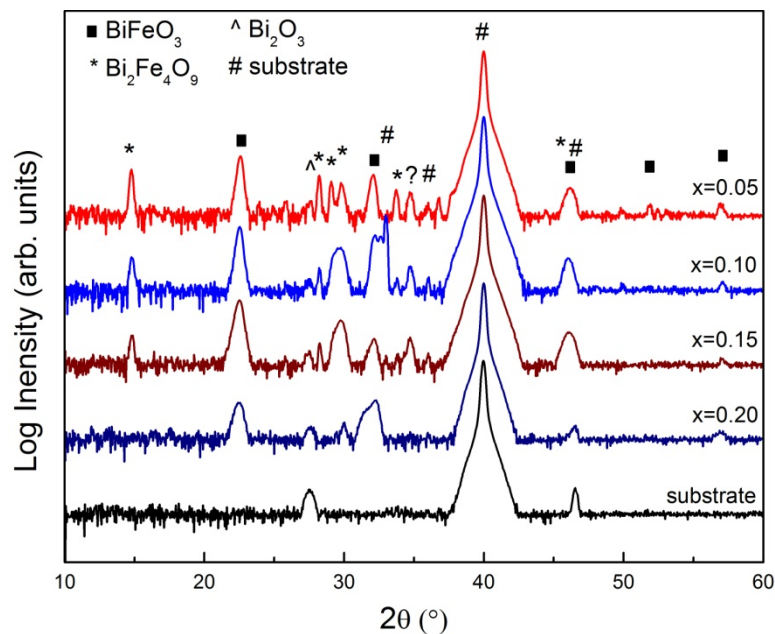
Figure 3.14: XRD patterns of BiFe$_{1-x}$Ti$_x$O$_3$, (x=0.05, 0.10, 0.15 or 0.20) films annealed at 700°C/1h.

Reflections belonging to an iron rich phase become less pronounced which implies that the presence of the Ti^{4+} ion in the system partially stabilizes the bismuth ferrite phase. The most prominent change is the complete disappearance of $Bi_2Fe_4O_9$ as a result of substitution with 20 mol% Ti. At the same time, with an increase of the Ti content towards $x=0.20$, the peak at $2\theta{\sim}32°$ associated with BFO becomes more broadened. This peak broadening is connected with a decreasing of average grain size below 100 nm, as AFM images in Figure 3.15 shows.

SEM images in Figure 3.16 reveal a slightly higher porosity in the Ti substituted films. Furthermore, the growth rate of the large iron-rich grains of the secondary phase at 700°C is significantly lower as the amount of Ti increases. Elongated grains of ~5 µm, appearing in the unsubstituted films, decrease to below 1 µm and finally disappear in those samples with the highest Ti concentration.
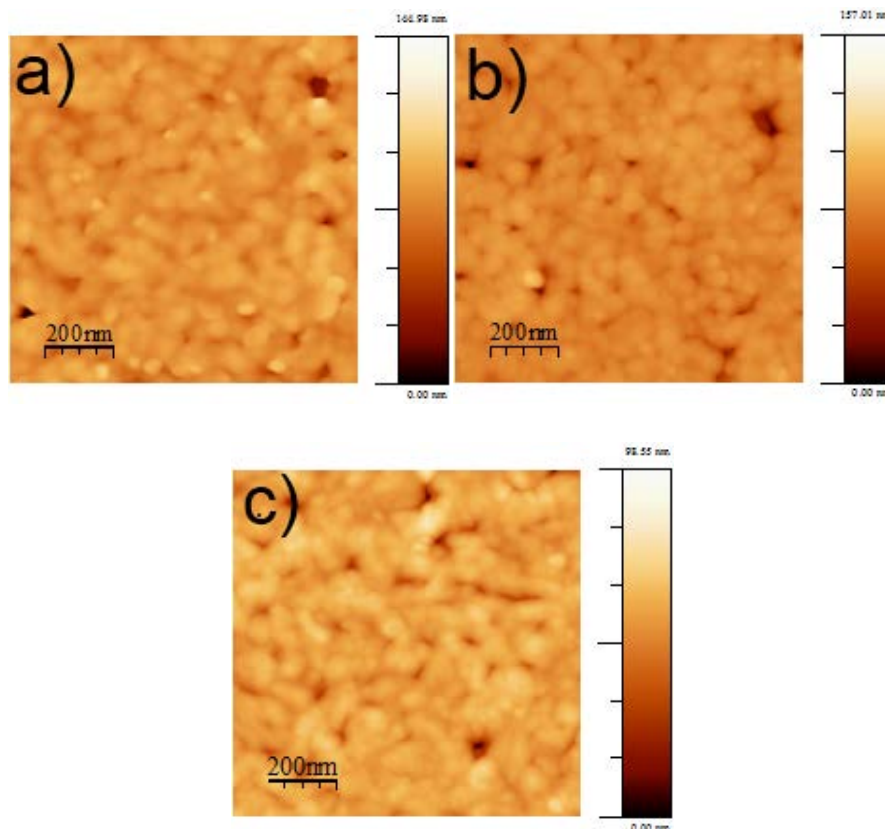
Figure 3.15: AFM images of $BiFe_{1-x}Ti_xO_3$ films annealed at 700°C/1h with a) $x=0.05$, b) 0.10 and c) 0.15
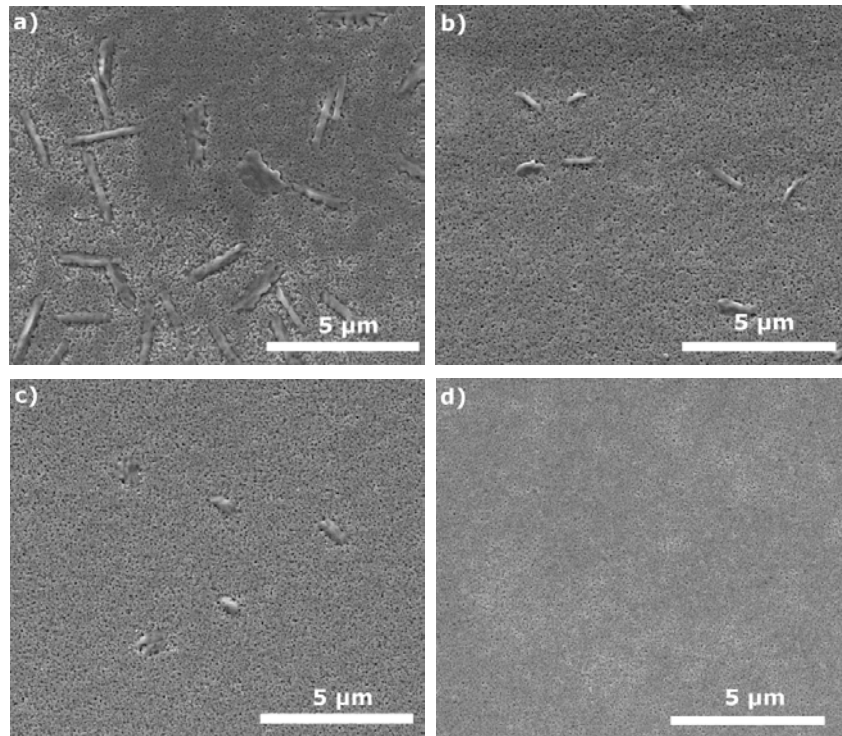
Figure 3.16: SEM micrographs of BiFe$_{1-x}$Ti$_x$O$_3$ films annealed at 700°C/1h with a) x=0.05, b) 0.10, c) 0.15 and d) 0.20.

Similar effects of Ti substitution on the growth of BiFeO$_3$ grains in bulk ceramics and thin films were found by several authors [50-54]. Bernardo et al. observed a positive effect of Ti substitution on the phase stabilization of BFO ceramics for classical solid state synthesis [50, 51]. The partial stabilization of BFO and the inhibition of grain growth are probably results of two phenomena: entering of Ti^{4+} ions inside the perovskite structure and segregation of Ti due to limited incorporation. As mentioned before, Ti^{4+} ions in the structure behave as a donor and thus can suppress the formation of oxygen vacancies which in turn limits the diffusion of matter resulting in a lower rate of grain growth [50, 53, 55]. Moreover, in a recent paper Bernardo and coauthors reported thorough microstructural analyses of Ti-doped ceramics [51]. Interestingly, they found clusters of nanometer-sized grains separated by Ti rich layers. Due to the segregation of Ti from the structure the Ti-rich areas are formed at the inner-

grain boundaries where they hinder the grain-boundaries mobility inhibiting the growth of grains. In ceramic processing, this type of grain-growth control is known as the solute-drag based mechanism [51].

These results suggest that substitution of Fe by aliovalent Ti can be used to prevent the compositional degradation of bismuth ferrite. Bernardo et al. reported on similar effect when Ti^{4+} is added into BFO ceramic [50, 51] although in studies of Valant et al. [56] the Ti^{4+} ion is considered as an impurity leading to the appearance of a larger fraction of the iron rich $Bi_2Fe_4O_9$ phase. The plausible explanation for the improved phase stability of Ti substituted films could be related to the limitation of bismuth diffusion due to reported segregation of titanium at the grain boundaries [51].

3.8 Magnetic properties

In order to study the influence of secondary phases and substitution of Fe by aliovalent Ti on the magnetic properties, three-layered BFO films annealed at 600°C/1h and 700°C/1h as well as $BiFe_{1-x}Ti_xO_3$ (where x=0.05; 0.20) films were subjected to SQUID measurements at 300 K with the magnetic field parallel to the film surface. The obtained magnetic hysteresis loops are presented in Figure 3.17. Both BFO films annealed at 600°C and 700°C show a weak ferromagnetic response. Bulk $BiFeO_3$ is an antiferromagnetic material with G-type magnetization and Néel temperature of 370°C [57-59]. However, in thin films, a weak ferromagnetic response is often reported in $BiFeO_3$ and is usually associated with canting of Fe atoms in the antiferromagnetic lattice [60, 61]. In comparison with the film treated at 600°C hysteresis loop of the BFO film annealed at 700°C exhibits lower magnetization values. The observed behavior could be explained by the combination of two effects: a lower amount of $BiFeO_3$ phase due to decomposition at 700°C as well as the presence of $Bi_2Fe_4O_9$ phase in the form of large grains as evidenced by XRD and SEM which exhibits paramagnetic behavior [62]. In case of $BiFe_{1-x}Ti_xO_3$ films (where x=0.05; 0.20) saturation magnetization decreases further in comparison to BFO films annealed at 700°C. Wang et al.[52] also observed weakened ferromagnetic orderings in Ti substituted films while Murari et al. [63] reported on paramagnetic behavior in BFO films substituted with 5% Ti, relating these results to the non-magnetic

80

nature of Ti^{4+} ions. In contrast with their films, $BiFe_{0.95}Ti_{0.05}O_3$ films in the study presented here comprise $Bi_2Fe_4O_9$ as secondary phase which should also be taken into account when comparing magnetic behavior. Also, the amount of this secondary phase in $BiFe_{0.80}Ti_{0.20}O_3$ films, according to XRD results, is almost negligible. As it is seen in Figure 3.17, compared with BFO film annealed at 700°C, saturation magnetization of Ti substituted films appears at lower fields which can be an evidence of altering magnetic properties by substitution of Fe with aliovalent Ti.
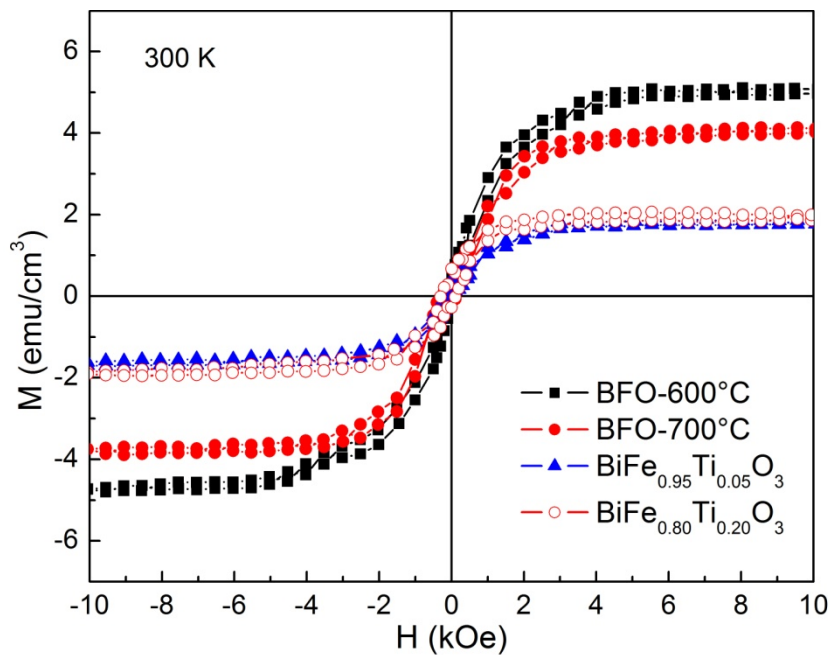
Figure 3.17: Magnetic hysteresis loops of $BiFeO_3$ films annealed at 600°C/700°C and $BiFe_{1-x}Ti_xO_3$ ($x \leq 0.2$) films annealed at 700°C measured at 300 K.

3.9 Conclusions

Our study on the thermal stability of $BiFeO_3$ films obtained by chemical solution deposition showed that a significant amount of the iron-rich $Bi_2Fe_4O_9$ phase formed at 700°C as a result of $BiFeO_3$ film decomposition. The obtained results suggest a loss of Bi from films at higher temperatures, possibly not only due to

volatilization but also due to high diffusion towards the substrate and possible interaction with the Pt electrode. In order to suppress the decomposition of $BiFeO_3$ and the formation of iron-rich phase, a shorter annealing time or the addition of Bi up to 30 mol% should be taken into account. Another approach for improving the stability of the BFO phase is substitution of Fe by aliovalent Ti where limitation of Bi diffusion probably occurs due to the inhibition of oxygen vacancy formation as well as segregation of titanium at the grain boundaries. These findings could be applicable not only to the other thin films with Bi-based compounds but also to films that contain other highly diffusible compounds when control over phase formation is crucial. Magnetic measurements revealed that presence of the $Bi_2Fe_4O_9$ secondary phase as well as substitution of Fe with Ti in BFO films leads to a decrease in saturation magnetization.

3.10 Experimental

3.10.1 Precursor synthesis

Bi(III) citrate precursor solution
Aqueous Bi(III) precursor was synthesized based on the procedure developed in our research group [11]. Bismuth citrate ($BiC_6H_5O_7$, 99.99%, Aldrich) was mixed with water, in which this compound has limited solubility and in order to enhance its dissolution ammonia (NH_3, 32% in H_2O, extra pure, Merck) was added. To prevent precipitation in this unstable solution, monoethanolamine ($NH_2(CH_2)_2OH$, 99.5 +%, Aldrich) was added in 1.5:1 molar ratio to Bi^{3+}. After stirring overnight, a light yellow, clear solution was filtrated using a 0.1 μm filter paper (Supor-100, Pall Life Sciences) and then diluted with water to the concentration of 1.2 M. The pH value was checked to be ~7. This bismuth citrate solution remained stable for several months.

Iron(III) citrate precursor solution
Water-based iron (III) precursor was obtained by refluxing the requested amount of Fe(III)citrate hydrate ($FeC_6H_5O_7 \cdot H_2O$, 98%, 18–20% Fe, Acros) in water at 80°C overnight [16]. The obtained dark solution was filtrated and upon

addition of water, the concentration was adjusted to ~0.7 M. The pH of this solution was 1.5 and it was not increased since Fe(OH)$_3$ tends to precipitate at higher pH [64].

BiFeO$_3$ precursor solution

Synthesis of BiFeO$_3$ precursor was based on the procedure by Hardy et al. [16]. The BiFeO$_3$ precursor solution was prepared as a multimetal ion solution by mixing Bi(III) and Fe(III) citrate solutions in the desired molar ratio followed by addition of ammonia (NH$_3$, 32% in H$_2$O, extra pure, Merck) and water in order to adjust the pH to 7.2 and concentration to ~0.6 M, respectively. The ratio of citric acid against total amount of metal ions was 1:1. Besides the stoichiometric BiFeO$_3$ solution, solutions with 10%, 20% and 30% Bi excess were prepared in this way as well.

When part of Fe(III) was substituted with Ti(IV), aqueous citratoperoxo-Ti(IV) precursor solution was used as a source of Ti(IV). Following the general procedure for BiFeO$_3$ precursors solution and adjusting the molar ratio of Fe(III) and Ti(IV), we obtained four different solutions as precursors for BiFe$_{1-x}$Ti$_x$O$_3$ (BFTO) with a total concentration of metal ions of 0.6 M, in which x=0.05, 0.10, 0.15 and 0.20.

Citratoperoxo-Ti(IV) precursor solution

The synthesis route for the aqueous citratoperoxo-Ti(IV) precursor solution was developed in our research group [65]. In the preparation of the citratoperoxo-Ti(IV) precursor with a ~0.7 M concentration of Ti(IV) first step was hydrolysis of titanium(IV)isopropoxide ((Ti(OC$_3$H$_7$)$_4$, 98%, Acros) in H$_2$O. As a result of hydrolysis and condensation reactions, a white precipitation was obtained and it was further thoroughly rinsed with water in order to remove byproducts of hydrolysis. In the second step, citric acid (C$_6$H$_8$O$_7$, 99.5%, Sigma Aldrich) and hydrogen peroxide (H$_2$O$_2$, 35 wt.-% in H$_2$O, p.a., stabilized, Acros) were added to this precipitate to obtain 2:1 and 1.2:1 molar ratio against Ti(IV), respectively. The round-bottom flask with this mixture was placed in an oil bath and its content was subjected to refluxing for 2 hour at 80°C. After cooling down to room temperature, the obtained dark red solution was adjusted to pH value of 7 by adding ammonia (NH$_3$, 32% in H$_2$O, extra pure, Merck) resulting in clear,

stable orange precursor. The precursor was further filtrated using a 0.1 μm filter paper (Supor-100, Pall Life Sciences) and final precursor concentration was adjusted by adding water to reach 100 ml.

3.10.2 Film deposition and thermal treatment

The solutions were filtered through a syringe filter of 0.2μm (Acrodisc Premium, Pall Life Sciences) onto the platinized silicon substrates (Pt/TiO$_x$/SiO$_2$/Si) which were thoroughly cleaned beforehand in SPM/APM (sulfuric acid peroxide mixture/ammonia peroxide mixture) to improve their wettability [66]. Thin layers were spin coated at a rotation speed of 3000 rpm for 30 s, with an acceleration of 1000 rpm/s. Each deposition step was followed by a hot plate treatment at 110°C (1 min), 260°C (2 min) and 480°C (2 min) in order to decompose the organic constituents. The thickness of the obtained films is controlled by the number of deposited layers. Finally, the films were subjected to an annealing process by inserting them into a preheated tube furnace at 600°C, 650°C or 700°C for different times in a dry air atmosphere using a gas flow of 0.5 l/min.

3.10.3 Characterization techniques

The exact concentration of the metal ion in the monometal precursors was determined by means of inductively coupled plasma atomic emission spectroscopy (ICP–AES, Optima 3300 DV, PerkinElmer). Samples were prepared by diluting the precursor solutions with 5% HNO$_3$ (J.T. Baker, 69-70%, Baker Instra-analyzed Reagent) so that the expected concentrations fall within the calibration range of 1 to 10 ppm.

The crystal structure of the obtained films was analyzed using a Bruker D8 Discover diffractometer operating in θ–2θ mode with the parallel beam geometry using a Göbel mirror (line focus, Cu K$_\alpha$ radiation). XRD diffractograms are shown on log scale along the y-axis to reveal much better the possible presence of secondary phases.

Thin film microstructure and morphology were examined using a scanning electron microscopy (FEI Quanta 200 FEG-SEM) equipped with secondary electron (SE) and back scattering electron (BSE) detectors. More information about crystalline material was obtained with electron backscattered diffraction (EBSD) system (Oxford Instruments with NordlysII detector). For this purpose, the SEM images were taken under EBSD conditions i.e. sample was tilted ~70° with respect to the horizontal axes which allows more electrons to be forward scattered and to escape towards the detector.

The topography analysis of the films on perovskite-based substrates was performed by means of the atomic force microscope (Veeco Dimension Microscope AFM with Digital Instrument Nanoscope III controller) in tapping mode using a Si cantilever tip.

Magnetic response of the samples was measured by superconducting quantum interface device (SQUID) magnetometer of Quantum Design MPMSXL-5 with a reciprocating sample option (RSO) head at 300 K in plane with the thin films. This part of research is done in collaboration with Prof. Margriet Van Bael, Lab. voor Vaste-Stoffysica en Magnetisme and with Prof. Kristiaan Temst, Instituut voor Kern-en Stralingsfysica, KU Leuven.

References

[1] H. Bea, M. Bibes, A. Barthelemy, K. Bouzehouane, E. Jacquet, A. Khodan, J.P. Contour, S. Fusil, F. Wyczisk, A. Forget, D. Lebeugle, D. Colson, M. Viret, Influence of parasitic phases on the properties of $BiFeO_3$ epitaxial thin films, Appl. Phys. Lett., 87 (2005).

[2] H. Bea, M. Bibes, S. Fusil, K. Bouzehouane, E. Jacquet, K. Rode, P. Bencok, A. Barthelemy, Investigation on the origin of the magnetic moment of $BiFeO_3$ thin films by advanced X-ray characterizations, Physical Review B, 74 (2006).

[3] H. Toupet, F. Le Marrec, J. Holc, M. Kosec, P. Vilarhino, M.G. Karkut, Growth and thermal stability of epitaxial BiFeO3 thin films, J. Magn. Magn. Mater., 321 (2009) 1702-1705.

[4] S. Fujino, M. Murakami, S.H. Lim, M. Wuttig, L.G. Salamanca-Riba, I. Takeuchi, Ferroelectric properties of multiphase Bi-Fe-O thin films, Solid State Ionics, 178 (2007) 1257-1261.

[5] M.D. Casper, M.D. Losego, J.P. Maria, Optimizing phase and microstructure of chemical solution-deposited bismuth ferrite ($BiFeO_3$) thin films to reduce DC leakage, J. Mater. Sci., 48 (2013) 1578-1584.

[6] F. Tyholdt, S. Jorgensen, H. Fjellvag, A.E. Gunnaes, Synthesis of oriented BiFeO3 thin films by chemical solution deposition: Phase, texture, and microstructural development, J. Mater. Res., 20 (2005) 2127-2139.

[7] M.L. Calzada, A. Gonzalez, J. Garcia-Lopez, R. Jimenez, Crystallization, heterostructure, microstructure, and properties of ferroelectric strontium bismuth tantalate films derived from tantalum glycolate solutions, Chem. Mater., 15 (2003) 4775-4783.

[8] R.W. Schwartz, Chemical solution deposition of perovskite thin films, Chem. Mater., 9 (1997) 2325-2340.

[9] R.W. Schwartz, T. Schneller, R. Waser, Chemical solution deposition of electronic oxide films, C.R. Chim., 7 (2004) 433-461.

[10] C. De Dobbelaere, A. Hardy, J. D'Haen, H. Van den Rul, M.K. Van Bael, J. Mullens, Morphology of water-based chemical solution deposition (CSD) lead titanate films on different substrates: Towards island formation, J. Eur. Ceram. Soc., 29 (2009) 1703-1711.

[11] A. Hardy, D. Mondelaers, M.K. Van Bael, J. Mullens, L.C. Van Poucke, G. Vanhoyland, J. D'Haen, Synthesis of (Bi,La)$_4$Ti$_3$O$_{12}$ by a new aqueous solution-gel route, J. Eur. Ceram. Soc., 24 (2004) 905-909.

[12] D. Nelis, M.K. Van Bael, H. Van den Rul, J. Mullens, L.C. Van Poucke, G. Vanhoyland, J. D'Haen, W. Laureyn, D.J. Wouters, Ferroelectric SrBi$_2$Nb$_2$O$_9$ thin films by aqueous chemical solution deposition, Integr. Ferroelectr., 45 (2002) 205-213.

[13] I. Truijen, M.K. Van Bael, H. Van den Rul, J. D'Haen, J. Mullens, Synthesis of thin dense titania films via an aqueous solution-gel method, J. Sol-Gel Sci. Technol., 41 (2007) 43-48.

[14] H. Van den Rul, D. Mondelaers, M.K. Van Bael, J. Mullens, Water-based wet chemical synthesis of (doped) ZnO nanostructures, J. Sol-Gel Sci. Technol., 39 (2006) 41-47.

[15] K. Van Werde, G. Vanhoyland, D. Nelis, D. Mondelaers, M.K. Van Bael, J. Mullens, L.C. Van Poucke, Phase formation of ferroelectric perovskite 0.75 Pb(Zn$_{1/3}$,Nb$_{2/3}$)O$_3$-0.25 BaTiO$_3$ prepared by aqueous solution-gel chemistry, J. Mater. Chem., 11 (2001) 1192-1197.

[16] A. Hardy, S. Gielis, H. Van den Rul, J. D'Haen, M.K. Van Bael, J. Mullens, Effects of precursor chemistry and thermal treatment conditions on obtaining phase pure bismuth ferrite from aqueous gel precursors, J. Eur. Ceram. Soc., 29 (2009) 3007-3013.

[17] Y. Narendar, G.L. Messing, Synthesis, decomposition and crystallization characteristics of peroxo-citrato-niobium: An aqueous niobium precursor, Chem. Mater., 9 (1997) 580-587.

[18] V.S. Filip'ev, N.P. Smolyaninov, E.G. Fesenko, I.N. Belyaev, Synthesis of BiFeO$_3$ and determination of the unit cell, Kristallografiya, 5 (1960) 958.

[19] M.L. Calzada, R. Jimenez, A. Gonzalez, J. Garcia-Lopez, D. Leinen, E. Rodriguez-Castellon, Interfacial phases and electrical characteristics of ferreoelectric strontium bismuth tantalate films on Pt/TiO$_2$ and Ti/Pt/Ti heterostructure electrodes, Chem. Mater., 17 (2005) 1441-1449.

[20] D. Stojakovic, Electron backscatter diffraction in materials characterization, Processing and Application of Ceramics, 6 (2012) 1-13.

[21] F. Tyholdt, H. Fjellvag, A.E. Gunnaes, A. Olsen, Synthesis of epitaxial $BiFeO_3$ films by chemical solution deposition on Pt(100), J. Appl. Phys., 102 (2007).

[22] S. Yakovlev, J. Zekonyte, C.H. Solterbeck, M. Es-Souni, Interfacial effects on the electrical properties of multiferroic $BiFeO_3$/Pt/Si thin film heterostructures, Thin Solid Films, 493 (2005) 24-29.

[23] H. Okamoto, The Bi-Pt (Bismuth-Platinum) system, J. Phase Equilib., 12 (1991) 207-210.

[24] I. Bretos, R. Jimenez, E. Rodriguez-Castellon, J. Garcia-Lopez, M.L. Calzada, Heterostructure and compositional depth profile of low-temperature processed lead titanate-based ferroelectric thin films prepared by photochemical solution deposition, Chem. Mater., 20 (2008) 1443-1450.

[25] A.C. Dippel, T. Schneller, R. Waser, D. Park, J. Mayer, Formation Sequence of Lead Platinum Interfacial Phases in Chemical Solution Deposition Derived $Pb(Zr_{1-x}Ti_x)O_3$ Thin Films, Chem. Mater., 22 (2010) 6209-6211.

[26] S.M. Selbach, M.A. Einarsrud, T. Grande, On the Thermodynamic Stability of $BiFeO_3$, Chem. Mater., 21 (2009) 169-173.

[27] T. Rojac, M. Kosec, B. Budic, N. Setter, D. Damjanovic, Strong ferroelectric domain-wall pinning in $BiFeO_3$ ceramics, J. Appl. Phys., 108 (2010).

[28] M.S. Bernardo, T. Jardiel, M. Peiteado, A.C. Caballero, M. Villegas, Reaction pathways in the solid state synthesis of multiferroic $BiFeO_3$, J. Eur. Ceram. Soc., 31 (2011) 3047-3053.

[29] T. Rojac, A. Bencan, B. Malic, G. Tutuncu, J.L. Jones, J.E. Daniels, D. Damjanovic, $BiFeO_3$ Ceramics: Processing, Electrical, and Electromechanical Properties, J. Am. Ceram. Soc., 97 (2014) 1993-2011.

[30] R. Palai, R.S. Katiyar, H. Schmid, P. Tissot, S.J. Clark, J. Robertson, S.A.T. Redfern, G. Catalan, J.F. Scott, beta phase and gamma-beta metal-insulator transition in multiferroic $BiFeO_3$, Physical Review B, 77 (2008).

[31] X. Zhang, L. Bourgeois, J. Yao, H. Wang, P.A. Webley, Tuning the morphology of bismuth ferrite nano- and microcrystals: From sheets to fibers, Small, 3 (2007) 1523-1528.

[32] J.T. Han, Y.H. Huang, X.J. Wu, C.L. Wu, W. Wei, B. Peng, W. Huang, J.B. Goodenough, Tunable synthesis of bismuth ferrites with various morphologies, Adv. Mater., 18 (2006) 2145.

[33] Q.J. Ruan, W.D. Zhang, Tunable Morphology of Bi$_2$Fe$_4$O$_9$ Crystals for Photocatalytic Oxidation, J. Phys. Chem. C, 113 (2009) 4168-4173.

[34] C.J. Tsai, C.Y. Yang, Y.C. Liao, Y.L. Chueh, Hydrothermally grown bismuth ferrites: controllable phases and morphologies in a mixed KOH/NaOH mineralizer, J. Mater. Chem., 22 (2012) 17432-17436.

[35] Z.T. Hu, B. Chen, T.T. Lim, Single-crystalline Bi$_2$Fe$_4$O$_9$ synthesized by low-temperature co-precipitation: performance as photo- and Fenton catalysts, Rsc Advances, 4 (2014) 27820-27829.

[36] X.Y. Zhang, J. Lv, L. Bourgeois, J.W. Cui, Y.C. Wu, H.T. Wang, P.A. Webley, Formation and photocatalytic properties of bismuth ferrite submicrocrystals with tunable morphologies, New J. Chem., 35 (2011) 937-941.

[37] M.I. Morozov, N.A. Lomanova, V.V. Gusarov, Specific features of BiFeO$_3$ formation in a mixture of bismuth(III) and iron(III) oxides, Russ. J. Gen. Chem., 73 (2003) 1676-1680.

[38] A. Lahmar, K. Zhao, S. Habouti, M. Dietze, C.H. Solterbeck, M. Es-Souni, Off-stoichiometry effects on BiFeO$_3$ thin films, Solid State Ionics, 202 (2011) 1-5.

[39] S.K. Singh, H. Funakuba, H. Uchida, H. Ishiwara, Structural and electrical properties of BiFeO3 thin films, Integr. Ferroelectr., 76 (2005) 139-146.

[40] S.M. Selbach, T. Tybell, M.A. Einarsrud, T. Grande, Phase transitions, electrical conductivity and chemical stability of BiFeO3 at high temperatures, J. Solid State Chem., 183 (2010) 1205-1208.

[41] K. Kalantari, I. Sterianou, S. Karimi, M.C. Ferrarelli, S. Miao, D.C. Sinclair, I.M. Reaney, Ti-Doping to Reduce Conductivity in Bi$_{0.85}$Nd$_{0.15}$FeO$_3$ Ceramics, Adv. Funct. Mater., 21 (2011) 3737-3743.

[42] S. Yasui, H. Uchida, H. Nakaki, K. Nishida, H. Funakubo, S. Koda, Analysis for crystal structure of Bi(Fe,Sc)O$_3$ thin films and their electrical properties, Appl. Phys. Lett., 91 (2007).

[43] C.F. Chung, J.P. Lin, J.M. Wu, Influence of Mn and Nb dopants on electric properties of chemical-solution-deposited BiFeO$_3$ films, Appl. Phys. Lett., 88 (2006).

[44] D. Do, J.W. Kim, S.S. Kim, Effects of Dy and Mn Codoping on Ferroelectric Properties of BiFeO$_3$ Thin Films, J. Am. Ceram. Soc., 94 (2011) 2792-2795.

[45] F. Yan, M.O. Lai, L. Lu, T.J. Zhu, Enhanced Multiferroic Properties and Valence Effect of Ru-Doped $BiFeO_3$ Thin Films, J. Phys. Chem. C, 114 (2010) 6994-6998.

[46] V.A. Khomchenko, D.A. Kiselev, M. Kopcewicz, M. Maglione, V.V. Shvartsman, P. Borisov, W. Kleemann, A.M.L. Lopes, Y.G. Pogorelov, J.P. Araujo, R.M. Rubinger, N.A. Sobolev, J.M. Vieira, A.L. Kholkin, Doping strategies for increased performance in $BiFeO_3$, J. Magn. Magn. Mater., 321 (2009) 1692-1698.

[47] X.D. Qi, J.H. Dho, M. Blamire, Q.X. Jia, J.S. Lee, S. Foltyn, J.L. MacManus-Driscoll, Epitaxial growth of $BiFeO_3$ thin films by LPE and sol-gel methods, J. Magn. Magn. Mater., 283 (2004) 415-421.

[48] Y. Wang, Q.H. Jiang, H.C. He, C.W. Nan, Multiferroic $BiFeO_3$ thin films prepared via a simple sol-gel method, Appl. Phys. Lett., 88 (2006).

[49] J.G. Wu, J. Wang, Ferroelectric and Impedance Behavior of La- and Ti-Codoped $BiFeO_3$ Thin Films, J. Am. Ceram. Soc., 93 (2010) 2795-2803.

[50] M.S. Bernardo, T. Jardiel, M. Peiteado, A.C. Caballero, M. Villegas, Sintering and microstructural characterization of W^{6+}, Nb^{5+} and Ti^{4+} iron-substituted $BiFeO_3$, J. Alloys Compd., 509 (2011) 7290-7296.

[51] M.S. Bernardo, T. Jardiel, M. Peiteado, F.J. Mompean, M. Garcia-Hernandez, M.A. Garcia, M. Villegas, A.C. Caballero, Intrinsic Compositional Inhomogeneities in Bulk Ti-Doped $BiFeO_3$: Microstructure Development and Multiferroic Properties, Chem. Mater., 25 (2013) 1533-1541.

[52] Y. Wang, C.W. Nan, Enhanced ferroelectricity in Ti-doped multiferroic $BiFeO_3$ thin films, Appl. Phys. Lett., 89 (2006).

[53] C.D. Zheng, J. Yu, D.M. Zhang, B. Yang, Y.Y. Wu, L.H. Wang, Y.B. Wang, W.L. Zhou, Processing and ferroelectric properties of Ti-doped $BiFeO_3$ ceramics, Integr. Ferroelectr., 94 (2007) 31-36.

[54] G.D. Hu, S.H. Fan, C.H. Yang, W.B. Wu, Low leakage current and enhanced ferroelectric properties of Ti and Zn codoped $BiFeO_3$ thin film, Appl. Phys. Lett., 92 (2008).

[55] H.M. Chan, M.P. Harmer, D.M. Smyth, Compensating defects in highly donor-doped $BaTiO_3$, J. Am. Ceram. Soc., 69 (1986) 507-510.

[56] M. Valant, A.K. Axelsson, N. Alford, Peculiarities of a solid-state synthesis of multiferroic polycrystalline $BiFeO_3$, Chem. Mater., 19 (2007) 5431-5436.

[57] A. Palewicz, R. Przenioslo, I. Sosnowska, A.W. Hewat, Atomic displacements in BiFeO$_3$ as a function of temperature: neutron diffraction study, Acta Crystallographica Section B-Structural Science, 63 (2007) 537-544.

[58] S.M. Selbach, T. Tybell, M.A. Einarsrud, T. Grande, The Ferroic Phase Transitions of BiFeO$_3$, Adv. Mater., 20 (2008) 3692-+.

[59] J. Wang, J.B. Neaton, H. Zheng, V. Nagarajan, S.B. Ogale, B. Liu, D. Viehland, V. Vaithyanathan, D.G. Schlom, U.V. Waghmare, N.A. Spaldin, K.M. Rabe, M. Wuttig, R. Ramesh, Epitaxial BiFeO$_3$ multiferroic thin film heterostructures, Science, 299 (2003) 1719-1722.

[60] H. Bea, M. Bibes, S. Petit, J. Kreisel, A. Barthelemy, Structural distortion and magnetism of BiFeO$_3$ epitaxial thin films: A Raman spectroscopy and neutron diffraction study, Philos. Mag. Lett., 87 (2007) 165-174.

[61] C. Ederer, N.A. Spaldin, Weak ferromagnetism and magnetoelectric coupling in bismuth ferrite, Physical Review B, 71 (2005).

[62] Z.M. Tian, S.L. Yuan, X.L. Wang, X.F. Zheng, S.Y. Yin, C.H. Wang, L. Liu, Size effect on magnetic and ferroelectric properties in Bi$_2$Fe$_4$O$_9$ multiferroic ceramics, J. Appl. Phys., 106 (2009).

[63] N.M. Murari, R. Thomas, R.E. Melgarejo, S.P. Pavunny, R.S. Katiyar, Structural, electrical, and magnetic properties of chemical solution deposited BiFe$_{1-x}$Ti$_x$O$_3$ and BiFe$_{0.9}$Ti$_{0.05}$Co$_{0.05}$O$_3$ thin films, J. Appl. Phys., 106 (2009).

[64] J. Kragten, Atlas of Metal–Ligand Equilibria in Aqueous Solution, Horwood, Chichester, England, 1978.

[65] A. Hardy, J. D'Haen, M.K. Van Bael, J. Mullens, An aqueous solution-gel citratoperoxo-Ti(IV) precursor: synthesis, gelation, thermo-oxidative decomposition and oxide crystallization, J. Sol-Gel Sci. Technol., 44 (2007) 65-74.

[66] M.K. Van Bael, D. Nelis, A. Hardy, D. Mondelaers, K. Van Werde, J. D'Haen, G. Vanhoyland, H. Van den Rul, J. Mullens, L.C. Van Poucke, F. Frederix, D.J. Wouters, Aqueous chemical solution deposition of ferroelectric thin films, Integr. Ferroelectr., 45 (2002) 113-122.

Chapter 4

Influence of the substrate on the thermal stability of BiFeO$_3$ thin films

In the previous chapter, it was shown that BiFeO$_3$ films deposited on platinized silicon substrates tend to decompose at higher temperatures and interact with the substrate. Therefore, various substrates and buffer layers were investigated in terms of film/substrate interactions and their effect on thermal stability of BiFeO$_3$ thin film and obtained results are presented in this chapter. The aim was to identify appropriate substrates for processing BiFeO$_3$ films at elevated temperature such that film/substrate interaction and possible formation of secondary phase as a result of this interaction would be minimized. Magnetic response of the obtained BiFeO$_3$ films to an applied magnetic field at 2 K and 300 K was investigated by SQUID measurements.

4.1 Introduction

Besides deposition techniques, an important factor in the processing of thin films is the choice of an appropriate substrate. As discussed in Chapter 2, one of the benefits of structural and dimensional resemblance between thin film and substrate is epitaxial stabilization of metastable phases or compounds that are not achievable in form of powders or bulk but only as thin films [1]. Considering issues with phase formation and decomposition, the example where phase stabilization could benefit from the substrate-induced strain in epitaxial films is bismuth ferrite, BiFeO$_3$. Thus, in their studies on the effect of parasitic phases on BiFeO$_3$ film properties, Béa et al. found that epitaxial strain influences the stabilization of the BFO phase on (001) SrTiO$_3$ substrate for film thicknesses up

to 70 nm at slightly higher deposition pressure at 580°C during PLD [2]. Another report, but on $BiFeO_3$-$CoFe_2O_4$ composite multiferroics by Dix et al. showed the importance of appropriate substrate or buffer-layer selection for epitaxial stabilization of different $BiFeO_3$ phases in thin films. Thus, growth of tetragonal $BiFeO_3$ occurs preferentially on (001) $LaAlO_3$ substrate, while (001) $SrTiO_3$ substrate and $LaNiO_3$-buffered $LaAlO_3$ substrates promote the growth of the rhombohedral phase. With a further increase in lattice parameters in case of cubic substrates, such as $MgAl_2O_4$ and MgO, decomposition of $BiFeO_3$ occurs resulting in formation of Bi-rich dendritic structures [3].

Another important aspect in the selection of suitable substrates for thin film deposition concerns film/substrate interactions. In order to reach optimal morphology and structure that would lead to desired material properties, chemical solution processing of metal oxide thin films often requires relatively high temperatures [4-6]. In this sense the use of various substrates can be limited due to possible interactions with the film. A number of undesired effects were reported such as delamination of the substrate, diffusion of constituent elements from the film towards the substrate (especially highly diffusible elements like Bi or Pb), reactions between film and substrate, formation an interfacial layer, etc. [7-14]. Furthermore, the "loss" of these elements from the films due to their high diffusibility at elevated temperatures can lead to additional formation of secondary phases in the films [5]. Thus, in terms of temperature limitation, the choice of an appropriate substrate or selected buffer layers is an important factor in the processing of thin films.

In this chapter, we present a thorough study of the influence of various substrates and buffer layers on the thermal stability of $BiFeO_3$ thin films obtained by chemical solution deposition. We looked at two opposite aspects of substrate behavior: a tendency towards interaction with the film which increases formation of secondary phases versus the stabilization of the $BiFeO_3$ phase at elevated temperatures.

4.2 Films on silicon based substrates

Silicon based substrates are selected in part due to relatively low cost and availability of Si, as well as the widespread technological application of this substrate. Phase formation and thermal stability of three-layered BiFeO$_3$ films on silicon based substrates are investigated by annealing the films at two different temperatures, 600°C and 700°C. Since thermal treatment of the BFO films on platinized silicon substrates at 600°C and 700°C resulted in significant differences in the microstructure and phase formation, these two temperatures were chosen for the further film processing on the other silicon based substrates.

4.2.1 Structure and morphology

Although thorough structural and microstructural analysis of the films on platinized silicon wafers is given in chapter 3, some of the results are reconsidered for the sake of easier comparison among the substrates. The XRD patterns in Figure 4.1 show that the BFO phase forms at 600°C without detectable secondary phases, regardless of the type of substrates used for deposition, SiO$_2$/Si, Al$_2$O$_3$/Si or Pt/TiO$_2$/SiO$_2$/Si.

In the SEM micrographs in Figure 4.2, in the case of Al$_2$O$_3$-coated and regular silicon substrates, clustering and broken up layers are visible. On the other hand the film on platinized silicon substrate has a rather dense, smooth surface. After increasing the annealing temperature to 700°C, dramatic changes occur both in the structure and the morphology of the films. Secondary phase formation is very pronounced in all three cases, yet the types of secondary phases differ. Interaction between the film and silicon substrate results in complete decomposition of BiFeO$_3$ giving Bi$_2$SiO$_5$ and hematite Fe$_2$O$_3$ as new products. Also, thin films deposited on Al$_2$O$_3$/Si show a different phase composition after annealing at 700°C. In this case the BFO phase has become negligible, while new phases are detected, namely Bi$_2$Fe$_4$O$_9$ and Fe$_2$O$_3$. It is possible that the Al$_2$O$_3$ coating reacted with the film so that Al ions are now incorporated in Bi$_2$Fe$_4$O$_9$ as an impurity, giving Bi$_2$Fe$_{4-x}$Al$_x$O$_9$. According to Valant et al., who

deliberately added small amounts of Al_2O_3 impurities in the mixture of Bi_2O_3 and Fe_2O_3 powders, this type of impurity tends to promote the formation of the $Bi_2Fe_4O_9$ secondary phase [15]. SEM images in Figure 4.3 show a very heterogeneous microstructure with different types of grains in films on silicon substrates, while the film on Al_2O_3/Si transformed to an almost continuous layer with few pores where it is difficult to distinguish the grains and grain boundaries, except for a few laminar outgrowths. Significant amounts of an iron-rich $Bi_2Fe_4O_9$ phase formed together with some Bi-rich phases in films deposited on Pt electrode. Concerning the microstructure, these films consists of small, equiaxed grains that belong to $BiFeO_3$ and big, elongated grains of $Bi_2Fe_4O_9$ embedded in the $BiFeO_3$ matrix.
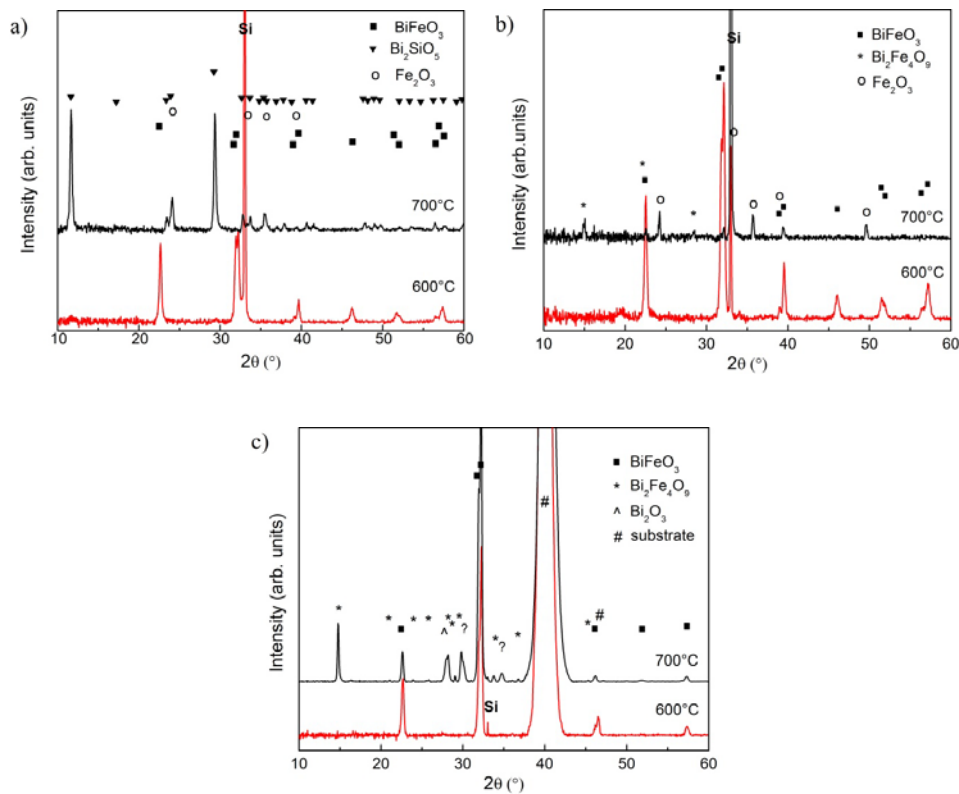
Figure 4.1: XRD analysis of the films annealed at 600°C or 700°C for 1 hour on different substrates: a) SiO_2/Si, b) Al_2O_3/Si and c) $Pt/TiO_2/SiO_2$/Si.
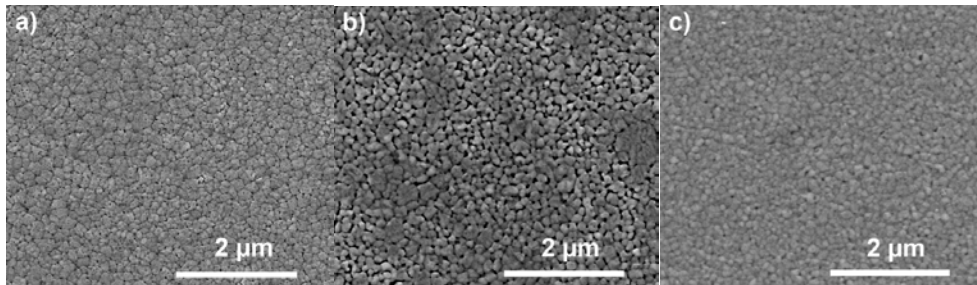
Figure 4.2: Top-view SEM images of the films annealed at 600°C on a) SiO$_2$/Si, b) Al$_2$O$_3$/Si and c) Pt/TiO$_2$/SiO$_2$/Si.
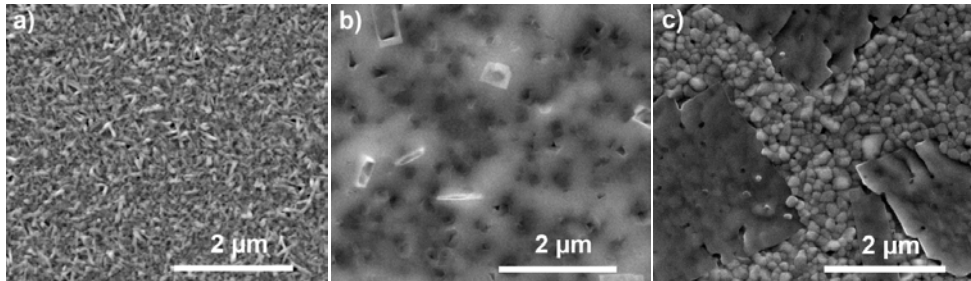
Figure 4.3: Top-view SEM images of the films annealed at 700°C on a) SiO$_2$/Si, b) Al$_2$O$_3$/Si and c) Pt/TiO$_2$/SiO$_2$/Si.

4.2.2 RBS and AES analyses

Further evaluation of the interaction between film and Al$_2$O$_3$/Si substrate was accomplished using Rutherford backscattering spectrometry (RBS) and Auger Electron Spectroscopy (AES) analyses. Rutherford backscattering spectrometry, as an ideal tool for analysis of thin layers up to a few microns thick, is used to provide depth-resolved elemental composition of BFO films annealed at 700°C on alumina coated silicon substrates. Figure 4.4 shows experimental RBS data (black circles) of the three-layered film together with a simulated spectrum (solid red line). The simulated graph represents an RBS spectrum without taking interdiffusion into account and is shown for comparison reasons. The Bi and Fe signals show a strong lowering of their low energy side, indicating a diffusion of these cations towards the Si substrate. The substrate Si edge is split into two steps, one remaining the bulk Si interface, the other one at higher energies

points to the formation of a secondary phase layer. It should be emphasized here that although the RBS signal arising from Si or Al (from the buffer aluminate layer) at this position cannot be distinguished, considering the very low Al content, the overwhelming part of the signal can be attributed to Si. Both these edges show a smooth decrease which results from the interdiffusion of the secondary phase and Si substrate.
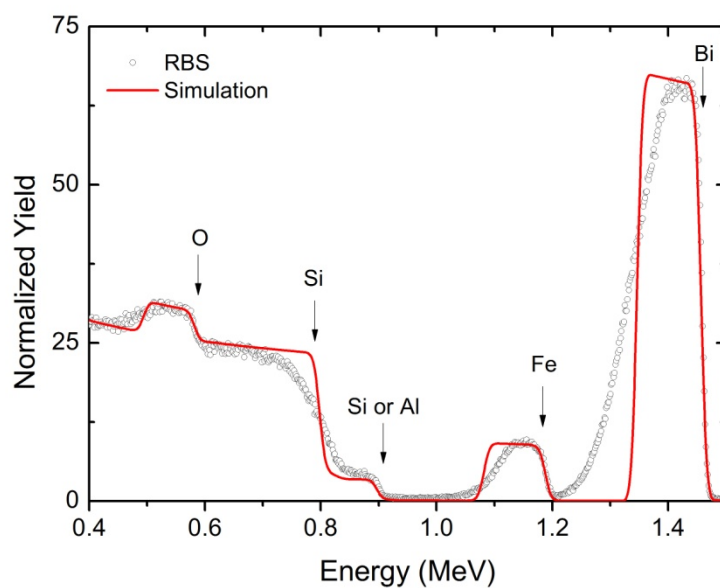
Figure 4.4: RBS spectra of three-layered BFO thin film on alumina coated silicon substrates annealed at 700°C.

The RBS findings were consistent with AES analysis. As a surface-sensitive technique, AES allows for the rapid determination of the elemental composition of a small region of the material surface [16]. Figure 4.5 shows an AES surface survey on the film annealed at 700°C on alumina coated silicon substrates. In this differential spectrum peaks of Si, Al and Fe are observed together with the peaks associated with some common surface contaminants. The presence of Si and Al peaks in the AES surface spectrum suggests that there was Si and Al

diffusion through the entire film thickness to the surface at this annealing temperature.

In terms of the silicon detected on the film surface on Al$_2$O$_3$/Si substrate, this can be related to the diffusion of silicon atoms from the substrate into the film. It is possible that after interaction Al$_2$O$_3$ layer and BiFeO$_3$ films, Al$_2$O$_3$ layer is degraded and its role as the barrier layer would be negligible. Without the barrier layer, the obstacles for thermal diffusion of silicon atoms into the film are decreased. Diffusion of silicon from the substrate into the film have been reported for different metal oxide films deposited via CSD as a consequence of high temperature processing [17-19].
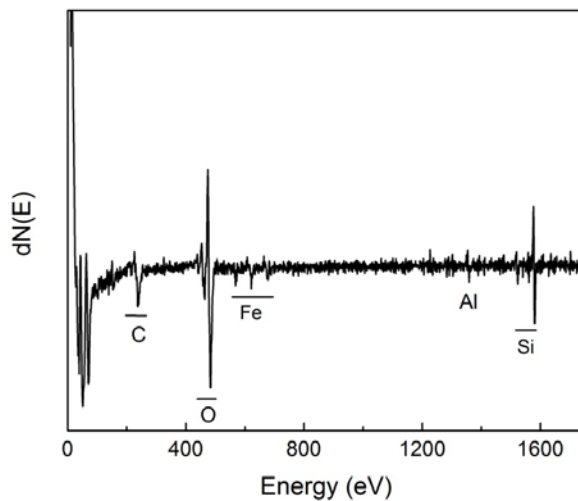
Figure 4.5: AES spectra of a three-layered BFO thin film on alumina coated silicon substrates annealed at 700°C.

Both RBS and AES analyses were performed on different spots of the same sample and on different samples, as well. Results obtained from these measurements are comparable.

Here, BFO films deposited on the silicon-based substrates were in direct contact with three different top layers on the substrates itself, SiO$_2$, Pt or Al$_2$O$_3$.

Formation of secondary phases as result of decomposition of the BFO phase at 700°C as well as the resulting film microstructure was strongly influenced by type of materials the film was in contact with. As discussed in chapter 1, decomposition of BFO films on $Pt/TiO_x/SiO_2/Si$, but also on SiO_2/Si or Al_2O_3/Si could be related to the thermal instability of BFO phase in a temperature interval from 450° to 770°C under ambient atmosphere [20]. However, the formed secondary phases tend to interact with the substrates in a different way, where Bi_2SiO_5 forms when SiO_2/Si is used, and iron-rich phase when Al_2O_3/Si is used. Plausible explanation for the formation of these phases could be found in the work of Valant et al. [15] who investigated the influence of impurities on the BFO phase formation followed by thermodynamics explanation. They found that small amount of impurities (<1 wt%) such as SiO_2 or Al_2O_3 in the mixture of Bi_2O_3 and Fe_2O_3 powders enhance formation of significant amount of thermodynamically stabilized Bi-rich and Bi-poor secondary phases (several tens of vol%) due to solubility of the impurities in these phases. Thus, when SiO_2 is present as an impurity, it tends to react to form sillenite phase $Bi_{12}SiO_{20}$ which is isostructural to $Bi_{25}FeO_{39}$ phase. In the case of Al_2O_3, this type of impurity promotes the formation of Al-containing $Bi_2Fe_4O_9$ secondary phase [15]. Furthermore, Rojac et al. [21] as well as Bucci et al. [22] showed that, BFO powders or ceramics tend to react at contact surfaces with substrates/crucibles during thermal treatments. Since the refractory materials usually contain silicon or alumina, the observed composition degradation of BFO at such contacts can be also related to the 'impurity' effect. With regard to SiO_2/Si or Al_2O_3/Si substrates presented here, we believe that decomposition of BFO initiated due to instability of BFO phase at 700°C is further enhanced by the reaction of one of secondary phases with the substrates.

4.3 Films on single crystal substrates

In addition to Si, single crystal oxides with a perovskite structure such as $(001)_{pc}$-oriented $LaAlO_3$ (LAO) and $SrTiO_3$ (STO) as well as (0001)-oriented sapphire (Al_2O_3) were used as the substrates for deposition of BFO films.

4.3.1 Perovskite based substrates

The choice of substrates was based on their crystal structure and lattice compatibility with BiFeO$_3$, all of which affect the film strain and structural disorder [23]. The use of substrates with a higher level of lattice matching and of the similar crystallographic structure as perovskite film would be expected to decrease value of $f(\theta)$ in equiation 2.2, as discussed in the chapter 2. This would lower the energy barrier for nucleation at the substrate interface compared to nucleation within the bulk of the film [24]. LAO substrate has a rhombohedral structure with a pseudocubic lattice parameter a = 3.79 Å, while the structure of an STO substrate is cubic with lattice parameter a = 3.905 Å.

According to X-ray diffraction analysis performed in conventional θ-2θ scans, films deposited on (001)$_{pc}$-oriented LAO and STO substrates crystallized into the bismuth ferrite phase at 700°C annealing temperature without any other secondary phase detectable within instrumental sensitivity, as shown in Figure 4.6. Reflections in the patterns, (001) and (002) belong to BiFeO$_3$ indicating highly oriented films along the c-axis of the pseudo-cubic cell. However, very small reflections visible at 2θ =31.8° and 32° (shown as an insets in the graphs in Figure 4.6) point to some degree of polycrystalline growth.
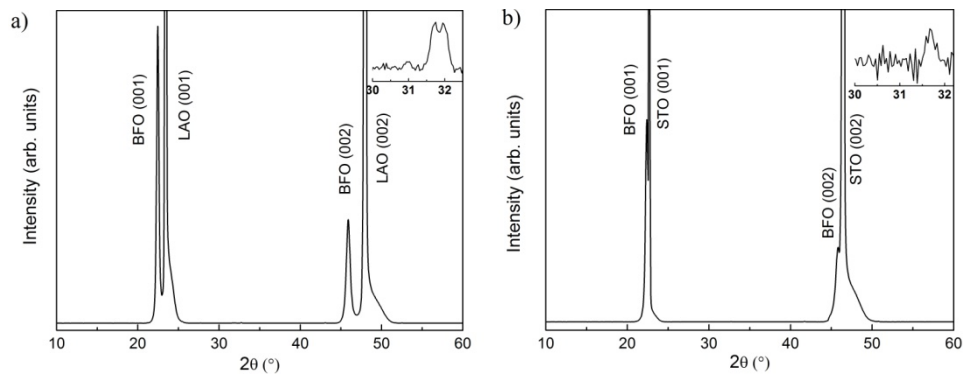
Figure 4.6: XRD analysis of BFO films annealed at 700°C on perovskite-based substrates: a) (001) LaAlO$_3$ and b) (001) SrTiO$_3$ substrate. Insets show details from the XRD patterns where the present peaks results from polycrystalline BiFeO$_3$ grains.

From the omega-rocking curves in Figure 4.7, the values of the full width at half maximum (FWHM) of (001) peaks were found to be similar, 1.09° and 1.12° for

BFO films both on LAO and STO substrate, respectively. These values indicate a certain degree of mosaic character of the films due to misorientation of crystallites.

To get insight into the in-plane relationship between film and substrate orientation, phi scans of the (110) diffraction were acquired on BFO films and perovskite-based substrates. Figure 4.8 shows the four BFO peaks separated by 90° from each other and well matched with the substrate peaks, revealing a cube-to-cube epitaxial growth of BFO on top of the (001)-oriented $LaAlO_3$ or $SrTiO_3$.
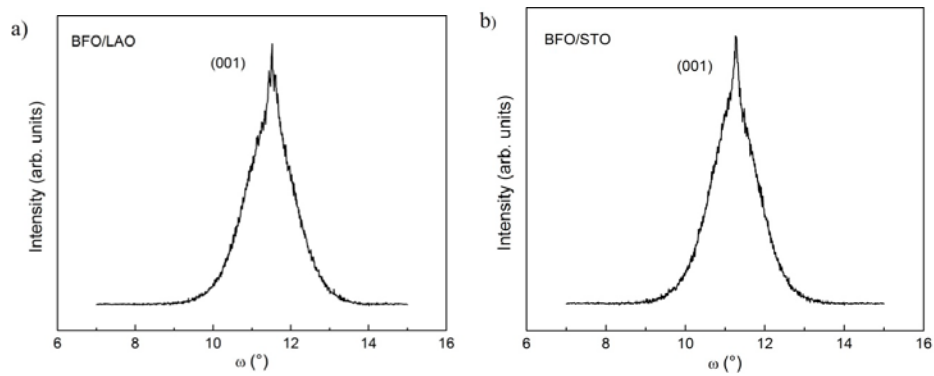
Figure 4.7: Rocking curves of $BiFeO_3$ (001) atomic plane on: a) (001) $LaAlO_3$ (FWHM=1.09°) and b) (001) $SrTiO_3$ (FWHM=1.12°).
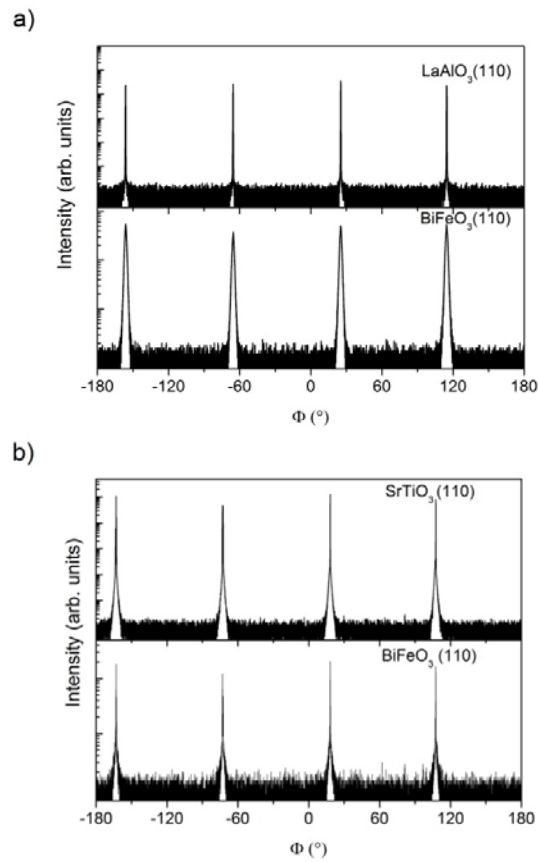
Figure 4.8: Phi scans of the (110) peak of BFO films annealed at 700°C on: a) (001) LaAlO₃ and b) (001) SrTiO₃ substrate.

In order to preferentially probe the top part of the films, Grazing Incidence (GI)-XRD was acquired on BFO films, Figure 4.9. The GIXRD scans were collected with a grazing incidence angle of 1.5°. The presence of different BiFeO₃ diffraction peaks on the pattern suggests some degree of polycrystalline growth in the films.
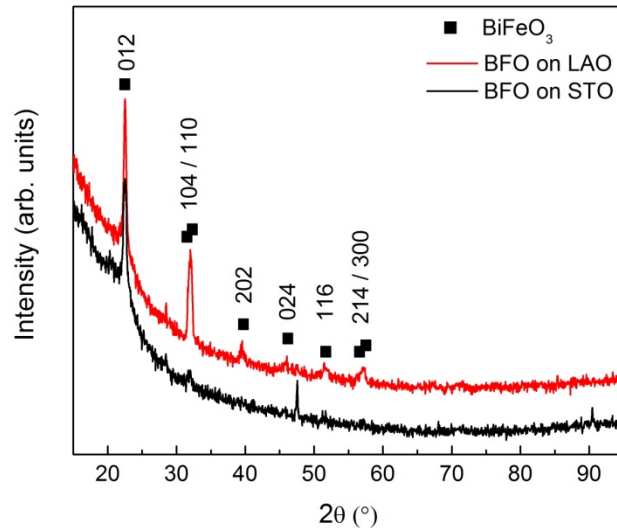
Figure 4.9: GI-XRD on BFO films annealed at 700°C on (001) LAO and (001) STO substrates.

SEM and AFM images in Figure 4.10 show similar surface microstructure of BFO films on LAO and STO substrates. While SEM micrographs show rather porous films, AFM images give more details about their morphology, revealing some square shaped porous (pore) as well as very small grains on the film surface. These grains can probably be ascribed to a polycrystalline bismuth ferrite which would be in accordance to XRD analyses. According to the theory of nucleation and growth of epitaxial thin films obtained by CSD, heterogeneous nucleation of film grains occurs at the interface between the substrate and the amorphous layer, as described by Miller et al. for the case of the cubic $Zr(Y)O_2$ on $Zr(Y)O_2$ [25]. The initial epitaxial grains simultaneously nucleate at different sites along the interface which is described in literature as the island-mode film growth. For this type of film growth, mosaicity in the film is often observed [26-28]. The grains continue the growth further through the film by consuming randomly oriented grains and converting polycrystalline film to a single crystal. The driving force is the elimination of grain boundaries [28, 29].
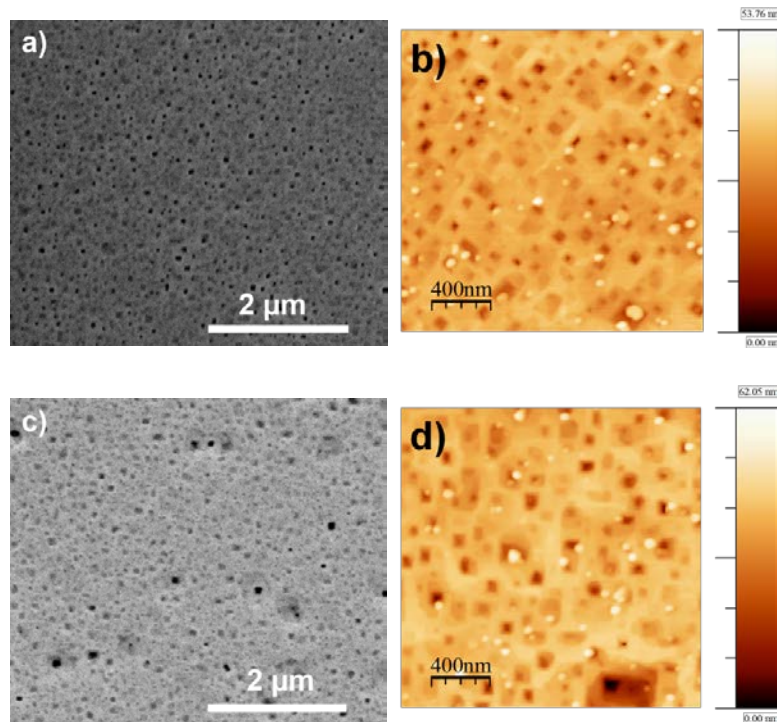
Figure 4.10: The surface SEM images (a, c) and AFM images (b, d) of BFO films on (001) LAO (a and b) and (001) STO (c and d) substrates.

4.3.2 (0001)-oriented sapphire

Besides perovskite based substrates, BiFeO₃ films were also deposited on (0001)-oriented sapphire (Al₂O₃). Although the *c*-sapphire has a hexagonal structure and significantly different lattice parameters (a=0.477 nm, c=1.304 nm) compared to BiFeO₃, this substrate is chosen because of its chemical and thermal stability. As XRD analysis shows, after annealing at 700°C, polycrystalline film consists of BiFeO₃ as a major phase accompanied by some impurity phases such as Bi₂Fe₄O₉ and Bi₂O₃ phases, Figure 4.11. SEM images reveal a discontinuous layer of grains with a size up to 1 μm, Figure 4.12. Some microstructural heterogeneity is present in the form of bigger, irregular shapes that probably belong to a secondary phase which is in accordance with XRD analysis.
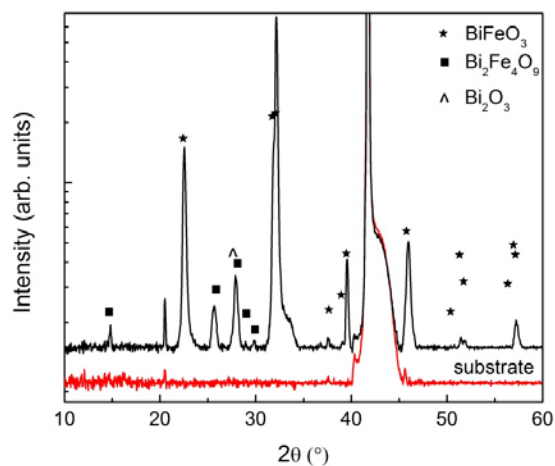
Figure 4.11: XRD pattern of $BiFeO_3$ film on *c*-sapphire substrate annealed at 700°C.

In comparison with the films on silicon-based or single crystal Al_2O_3 substrates, films on perovskite-based substrates consist of the bismuth ferrite phase while other secondary phases were not detected (or are under the detection limit). The plausible explanation is that the $BiFeO_3$ phase is epitaxially stabilized in the film as a result of the similarity in structure and compressive strain induced by the small lattice mismatch between $BiFeO_3$ and $SrTiO_3$ or $LaAlO_3$ substrates. This is supported by the fact that the film on *c*-sapphire does not show preferential orientation like on $SrTiO_3$ or $LaAlO_3$ which is also attributed to the lattice mismatch between the substrates and the film. On the other hand, compared to films grown on silicon based substrates and annealed at 700°C where a $BiFeO_3$ phase hardly exists or is accompanied by a large amount of secondary phases, films on sapphire contain less secondary phases and interaction with the substrate is not observed.
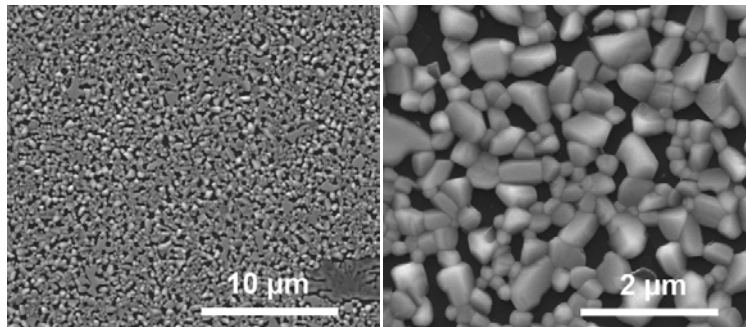
Figure 4.12: Surface SEM images of BiFeO$_3$ film annealed at 700°C on *c*-sapphire substrate.

4.3.3 Magnetic properties

To study the magnetic properties, BFO films deposited on (001) LaAlO$_3$ and (001) SrTiO$_3$ substrates were subjected to SQUID measurements at 2 K and 300 K with the magnetic field parallel to the film surface, Figure 4.13. This part of research is done in collaboration with Prof. Margriet Van Bael, Lab. voor Vaste-Stoffysica en Magnetisme and with Prof. Kristiaan Temst, Instituut voor Kern-en Stralingsfysica, KU Leuven. According to this magnetometry measurement, at 300 K BiFeO$_3$ films on both LaAlO$_3$ (Figure 4.13a) and SrTiO$_3$ (Figure 4.13b) show weak ferromagnetism and fully saturate below ~2 kOe with saturation magnetization values of ~3 emu/cm^3 and ~2.5 emu/cm^3, respectively. At 2 K however, while both samples still retain their ferromagnetic property, BiFeO$_3$ grown on LaAlO$_3$ needs a higher magnetic field (~20 kOe) to saturate.

The room-temperature magnetic properties presented here are consistent with the ones of single-phase films grown by other techniques such as PLD or MBE [30-32] as well as with theoretical predictions [33]. According to the theoretical study, the suppression of the spin spiral structure of the BiFeO$_3$ films results in weak ferromagnetic response due canting of antiferromagnetic lattice [33]. Breaking the spin spiral structure could result from the rotation of FeO6 octahedron surrounding the corresponding magnetic ions due the substrate induced strain in the epitaxial BiFeO$_3$ thin films [30, 34, 35]. Furthermore, these findings offer the possibility for further exploitation of the linear magnetoelectric

effect at room temperature since this effect in bulk BFO averages to zero due to the presence of cycloidal order [30].
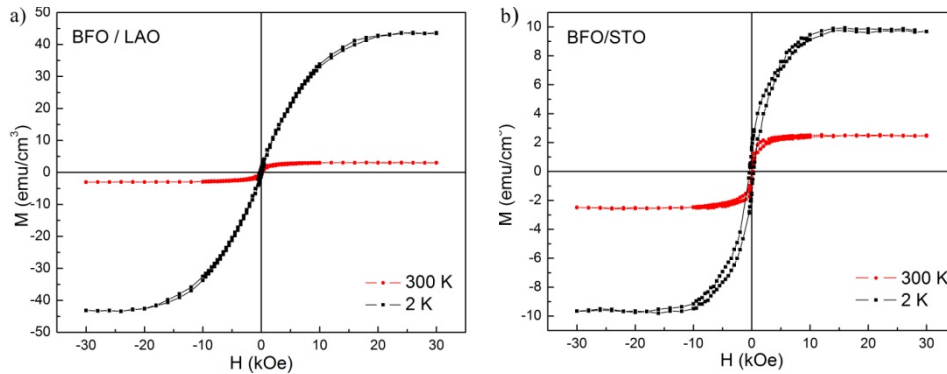
Figure 4.13: In-plane magnetization curves (*M-H*) measured at 2 K and 300 K for the $BiFeO_3$ films deposited on a) LAO and b) STO substrates. The presented magnetic measurements have been adjusted by subtracting the diamagnetic part of the signal originating from the substrates.

4.5 Films on buffer layers

Although the effect of perovskite-based substrates on the stabilization of $BiFeO_3$ phase was very promising, we also considered various buffer layers on silicon based substrates as an alternative to the rather expensive single crystal ones. Thus, we deposited TiO_2 as well as perovskite-based $BaTiO_3$ (BTO) and $SrTiO_3$ (STO) layers on platinized silicon substrates prior to the deposition of BFO film (Figure 4.14) in order to investigate the thermal behavior of bismuth ferrite films on buffer layers. After thermal treatment, all obtained buffer layers were single phase, polycrystalline films, Figure 4.15. In TiO_2 film anatase and rutile are present after annealing at 700°C. Reflections from $BaTiO_3$ and $SrTiO_3$ buffer layers correspond to perovskite structure. According to the XRD patterns in Figure 4.15, when BFO is deposited on TiO_2 buffer layers, the film contains a significant amount of pyrochlore $Bi_2Ti_2O_7$ phase. Obviously, the present secondary phase results from the interaction of the buffer layer and the BFO film. On the other hand, stability of the BFO phase is improved when deposited

over BaTiO$_3$ or SrTiO$_3$, Figure 4.15. Here, minor reflections of secondary phases (marked with +) present in the pattern point to much less pronounced film/buffer interaction compared with TiO$_2$.
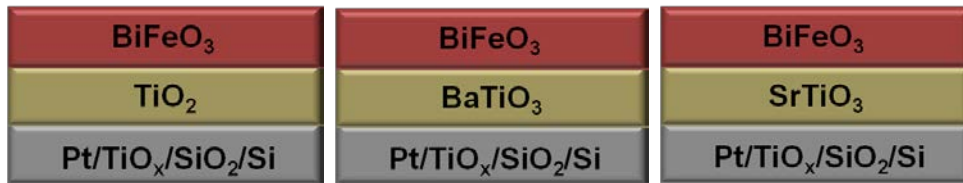
Figure 4.14: Schematic presentation of the BFO films deposited on different buffer layers on Pt/TiO$_x$/SiO$_2$/Si substrate
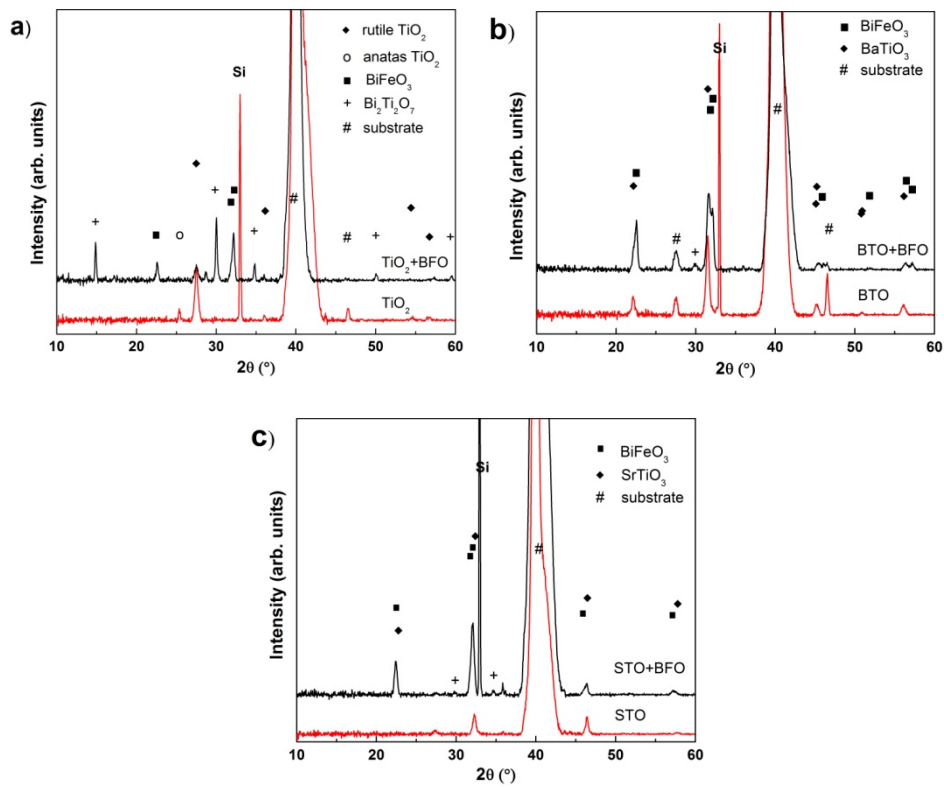
Figure 4.15: XRD patterns of BFO films on a) TiO$_2$, b) BaTiO$_3$ or c) SrTiO$_3$ buffer layer annealed at 700°C/1h.

SEM image in Figure 4.16 reveal rather inhomogeneous surface of the film deposited on TiO_2 and $SrTiO_3$ layer. On the other hand, Figure 4.16b indicates a narrow grain size distribution and reduced porosity in the BFO film on $BaTiO_3$.
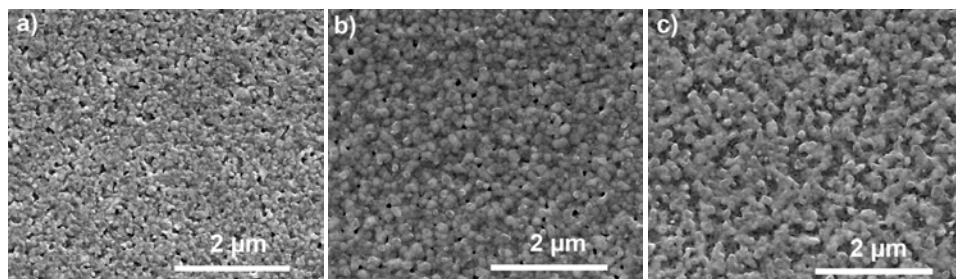
Figure 4.16: Surface SEM images of BFO films on a) TiO_2, b) $BaTiO_3$ or c) $SrTiO_3$ buffer layer annealed at 700°C/1h.

4.5 Conclusions

Our study on the substrate influence on the thermal stability of $BiFeO_3$ films showed that appropriate substrate selection plays an important role in preventing $BiFeO_3$ decomposition at elevated temperature. In the case of silicon based substrates, beside the decomposition, the appearance of iron- or bismuth-rich secondary phases can result from film-substrate interaction. On the other hand, perovskite based single crystal substrates promote epitaxial growth of $BiFeO_3$ films. Therefore, structural and dimensional similarities between film and substrate are crucial for epitaxial stabilization of the $BiFeO_3$ phase. Magnetic measurements on epitaxial BFO films at 2 K and 300 K showed weak ferromagnetic response. Another, more cost-effective solution for BFO film decomposition and interaction with the substrate is the use of proper polycrystalline buffer layers on silicon substrates. In this case chemical compatibility between buffer layer and bismuth ferrite should be taken into account. This approach can also be applicable in layered multiferroic composites when bismuth ferrite is one of the constituent phases.

4.6 Experimental

4.6.1 Solution synthesis and buffer layer deposition

TiO_2 buffer layer

The preparation of ~0.7 M citratoperoxo-Ti(IV) precursor solution already described in chapter 3 and subsequent deposition steps are adopted from the procedures developed in our research group [36, 37]. To form a buffer layer, the Ti(IV) precursor was spin coated at 3000 rpm for 30 s onto platinized silicon substrate and the deposited layer was thermally treated for 1 minute at 180°C, 2 minutes at 300°C and 1 hour at 600°C followed by annealing at 700°C for 1 hour in dry air atmosphere.

$BaTiO_3$ buffer layer

Preparation of multimetal ions solution with a total concentration of metal ions (Ba^{2+} and Ti^{4+}) of 0.6 M comprised of two steps. The first step was synthesis of aqueous citrato-Ti(IV) precursor according to the slightly modified procedure described previously. The solution was prepared without addition of hydrogen peroxide and NH_3, resulting in a colourless, transparent precursor with pH value of ~0.5. In the next step, $BaCO_3$ (p. a., Merck) was added in the appropriate volume of Ti(IV) precursor thus the molar ratio of Ba^{2+} to Ti^{4+} was 1:1 and mixed. While the $BaCO_3$ was already dissolving in the Ti(IV) precursor, 3 M solution of citric acid was added in 2:1 molar ratio to total amount of metal ions. When $BaCO_3$ was finally dissolved, ammonia was added dropwise to set the pH value at 7. A clear, colourless $BaTiO_3$ precursor was obtained by diluting with H_2O to desired the concentration. The $BaTiO_3$ precursor was applied on platinised silicon substrate by spin coating with 3000 rpm for 30 s. The obtained layer was treated on hot plates at 170°C/1 min, 250°C/2 min and 500°C/2 min and finally annealed at 700°C/1h in dry air.

$SrTiO_3$ buffer layer

The procedure for preparation of $SrTiO_3$ precursor and further buffer deposition was identical to the one described for $BaTiO_3$, except the fact that $SrCO_3$ (99,995%, Merck) was used instead of $BaCO_3$ in precursor preparation.

Prior to the deposition of the buffer layer, platinized silicon substrates were cleaned in SPM/APM (sulphuric acid peroxide mixture/ammonia peroxide mixture) mixture in order to improve wettability of the substrate surface for further deposition of aqueous precursor solutions.[38]

4.6.2 Chemical solution deposition of BiFeO₃ thin films

Aqueous $BiFeO_3$ precursor solution was prepared starting from aqueous Bi(III) and Fe (III) solutions as described in chapter 3. These monometal ion solutions were mixed in stoichiometric ratio and ammonia was added dropwise to adjust the pH value to 7.2. After diluting with water, the multimetal ion solution had a total concentration of metal ions of 0.6 M.

The prepared $BiFeO_3$ solution was spin coated on different types of substrates: i) silicon based substrates (SiO_2/Si, Al_2O_3/Si and Pt/TiO$_x$/SiO_2/Si) and ii) single crystal substrates (*c*-oriented sapphire Al_2O_3, (001)-oriented $SrTiO_3$ and $LaAlO_3$). Prior to deposition, the substrates were thoroughly cleaned in SPM/APM (sulfuric acid peroxide mixture/ ammonia peroxide mixture) to remove any organic contamination and improve their wettability. Furthermore, $BiFeO_3$ films were also deposited over buffered platinized silicon substrates (with TiO_2, $BaTiO_3$ or $SrTiO_3$ as buffer layers).

The general approach for deposition of the $BiFeO_3$ film was spin coating at a rotation speed of 3000 rpm during 30 s and an acceleration of 1000 rpm/s. The deposition process was slightly modified only when (001)-oriented $SrTiO_3$ and $LaAlO_3$ substrate were used. In this case it was necessary to increase the rotation speed to 6000 rpm to ensure uniform coating of a relatively small substrate surface (1 cm^2). In the next step the deposited layer was treated on hot plates at 110°C/1min, 260°C/2min and 480°C/2min in order to gradually decompose the organic constituents. This cycle of coating and hot plate treatment is repeated three times, thus enabling control of the film thickness. Finally, to anneal the films we inserted the samples in a preheated tube furnace at 600°C or 700°C for 1 hour in dry air atmospheres with a gas flow of 0.5 l/min.

4.6.3 Characterization techniques

The exact concentration of the metal ion in the monometal precursors was determined by means of inductively coupled plasma atomic emission spectroscopy (ICP–AES, Optima 3300 DV, PerkinElmer). Samples were prepared by diluting the precursor solutions with 5% HNO$_3$ (J.T. Baker, 69-70%, Baker Instra-analyzed Reagent) so that the expected concentrations fall within the calibration range of 1 to 10 ppm.

The crystal structure of the obtained films was analyzed using a Bruker D8 Discover diffractometer operating in θ–2θ mode with parallel beam geometry using a Göbel mirror (line focus, Cu K$_\alpha$ radiation). For thorough investigation of the epitaxialy grown BiFeO$_3$ films various X-ray diffraction measurements were carried out including (00l) rocking curves (Bruker D8 Discover diffractometer, UHasselt) as well as grazing incidence (GI) XRD and azimuthal phi scans (Bruker D8 Discover diffractometer with a CuK$_\alpha$ source mounted with a wide-angle Bragg-Brentano goniometer, KUL).

The microstructure of annealed films was analyzed using a scanning electron microscopy (FEI Quanta 200 FEG-SEM) equipped with secondary electron (SE) detectors. The topography analysis of the films on perovskite-based substrates was performed by means of the atomic force microscope (Veeco Dimension Microscope AFM with Digital Instrument Nanoscope III controller) in tapping mode using a Si cantilever tip.

Auger Electron Spectroscopy (AES) was carried out on films deposited on Al$_2$O$_3$/Si to determine the elemental composition of the film surface, while in-depth elemental composition was investigated using Rutherford backscattering spectroscopy (RBS). These analyses were performed in collaboration with prof. dr. K. Temst, Instituut voor Kern-en Stralingsfysica, KU Leuven. AES studies were performed in ultrahigh vacuum condition and reflected electrons were collected using a Thermo Alpha 110 hemispherical analyzer. On the other hand, RBS studies were performed after a ^{4}He$^+$ beam of 1.57 MeV generated from a 5SHD-2 Pelletron impinged on the samples mounted on a three-axis goniometer. The composition and thickness of the films were consequently obtained from the RBS spectra using the XRUMP software.

Magnetic response of the samples were measured by superconducting quantum interference device (SQUID) magnetometer of Quantum Design (MPMSXL-5) with a reciprocating sample option (RSO) head at 2K and 300K with the magnetic field in the plane of the thin films.

References

[1] O.Y. Gorbenko, S.V. Samoilenkov, I.E. Graboy, A.R. Kaul, Epitaxial stabilization of oxides in thin films, Chem. Mater., 14 (2002) 4026-4043.

[2] H. Bea, M. Bibes, S. Fusil, K. Bouzehouane, E. Jacquet, K. Rode, P. Bencok, A. Barthelemy, Investigation on the origin of the magnetic moment of BiFeO$_3$ thin films by advanced X-ray characterizations, Physical Review B, 74 (2006).

[3] N. Dix, R. Muralidharan, J.M. Rebled, S. Estrade, F. Peiro, M. Varela, J. Fontcuberta, F. Sanchez, Selectable Spontaneous Polarization Direction and Magnetic Anisotropy in BiFeO$_3$-CoFe$_2$O$_4$ Epitaxial Nanostructures, ACS Nano, 4 (2010) 4955-4961.

[4] N. Bassiri-Gharb, Y. Bastani, A. Bernal, Chemical solution growth of ferroelectric oxide thin films and nanostructures, Chem. Soc. Rev., 43 (2014) 2125-2140.

[5] G.L. Brennecka, J.F. Ihlefeld, J.P. Maria, B.A. Tuttle, P.G. Clem, Processing Technologies for High-Permittivity Thin Films in Capacitor Applications, J. Am. Ceram. Soc., 93 (2010) 3935-3954.

[6] R.W. Schwartz, Chemical solution deposition of perovskite thin films, Chem. Mater., 9 (1997) 2325-2340.

[7] I. Bretos, R. Jimenez, E. Rodriguez-Castellon, J. Garcia-Lopez, M.L. Calzada, Heterostructure and compositional depth profile of low-temperature processed lead titanate-based ferroelectric thin films prepared by photochemical solution deposition, Chem. Mater., 20 (2008) 1443-1450.

[8] M.L. Calzada, A. Gonzalez, J. Garcia-Lopez, R. Jimenez, Crystallization, heterostructure, microstructure, and properties of ferroelectric strontium bismuth tantalate films derived from tantalum glycolate solutions, Chem. Mater., 15 (2003) 4775-4783.

[9] M.L. Calzada, R. Jimenez, A. Gonzalez, J. Garcia-Lopez, D. Leinen, E. Rodriguez-Castellon, Interfacial phases and electrical characteristics of ferreoelectric strontium bismuth tantalate films on Pt/TiO$_2$ and Ti/Pt/Ti heterostructure electrodes, Chem. Mater., 17 (2005) 1441-1449.

[10] A.C. Dippel, T. Schneller, R. Waser, D. Park, J. Mayer, Formation Sequence of Lead Platinum Interfacial Phases in Chemical Solution Deposition Derived Pb(Zr$_{1-x}$Ti$_x$)O$_3$ Thin Films, Chem. Mater., 22 (2010) 6209-6211.

[11] C.T. Shelton, P.G. Kotula, G.L. Brennecka, P.G. Lam, K.E. Meyer, J.P. Maria, B.J. Gibbons, J.F. Ihlefeld, Chemically Homogeneous Complex Oxide Thin Films Via Improved Substrate Metallization, Adv. Funct. Mater., 22 (2012) 2295-2302.

[12] F. Tyholdt, H. Fjellvag, A.E. Gunnaes, A. Olsen, Synthesis of epitaxial BiFeO(3) films by chemical solution deposition on Pt(100), J. Appl. Phys., 102 (2007).

[13] B.E. Watts, F. Leccabue, S. Guerri, M. Severi, M. Fanciulli, S. Ferrari, G. Tallarida, C. Morandi, A comparison of Ti/Pt and TiN/Pt electrodes used with ferroelectric $SrBi_2Ta_2O_9$ films, Thin Solid Films, 406 (2002) 23-29.

[14] S. Yakovlev, J. Zekonyte, C.H. Solterbeck, M. Es-Souni, Interfacial effects on the electrical properties of multiferroic $BiFeO_3$/Pt/Si thin film heterostructures, Thin Solid Films, 493 (2005) 24-29.

[15] M. Valant, A.K. Axelsson, N. Alford, Peculiarities of a solid-state synthesis of multiferroic polycrystalline $BiFeO_3$, Chem. Mater., 19 (2007) 5431-5436.

[16] P.C. Dastoor, Auger Electron Spectroscopy and Microscopy - Techniques and Applications, in: D.J. O'Connor, B.A. Sexton, R.S.C. Smart (Eds.) Surface Analysis Methods in Materials Science, Springer, Germany, 2003.

[17] A. Huang, S.R. Shannigrahi, Effect of bottom electrode and resistive layer on the dielectric and ferroelectric properties of sol-gel derived $BiFeO_3$ thin films, J. Alloys Compd., 509 (2011) 2054-2059.

[18] T.M. Stawski, W.J.C. Vijselaar, O.F. Gobel, S.A. Veldhuis, B.F. Smith, D.H.A. Blank, J.E. ten Elshof, Influence of high temperature processing of sol-gel derived barium titanate thin films deposited on platinum and strontium ruthenate coated silicon wafers, Thin Solid Films, 520 (2012) 4394-4401.

[19] R.-Z. Xiao, Z.-D. Zhang, V.O. Pelenovich, Z.-S. Wang, R. Zhang, H. Li, Y. Liu, Z.-H. Huang, D.-J. Fu, Degradation of ferroelectric and weak ferromagnetic properties of BiFeO3 films due to the diffusion of silicon atoms, Chin. Phys. B, 23 (2014).

[20] S.M. Selbach, M.A. Einarsrud, T. Grande, On the Thermodynamic Stability of $BiFeO_3$, Chem. Mater., 21 (2009) 169-173.

[21] T. Rojac, A. Bencan, B. Malic, G. Tutuncu, J.L. Jones, J.E. Daniels, D. Damjanovic, $BiFeO_3$ Ceramics: Processing, Electrical, and Electromechanical Properties, J. Am. Ceram. Soc., 97 (2014) 1993-2011.

[22] J.D. Bucci, Robertso.Bk, W.J. James, Precision determination of lattice parameters and coefficients of thermal expansion of BiFeO$_3$, J. Appl. Crystallogr., 5 (1972) 187-&.

[23] J.M. Rondinelli, N.A. Spaldin, Structure and Properties of Functional Oxide Thin Films: Insights From Electronic-Structure Calculations, Adv. Mater., 23 (2011) 3363-3381.

[24] R.W. Schwartz, T. Schneller, R. Waser, Chemical solution deposition of electronic oxide films, C.R. Chim., 7 (2004) 433-461.

[25] K.T. Miller, C.J. Chan, M.G. Cain, F.F. Lange, Epitaxial zirconia thin-films from aqueous precursors, J. Mater. Res., 8 (1993) 169-177.

[26] T.A. Derouin, C.D.E. Lakeman, X.H. Wu, J.S. Speck, F.F. Lange, Effect of lattice mismatch on the epitaxy of sol-gel LiNbO$_3$ thin films, J. Mater. Res., 12 (1997) 1391-1400.

[27] C.D.E. Lakeman, Y. Xia, J.H. Kim, X.H. Wu, H.G. Eckert, F.F. Lange, Epitaxial films of Li$_{1-x}$Nb$_{1-x}$W$_x$O$_3$ prepared by chemical solution deposition, J. Mater. Res., 13 (1998) 1596-1606.

[28] F.F. Lange, Chemical solution routes to single-crystal thin films, Science, 273 (1996) 903-909.

[29] P.A. Langjahr, F.F. Lange, T. Wagner, M. Ruhle, Lattice mismatch accommodation in perovskite films on perovskite substrates, Acta Mater., 46 (1998) 773-785.

[30] H. Bea, M. Bibes, S. Petit, J. Kreisel, A. Barthelemy, Structural distortion and magnetism of BiFeO$_3$ epitaxial thin films: A Raman spectroscopy and neutron diffraction study, Philos. Mag. Lett., 87 (2007) 165-174.

[31] W. Eerenstein, F.D. Morrison, J. Dho, M.G. Blamire, J.F. Scott, N.D. Mathur, Comment on "Epitaxial BiFeO$_3$ multiferroic thin film heterostructures", Science, 307 (2005) 1203-1203.

[32] J.F. Ihlefeld, A. Kumar, V. Gopalan, D.G. Schlom, Y.B. Chen, X.Q. Pan, T. Heeg, J. Schubert, X. Ke, P. Schiffer, J. Orenstein, L.W. Martin, Y.H. Chu, R. Ramesh, Adsorption-controlled molecular-beam epitaxial growth of BiFeO$_3$, Appl. Phys. Lett., 91 (2007).

[33] C. Ederer, N.A. Spaldin, Weak ferromagnetism and magnetoelectric coupling in bismuth ferrite, Physical Review B, 71 (2005).

[34] F.M. Bai, J.L. Wang, M. Wuttig, J.F. Li, N.G. Wang, A.P. Pyatakov, A.K. Zvezdin, L.E. Cross, D. Viehland, Destruction of spin cycloid in (111)(c)-oriented $BiFeO_3$ thin films by epitiaxial constraint: Enhanced polarization and release of latent magnetization, Appl. Phys. Lett., 86 (2005).

[35] D.S. Rana, K. Takahashi, K.R. Mavani, I. Kawayama, H. Murakami, M. Tonouchi, T. Yanagida, H. Tanaka, T. Kawai, Thickness dependence of the structure and magnetization of $BiFeO_3$ thin films on $(LaAlO_3)_{(0.3)}(Sr_2AlTaO_6)_{(0.7)}$ (001) substrate, Physical Review B, 75 (2007).

[36] A. Hardy, J. D'Haen, M.K. Van Bael, J. Mullens, An aqueous solution-gel citratoperoxo-Ti(IV) precursor: synthesis, gelation, thermo-oxidative decomposition and oxide crystallization, J. Sol-Gel Sci. Technol., 44 (2007) 65-74.

[37] I. Truijen, M.K. Van Bael, H. Van den Rul, J. D'Haen, J. Mullens, Synthesis of thin dense titania films via an aqueous solution-gel method, J. Sol-Gel Sci. Technol., 41 (2007) 43-48.

[38] M.K. Van Bael, D. Nelis, A. Hardy, D. Mondelaers, K. Van Werde, J. D'Haen, G. Vanhoyland, H. Van den Rul, J. Mullens, L.C. Van Poucke, F. Frederix, D.J. Wouters, Aqueous chemical solution deposition of ferroelectric thin films, Integr. Ferroelectr., 45 (2002) 113-122.

Chapter 5

Self-assembled multiferroic nanostructured composites by ACSD

This chapter presents results on solution-derived composite films. Using the flexibility of solution chemistry and spontaneous phase separation of two immiscible phases, $BiFeO_3$-$CoFe_2O_4$ and $BaTiO_3$-$CoFe_2O_4$ films were synthesized on perovskite-based single crystal substrates. The composite films were subjected to thorough structural and microstructural characterization in order to understand the relation among the substrate and the constituent phases. Furthermore, the potential of the obtained composite heterostructures as multiferroic material was investigated through measurements of magnetic and electrical properties.

5.1 Introduction

Despite a lot of interest for magnetoelectric multiferroics and vast research that has been done in this field, proper materials with both ferroic orders and significant magnetoelectric coupling at room temperature still remain a challenge. Furthermore, the magnetoelectric coupling of the intrinsic multiferroics is usually too weak for practical applications. Combination of these factors brings about interest in different forms where, as an alternative to single phase multiferroics, composite materials comprising of ferroelectric and magnetic phases have received a lot of attention. Here, magnetoelectric coupling is a product of the interactions between ferroic orders of two constituent phases through interfacial strain, exchange-bias or field effects [1]. In strain-mediated multiferroics, where the interface mediates the elastic coupling, only very good

connectivity among constituent phases ensures better magnetoelectric coupling. In this context, three-dimensional epitaxial growth and self-assembly find their place in achieving more structural control at the nanoscale [2].

Self-assembled composite multiferroic heterostructures have been grown mostly by pulsed laser deposition [2-10] although there are some reports where rf magnetron sputtering [11], polymer-assisted deposition [12] or sol-gel deposition [13] was employed. In this work we investigate the potential of solution chemistry in the preparation of self-assembled multiferroic heterostructures. Aqueous chemical solution deposition enables a fast and flexible way to prepare materials with rather complex chemistry such as multiferroic composites which can consist of several different metal cations. Furthermore, the use of teratogenic substances such as 2-methoxyethanol and other organic solvents is minimized in favour of water based process. Therefore, we deposit two different composites $BiFeO_3$-$CoFe_2O_4$ and $BaTiO_3$-$CoFe_2O_4$ on single crystal substrates. Spinel ferrite $CoFe_2O_4$ (CFO) is chosen as a magnetic constituent in the composite because of its high ferrimagnetic order temperature (T_C=520°C), large magnetocrystalline anisotropy and magnetostriction and considerable saturation magnetization. The choice of perovskite $BaTiO_3$ (BTO) and $BiFeO_3$ (BFO) as ferroelectric constituents is based on their lead-free content and distinct ferroelectric properties. For deposition of multiferroic composites single crystal substrates $SrTiO_3$ (STO) and $LaAlO_3$ (LAO) with (001) orientation are selected considering the basal plane lattice constants of both substrates and constituent phases in the composite.

5.2 Solution preparation

Aqueous precursor solutions for deposition of $BiFeO_3$-$CoFe_2O_4$ and $BaTiO_3$-$CoFe_2O_4$ composites were prepared with a 7:3 molar ratio of perovskite phase (BTO or BFO) to spinel phase (CFO). The BFO-CFO precursor was obtained as a multimetal ion solution starting from monometal ion solutions of Bi, Fe and Co complexed with citric acid as a chelating agent. These solutions were mixed to achieve the desired composition of perovskite and spinel phase but also taking into account the stoichiometric ratio between the Bi^{3+} and Fe^{3+} ions in BFO as

well as between the Co^{2+} and Fe^{3+} ions in CFO. To prepare the BTO-CFO precursor, first a stoichiometric $BaTiO_3$ precursor was prepared by adding $BaCO_3$ and a 3 M solution of citric acid into a Ti precursor with low pH value, as described in chapter 4. The next step was to mix the $BaTiO_3$ precursor solution with Co(II) citrate and Fe(II) citrate solutions to achieve the desired composition. In the final precursor solutions of BFO-CFO and BTO-CFO composites, the total metal ion concentration was 0.6 M, the molar ratio of citric acid against metal ions was 2:1 and the pH value was adjusted to ~7.5 by addition of ammonia. With this synthesis approach we avoided the use of toxic methoxyethanol and ethylene glycol which were reported for other sol-gel derived composites [13]. Furthermore, solutions prepared in this way remained stable for almost one year at room temperature in air.

5.3 Gel decomposition

Prior to thin film deposition, thermal decomposition of the precursor gels was studied by thermo-gravimetric (TG) analysis from room temperature to 800°C in order to optimize the pyrolysis steps during film processing. To obtain gels, precursor solutions were first evaporated at 60°C. Figure 5.1 shows thermograms taken from ground gels of $BiFeO_3$-$CoFe_2O_4$ and $BaTiO_3$-$CoFe_2O_4$ precursors. Several steps in weight loss observed in TGA/DTG curves are associated with decomposition reactions in the gel. The decomposition process can be related to the general pathway reported in the earlier work of our group on citrate-based precursors [14-16]. In the first step, the decomposition of the excess ammonium citrate and uncomplexed functional groups of the citrato ligand occur around 200°C. In the case of BFO-CFO precursor, decomposition of monoethanolamin added to Bi^{3+} precursor also occurs during this step which can explain the difference in the profiles of these two precursors. This is followed by the decomposition of the complex itself and formation of organic residual fraction. The final decomposition steps associated with the removal of organic residual fraction occur at 435°C (for BFO-CFO precursor) and 420°C (BTO-CFO precursor), respectively. The stable weight is obtained starting from 480°C (BFO-CFO precursor) and 450°C (BTO-CFO precursor). The mass percentage

remaining after heating up to 800°C is 20 % for BFO-CFO and 19 % for BTO-CFO.
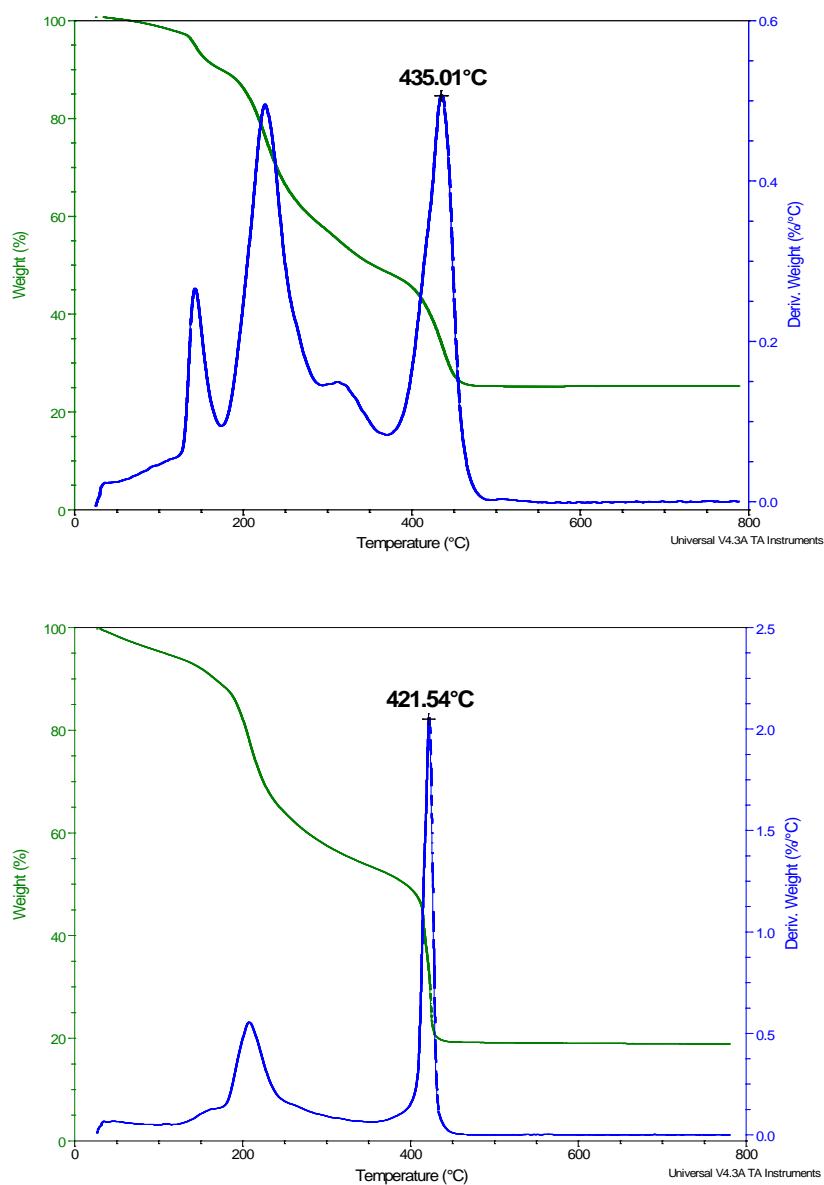

Figure 5.1: TGA/DTG profiles of the gels obtained from multimetal precursors of $BiFeO_3$-$CoFe_2O_4$ (top image) and $BaTiO_3$-$CoFe_2O_4$ (bottom image). The analysis is performed in dry air (100 ml/min) at the heating rate of 10°C/min.

Based on these results, a hot plate treatment comprising three steps (110°C, 260°C and 480°C) was chosen.

5.4 Powder crystallization

To confirm the potential of synthesized BFO-CFO and BTO-CFO precursors to form a two-phase system by spontaneous phase separation, HT-XRD was carried out. Precalcined gels were heated in static air at a heating rate of 10°C and diffraction patterns were recorded every 50°C starting from 450°C till 900°C. Diffraction patterns were also recorded at room temperature after the system had cooled down.

Crystallization of the perovskite $BiFeO_3$ phase from BFO-CFO precursor powder occurs at 550°C while the spinel CFO phase crystallizes at a higher temperature, above 600°C, see Figure 5.2a. XRD patterns confirm the phase separation during the crystallization of the powder precursor whereby the powder remains a two-phase system up to 750°C. At even higher temperatures, the peaks belonging to $BiFeO_3$ disappear due to the decomposition of the $BiFeO_3$ phase while the CFO phase remains present in the powder.

In the case of the BTO-CFO precursor powder, crystallization of both phases is shifted to higher temperatures as the patterns in Figure 5.2b indicate. First indications of crystalline $BaTiO_3$ phase appear above 750°C. On the other hand, peaks associated with spinel $CoFe_2O_4$ are present only in the pattern recorded after cooling to room temperature. No $BaCO_3$ formation was observed within detection limit of the technique.

Therefore, based on the results presented here it can be concluded that both synthesized aqueous precursors allow crystallization and coexistence of perovskite and spinel phase in a composite form. However, the difference in the required crystallization temperatures to obtain a two-phase system is around 150°C. Possible implications of this temperature difference for the microstructure of the thin films will be further discussed in this chapter.
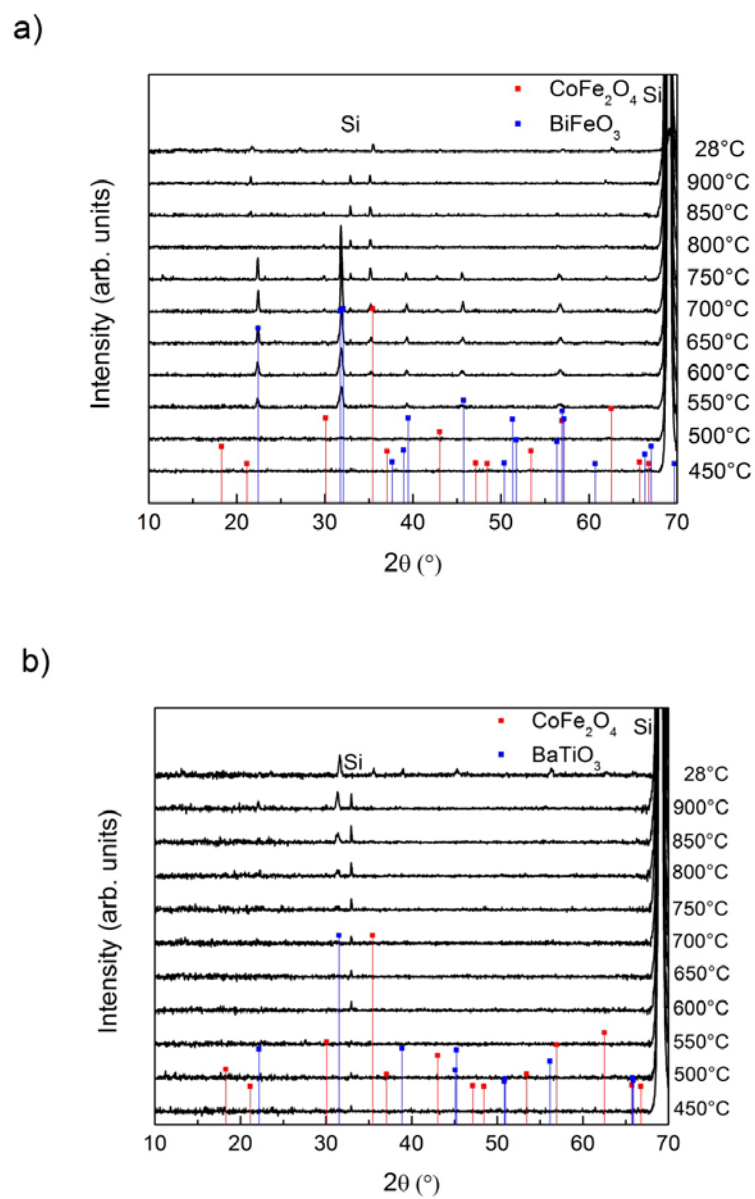
a)

b)

Figure 5.2: HT-XRD patterns of a) $BiFeO_3$-$CoFe_2O_4$ and b) $BaTiO_3$-$CoFe_2O_4$ gels pre-annealed at 200°C for 1hour.

5. 5 BiFeO$_3$-CoFe$_2$O$_4$ thin film composites

5.5.1 Phase formation

The BiFeO$_3$-CoFe$_2$O$_4$ film deposited on (001) LAO and (001) STO substrates were annealed at 700°C for 1 hour whereby the choice of annealing temperature was based on the studies on thermal stability of BiFeO$_3$ phase presented in chapter 4. The resulting phase formation was investigated by means of XRD. Figure 5.3 shows diffraction patterns of the composite on both substrates in which reflections associated with the BiFeO$_3$ phase follow the substrate, pointing to highly textured bismuth ferrite films. In case of the composite on LAO substrate, besides the peaks from rhombohedral BFO phase (R-BFO), reflections belonging to metastable near-tetragonal phase (T-BFO) are present in the pattern. On the basis of angle position of (002) peaks, out-of-plane lattice parameters for R-BFO and T-BFO were estimated to be $c = 0.397$ nm and $c = 0.464$ nm, respectively. Contrary to this pattern, XRD of a single phase BFO film on (001) LAO in Figure 4.6 (Chapter 4), shows no reflections pointing to the presence of T-BFO in the film. According to Zeches et al., T- and R-BFO phases coexist in single films on (001)-oriented LAO substrate due to epitaxial strain induced by the substrate [17]. They also found that the fraction of R-phase increases with film thickness [17]. Thus, the thickness difference could be one of the reasons for the absence of T-BFO in single phase BFO films on LAO since in this case the film thickness is around 100 nm, while in the composite BFO film the thickness is only around 40 nm as shown later by TEM studies. Another explanation, according to Dix et al. [18], could be that in composite nanostructures the extra interface between the two phases plays a role. They found the vertical interface between T-BFO and CoFe$_2$O$_4$ to be semicoherent despite the significant lattice mismatch [3], and therefore these interfaces probably promote stabilization of the T-BFO [18]. On the other hand, surprisingly, reflections belonging to the CoFe$_2$O$_4$ phase are not visible in the XRD pattern in Figure 5.3 although after annealing the composite at 700°C formation of a CoFe$_2$O$_4$ phase is expected. The absence of CFO peaks does not necessarily mean that CoFe$_2$O$_4$ is not present as a crystalline phase in the system. The explanation can be that CFO grains are too small to be detected or that the grain growth occurrs in such a way that they do not follow (001)

orientation. Thus, further microstructural analyses are necessary to shed some light on this question.
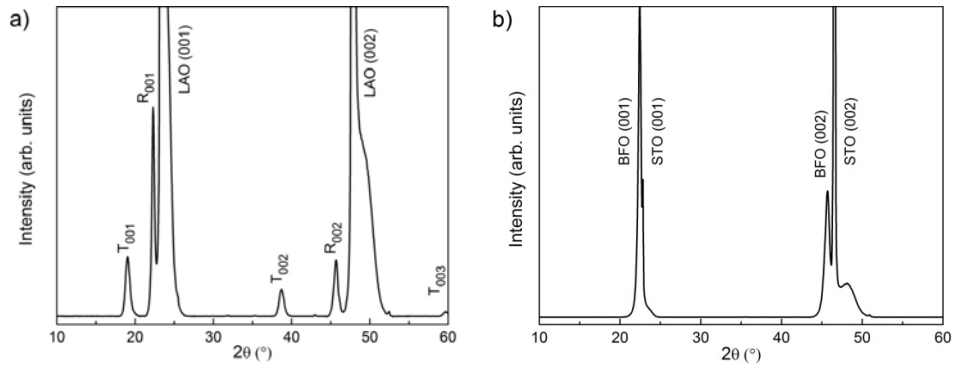
Figure 5.3: XRD patterns of BFO-CFO composite on a) (001) LAO substrate where T in tetragonal-like phase and R is rhombohedral-like phase of $BiFeO_3$ and b) (001) STO substrate.

5.5.2 SEM and AFM results

Microstructure and morphology of the BFO-CFO composite film on LAO and STO substrates were investigated by SEM and AFM techniques and the results are presented in Figure 5.4 and 5.5, respectively. In these SEM and AFM images formation of the two phase system with matrix and embedded phase is not so obvious although a few outgrowths are visible in the AFM image. They further affect the film surface roughness resulting in the root-mean-square (rms) roughness of about 5 nm and 8 nm for the composite on LAO and STO substrate, respectively.
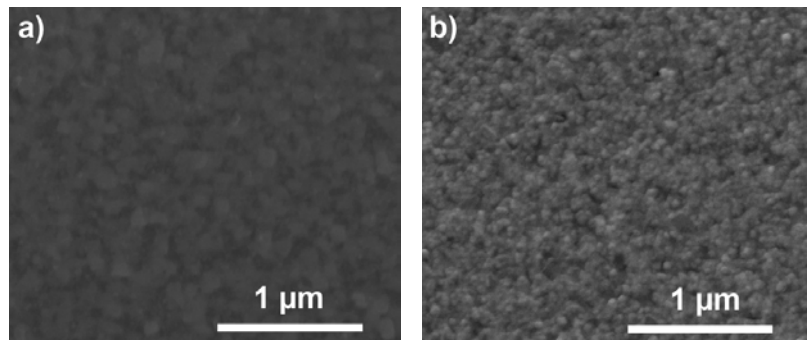
Figure 5.4: SEM images of BFO-CFO composite deposited on (001) LaAlO$_3$ (left) or (001) SrTiO$_3$ (right) substrate.
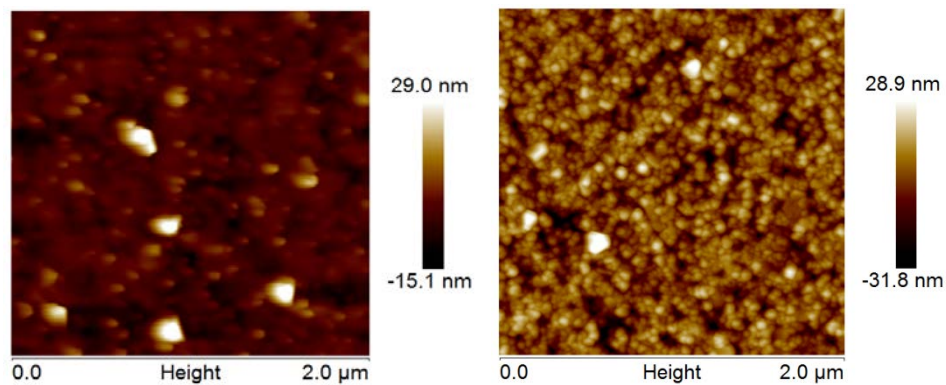
Figure 5.5: AFM images of BFO-CFO composite deposited on (001) LaAlO$_3$ (left) or (001) SrTiO$_3$ (right) substrate.

According to the SEM and AFM results, it seems that CoFe$_2$O$_4$ phase exist in BFO matrix as randomly dispersed nanoparticles instead of nanopillars clearly separated in the matrix. Similarly, Liu et al. [13] reported on nanoparticulate morphology in the sol-gel derived BaTiO$_3$-CoFe$_2$O$_4$ composite films. Furthermore, NiFe$_2$O$_4$ nanoparticles are formed in BaTiO$_3$-NiFe$_2$O$_4$ films obtained by polymer assisted deposition (PAD) [12] as well as in Pb(Zr$_{0.52}$Ti$_{0.48}$)O$_3$-NiFe$_2$O$_4$ films grown by PLD [19].

127

5.6 BaTiO$_3$-CoFe$_2$O$_4$ thin film composites

5.6.1 Phase formation

The annealing temperature of 900°C for the BaTiO$_3$-CoFe$_2$O$_4$ composite films was selected taking into consideration: 1. The reports on the BaTiO$_3$ films emphasizing the importance of annealing at temperatures not lower than 900°C since improved microstructural and crystalline quality was obtained at such temperatures leading to significant enhancements in electrical properties [20, 21]; 2. The studies of Liu et al. [13] on sol-gel derived BaTiO$_3$-CoFe$_2$O$_4$ composite films annealed at 1000°C and Luo et al. [12] on BaTiO$_3$-NiFe$_2$O$_4$ composite obtained by PAD after annealing at 900°C; 3. HT-XRD results obtained on the BaTiO$_3$-CoFe$_2$O$_4$ powder. BaTiO$_3$-CoFe2O4 composites deposited on (001) LAO and (001) STO substrates after annealing at 900°C were subjected to XRD measurements and the resulting patterns are shown in Figure 5.6. The most intense peaks in the patterns correspond to the (001) and (002) reflections of LAO and STO substrates. Furthermore, XRD analysis points to the reflections from two different phases present in the obtained films, namely BaTiO$_3$ and CoFe$_2$O$_4$. These results confirm the spontaneous phase separation occurring in the films during crystallization leading to the development of separate perovskite and spinel phases. Both phases show a high degree of crystallographic orientation with their *c*-axis normal to the substrates. Based on the (002) and (004) peak positions, out-of-plane lattice parameters are estimated for BTO and CFO, respectively. Thus, in BTO-CFO composite on LAO substrate the lattice parameters were found to be *c* = 0.402 nm for BTO and *c* = 0.828 nm for CFO. In the case of the composite on the STO substrate, out-of-plane lattice parameters are estimated to be *c* = 0.403 nm and *c* = 0.829 for BTO and CFO crystals, respectively. In comparison with the out-of-plane lattice parameters of bulk tetragonal BTO (*c* = 0.4036 nm) and cubic CFO (*a* = 0.838 nm), the calculated values indicate a very small out-of-plane compressive strain of 0.3% and 0.1% for the BTO constituent on LAO and STO substrate, respectively indicating almost relaxed (001)BTO crystals. This film relaxation probably results from dislocations whose formation is favourable at higher temperatures. On the other hand, when compared to bulk cubic CFO (*a* = 0.838 nm), the CFO phase has larger compressive out-of-plane strains of 1.2% on LAO

and 1.1% on STO substrate although the tensile strain would be expected considering the in-plane compressive strain due to the smaller lattice parameters from both the LAO (a = 0.379 nm) or the STO (a = 0.3905 nm) substrate. The appearance of compressive strain instead of tensile that is being expected in these composites suggests that the resulting strain could be due to the influence of the BTO matrix instead of the substrate [11, 22].
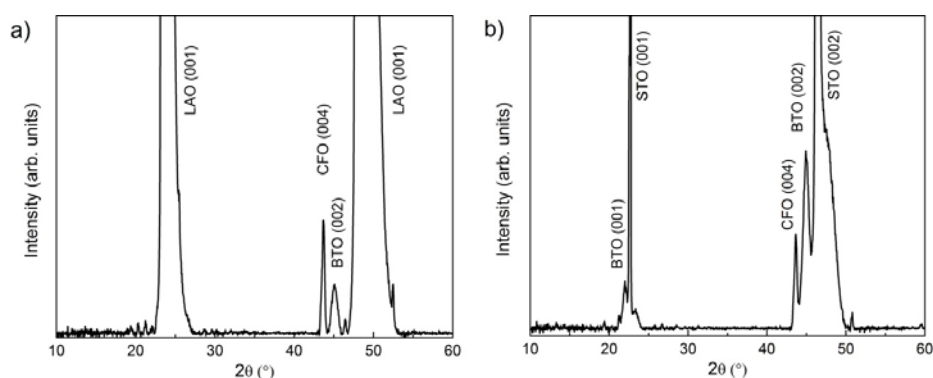
Figure 5.6: XRD patterns of the BTO-CFO film composite on a) (001) LAO and b) (001) STO substrate.

5.6.2 SEM and AFM results

$BaTiO_3$-$CoFe_2O_4$ composite films were investigated using SEM and AFM techniques to study their microstructure and morphology. SEM micrographs in Figure 5.7 show a very heterogeneous microstructure where it is possible to distinguish a matrix phase and grains embedded in the matrix. The embedded phase consists of bigger grains with a shape resembling irregular pyramids that grow out of the matrix phase, as the AFM images in Figure 5.8 show. The size of these grains is not uniform and they can reach up to 300 nm in width. Contrary, the matrix grains are equiaxed and considerably smaller than the embedded grains. In both cases, grain morphology is not affected by the choice of substrate. Both films were very rough with a root mean square (RMS) roughness of about 14 nm and 12 nm when deposited on (001) LAO and (001) STO substrate, respectively. The microstructure of the obtained films is in agreement

129

with the XRD results that reveal that the films are separated into two different phases.
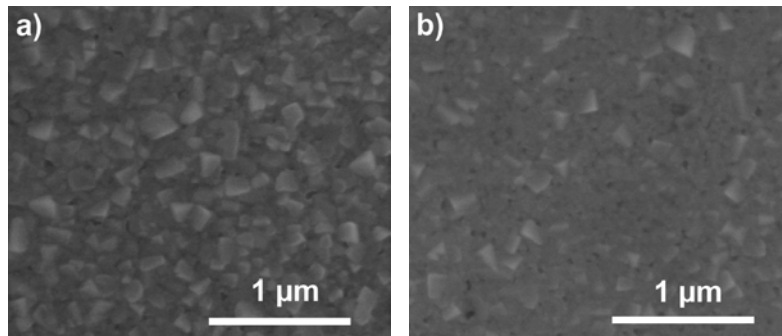
Figure 5.7: SEM images of $BaTiO_3$-$CoFe_2O_4$ film deposited on a) (001) $LaAlO_3$ or b) (001) $SrTiO_3$ substrate.
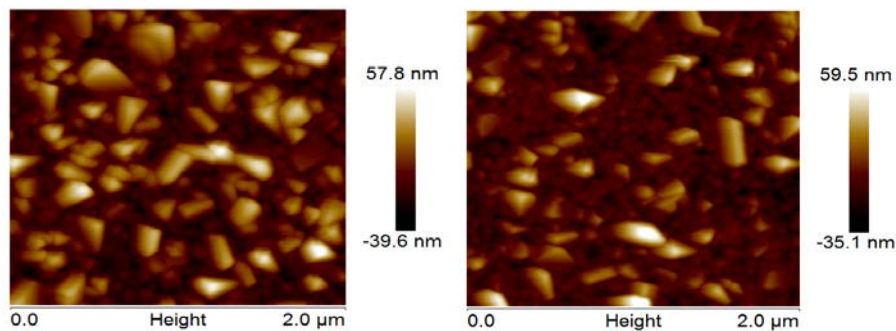
Figure 5.8: AFM images of $BaTiO_3$-$CoFe_2O_4$ film deposited on (001) $LaAlO_3$ (left) or (001) $SrTiO_3$ (right) substrate.

The amount and size of the outgrowths are much larger than in the BFO-CFO system. This also affects the surface roughness, resulting in a smoother surface of BFO-CFO films in comparison with BTO-CFO films and a decrease of rms roughness to about 5-8 nm. The difference in annealing temperature (200°C) between BFO-CFO and BTO-CFO composites could be an explanation for the observed difference in the size of these embedded features. However, due to the limitations imposed by the phase formation and decomposition of BFO at higher

temperatures as discussed in Chapters 3 and 4 it was not possible to anneal $BiFeO_3$-$CoFe_2O_4$ composite at higher temperature like $BaTiO_3$-$CoFe_2O_4$ composite. A relation between the growth temperature and the size of $CoFe_2O_4$ features was observed during PLD processing where an increase in temperature induced larger-sized $CoFe_2O_4$ nanopillars in both $BiFeO_3$-$CoFe_2O_4$ and $BaTiO_3$-$CoFe_2O_4$ composites [4, 23].

5.7 TEM study of BFO-CFO and BTO-CFO composite nanostructures

In order to get insight into the interfaces and interaction between the constituent phases in BFO-CFO or BTO-CFO composites as well as their relationship with the (001) LAO substrate, cross-sectional high-resolution transmission electron microscopy (HR-TEM), scanning transmission electron microscopy (STEM) and energy dispersive X-ray spectroscopy (EDX) were performed. This part of the research is done in collaboration with prof. dr. Joke Hadermann and the EMAT group, University of Antwerp.

$BiFeO_3$-$CoFe_2O_4$ composite on (001)$LaAlO_3$ substrate
Detailed structural analysis is performed on the cross section of $BiFeO_3$-$CoFe_2O_4$ composite deposited onto (001) LAO substrate. A selected area electron diffraction (SAED) pattern in Figure 5.9 reveals an epitaxial relation between the $BiFeO_3$ film and the LAO substrate. The $LaAlO_3$ and $BiFeO_3$ phases are oriented in the [100] zone axis, in contrast to the phase $CoFe_2O_4$ which is oriented in the [112] zone axis. The HRTEM image of the BFO-LAO interface in Figure 5.9b shows that the growth direction of the $BiFeO_3$ film follows the direction of the substrate which is further confirmed by Fast Fourier Transform (FFT) images.
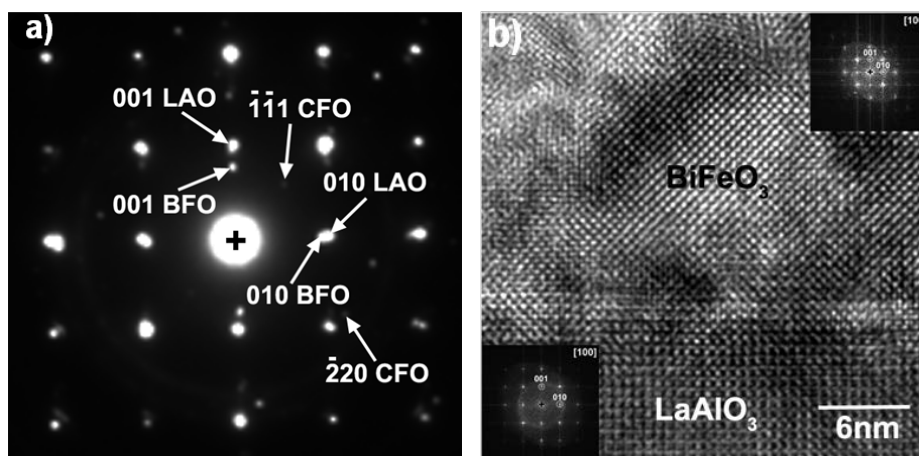
Figure 5.9: a) SAED pattern of a cross section of $BiFeO_3$-$CoFe_2O_4$ composite on $LaAlO_3$. The substrate ($LaAlO_3$) and the perovskite phases ($BiFeO_3$) are indexed in zone axis [100] while spinel phase ($CoFe_2O_4$) is indexed in [112] zone axis. b) HRTEM image of a cross section of the film with FFT images of the phases shown as insets.

Figure 5.10a shows a cross sectional STEM image of the $BiFeO_3$-$CoFe_2O_4$ composite on an LAO substrate. A film with a thickness of around 40 nm consists of a $BiFeO_3$ matrix with embedded $CoFe_2O_4$ grains pointing to phase separation of two immiscible phases. The surface of the $BiFeO_3$-$CoFe_2O_4$ film is rather smooth and the $BiFeO_3$ matrix is continuous. Spinel $CoFe_2O_4$ grains grow on the perovskite phase and the grain growth continues through the matrix of BFO film. This observation as well as epitaxial relationship between the BFO film and the substrate is further confirmed by high resolution HAAD-STEM images of two different areas along the BFO-CFO film cross section in Figure 5.10b and 5.10c. In addition, Figure 5.10b confirms the coexistence of T-phase and R-phase in the $BiFeO_3$ film where the areas of each phase were distinguished based on the difference in lattice parameters. Thus, for a T-phase area, the *c* axis lattice parameter was estimated to ~0.47 nm while for an R-phase area the out-of-plane lattice parameter was ~0.40 nm. These values are in agreement with the lattice parameters calculated from the corresponding reflections in the XRD patterns in Figure 5.3 and with values reported in literature [17].
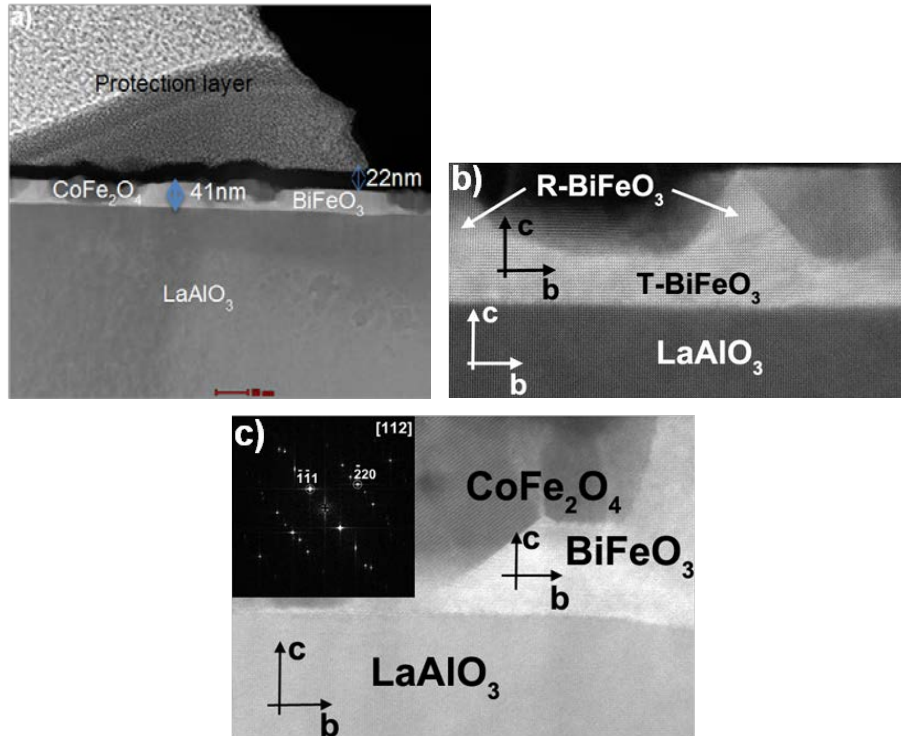
Figure 5.10: a) Cross-sectional STEM image of $LaAlO_3/BiFeO_3/CoFe_2O_4$ film coated by an amorphous carbon layer with thickness of 22 nm and Pt nanoparticles resulting from protection layers during FIB preparation; b) and c) High resolution HAADF-STEM images of two different areas in the interface region in a). The inset in c) is the FFT pattern of the $CoFe_2O_4$ area.

Figure 5.11a shows a cross-sectional high resolution HAADF-STEM image of the interface between the $BiFeO_3$ and $CoFe_2O_4$ phases in the composite film. Analysis of the interface from the inverse FFT image in Figure 5.11b indicates presence of misfit dislocations in Figure 5.11c. The lattice distortions of $BiFeO_3$ and $CoFe_2O_4$ result from misalignment of the unit cells within the crystals. The separations between two closer misfit dislocations are 1.35 nm.
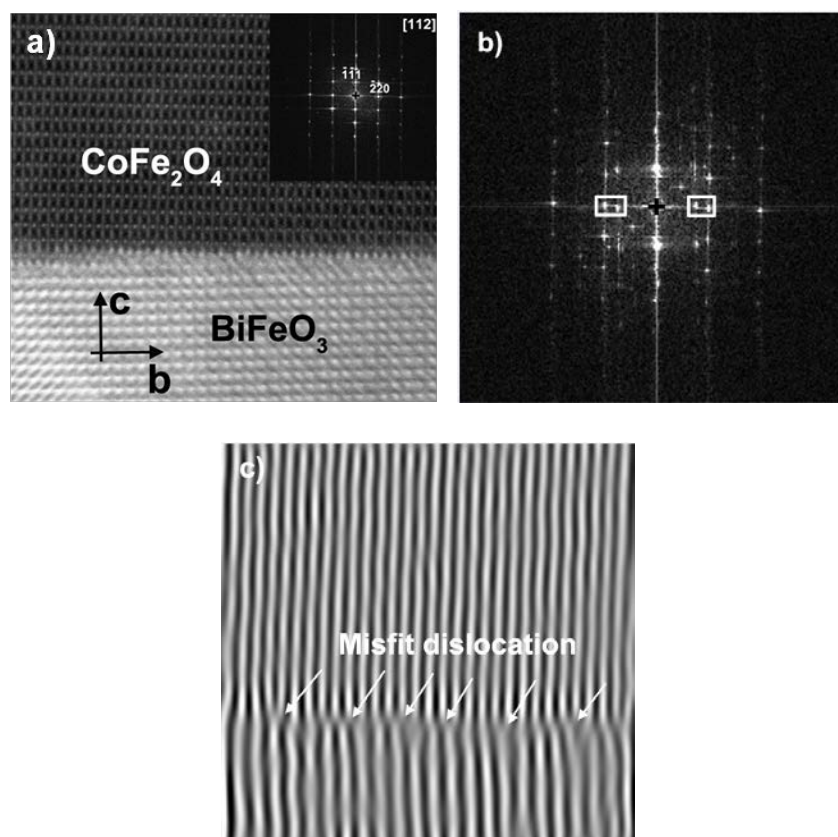
Figure 5.11: a) Cross-sectional high resolution HAADF-STEM image of the interface between $BiFeO_3$ and $CoFe_2O_4$ in BFO-CFO composite; b) Fourier transform (diffractogram) of the image a); c) Inverse Fourier transform of the reflections indicated by white square in b) revealing the presence of misfit dislocations.

In order to investigate the presence of secondary phases or interactions among the compounds in BFO-CFO heterostructures including the LAO substrate, EDX elemental mapping was performed. The results in Figure 5.12 point to the presence of the different elements expected in this film. There is no evidence of formation of secondary phases or interdiffusion across interfaces of constituent phases or any intermixing with the substrate.
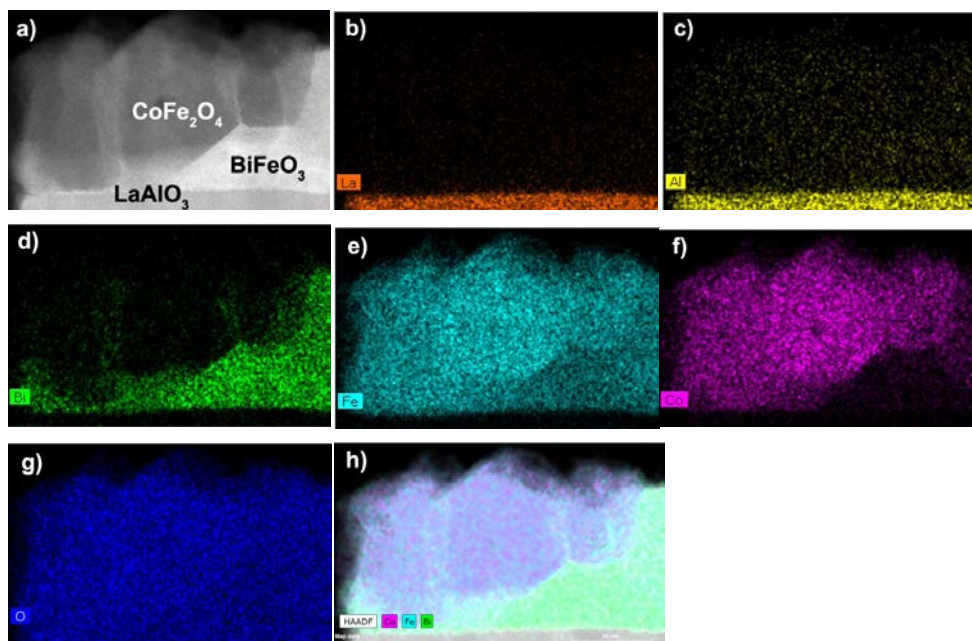
Figure 5.12: a) High resolution HAADF-STEM image of the cross section of the LaAlO$_3$//BiFeO$_3$/CoFe$_2$O$_4$ film and corresponding EDX mapping of the individual elements: b) La, c) Al, d) Bi, e) Fe, f) Co, g) O and h) Bi-Fe-Co.

BaTiO$_3$-CoFe$_2$O$_4$ composite on (001)LaAlO$_3$ substrate

Figure 5.13a shows selected-area electron diffraction pattern (SAED) of the BTO-CFO composite films on LAO substrate, where both the substrate (LaAlO$_3$) and the perovskite phases (BaTiO$_3$) are indexed in [100] zone axis. The SAED pattern reveals a heteroepitaxial growth of BTO on the LAO substrate, which is further confirmed by a HRTEM image in Figure 5.13b as well as by the corresponding FFT images from BTO and LAO shown as an insert. The orientation relationship of the BTO phase and the substrate is determined to be (001)LaAlO$_3$||(001)BaTiO$_3$ assuming the crystal structure of all of them as (pseudo)cubic.
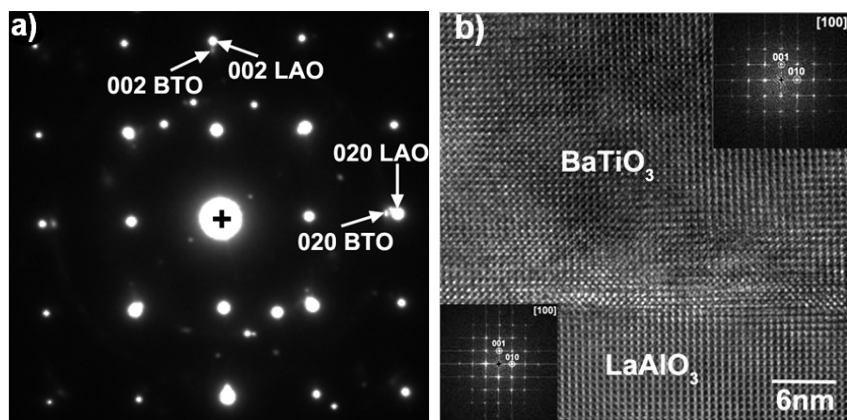
Figure 5.13: a) SAED pattern obtained at a cross section of $LaAlO_3//BaTiO_3/CoFe_2O_4$. Indexation is in zone axis [100]. b) HRTEM image of a cross section of the same sample. Fourier transform of the image (diffractogram) are shown as insets. All the indexations were done using the perovskite subcell that is common to all three phases.

Figure 5.14a is a cross sectional STEM image of a $BaTiO_3$-$CoFe_2O_4$ film on $LaAlO_3$ substrate. The film with a thickness of around 87 nm is rather inhomogeneous and has considerable surface roughness. Two self-assembled phases, perovskite $BaTiO_3$ and spinel $CoFe_2O_4$ are clearly seen with $CoFe_2O_4$ grains embedded in a matrix consisting of $BaTiO_3$ phase. The rather rough $BaTiO_3$ film comprises different grains with visible grain boundaries. This image also reveals that growth of the CFO phase occurs on the $BaTiO_3$ phase instead of on the LAO substrate. Protruding through the BTO matrix, CFO grains form islands on the top of the film. Thus, the outgrowths in the film observed in SEM and AFM images are in agreement with $CoFe_2O_4$ grains visible in the cross-section STEM image. Figures 5.14b and 5.14c show cross-sectional high resolution HAADF-STEM images of the enlarged area at the BTO-CFO-LAO interfaces as well as the FFT pattern of the $CoFe_2O_4$ area as an inset. These results further evidence the growth of CFO on BTO grains as well as the spread of the CFO phase in $BaTiO_3$ matrix whereby the $CoFe_2O_4$ is oriented in the [112] zone axis.
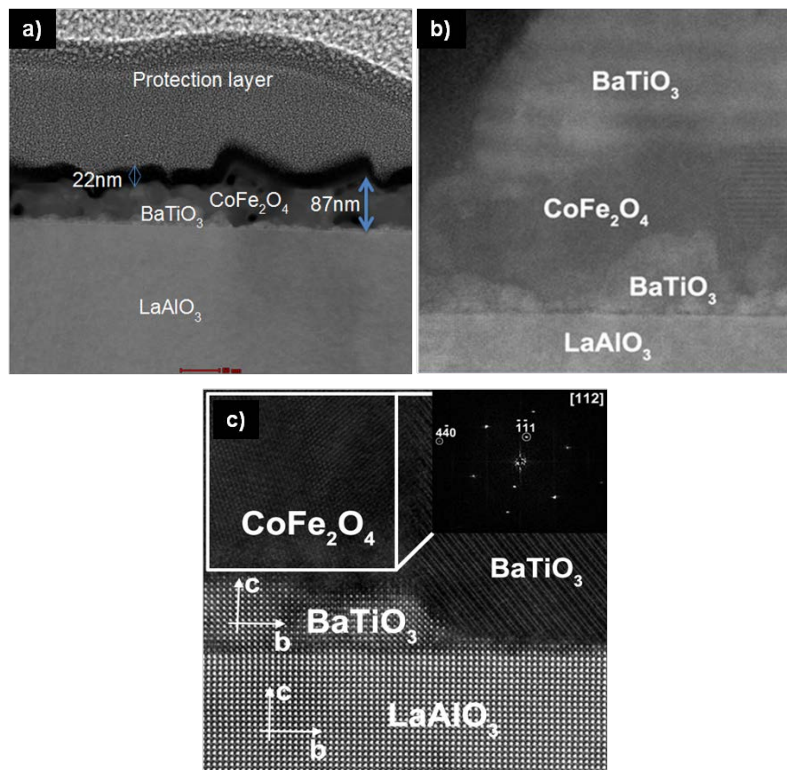
Figure 5.14: a) Cross-sectional STEM image of $LaAlO_3/BaTiO_3/CoFe_2O_4$ film coated by an amorphous carbon layer with a thickness of 22 nm and Pt nanoparticles as protection layers during FIB preparation; b) and c) High resolution HAADF-STEM image of interface region in a). The inset is the FFT pattern of the $CoFe_2O_4$ area.

Further investigation on this sample of BTO-CFO composite is focused on the interface between the $BaTiO_3$ film and the $LaAlO_3$ substrate for which cross-sectional HAADF-STEM and corresponding FFT images are presented in Figures 5.15a and 5.15b, respectively. By applying inverse FFT on the reflections marked by the white squares in image 5.15b, Figure 5.15c is obtained revealing the presence of misfit dislocations in the interface, spaced 5.94 nm apart. The interface is semicoherent with extra atomic planes in LAO interface with $BaTiO_3$ film. Formation of such misfit dislocations results from the considerable lattice mismatch between BTO and LAO. Thus, the growth of a relaxed film without substrate induced strain is expected.
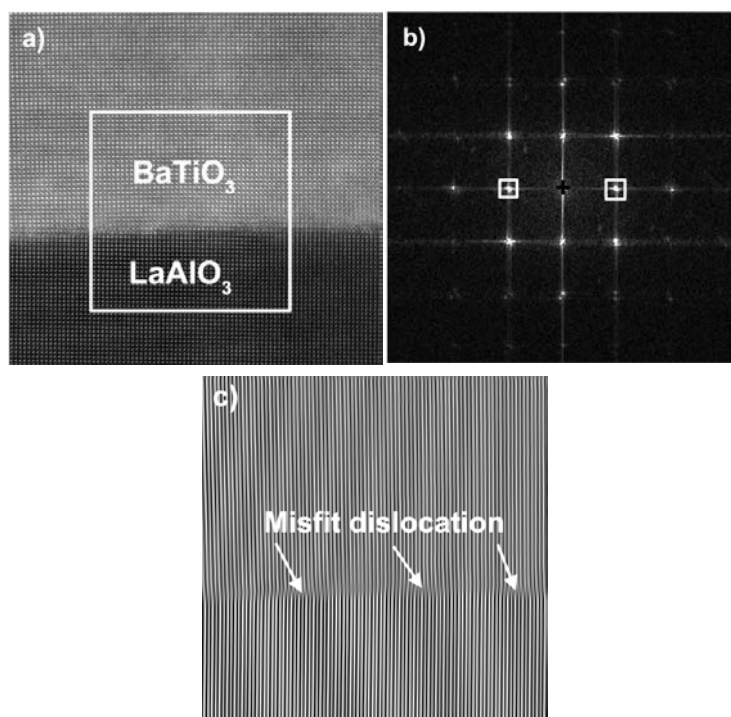
Figure 5.15: a) Cross-sectional high resolution HAADF-STEM image of the interface between $LaAlO_3$ substrate and $BaTiO_3$ film in the BTO-CFO composite; b) Fourier transform (diffractogram) of the image a); c) Inverse Fourier transform of the reflections indicated by white square in b) revealing the presence of misfit dislocations.

In figure 5.16a a high resolution HAADF-STEM image of the cross section of the $LaAlO_3/BaTiO_3/CoFe_2O_4$ film reveals an area in the film that cannot be assigned to $BaTiO_3$ nor $CoFe_2O_4$. In addition, corresponding EDX elemental mapping (Figures 5.16a-i) and the spectrum (Figure 5.16j) point to Ba, Ti, Fe and O as elements involved in this area. It was possible to index Fourier transforms of the unknown phase in zone axis [0-10] in Figure 5.17b using $Ba_2Ti_4Fe_2O_{13}$ cell parameters (a=15.196, b=3.8975, c=9.1291) [24]. Furthermore, the inset in Figure 5.17 represents a simulated STEM image of $Ba_2Ti_4Fe_2O_{13}$, which is in agreement with the experimental one. Formation of $Ba_2Ti_4Fe_2O_{13}$ as an impurity phase in BTO-CFO composite probably results from interdiffusion occurring across the interface during annealing at 900°C.
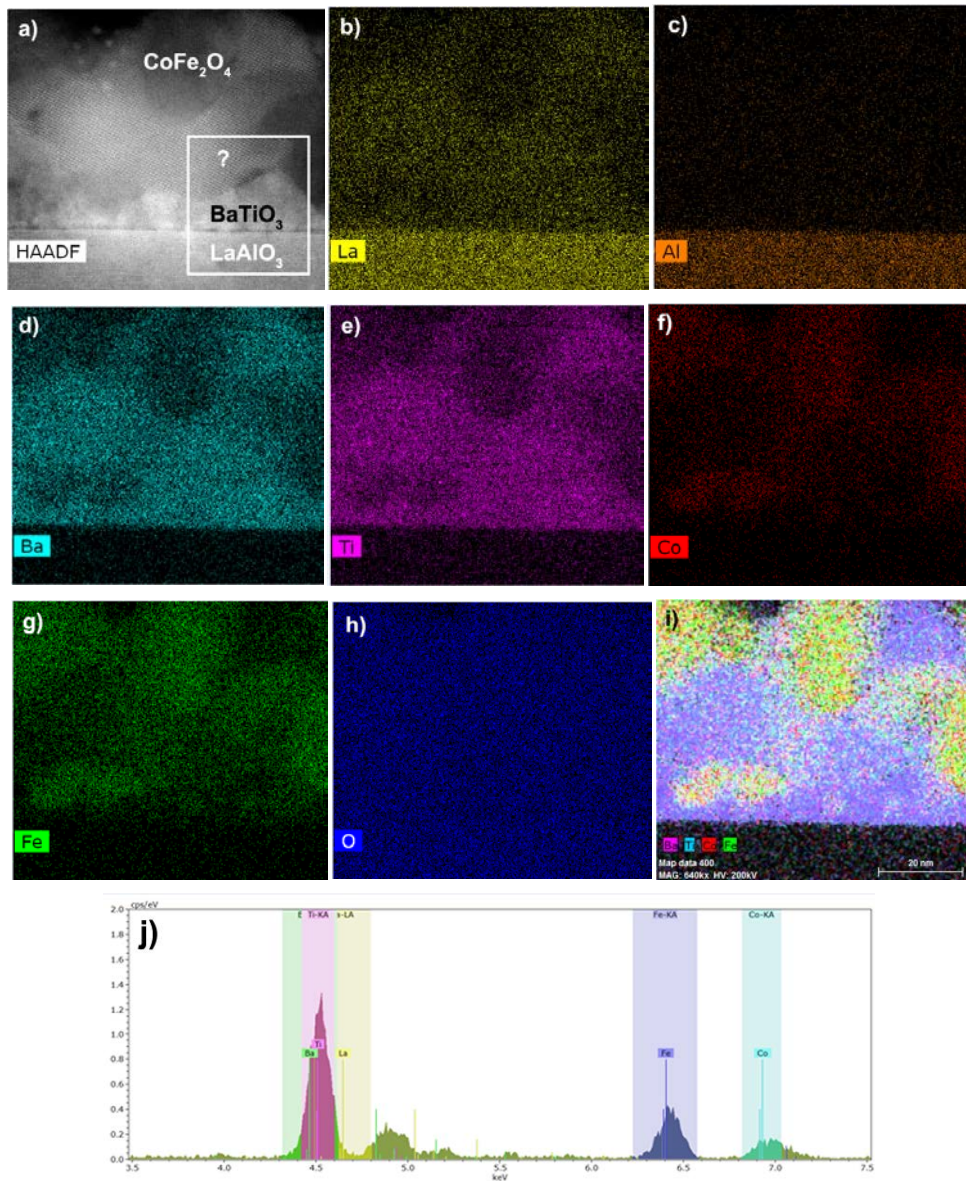
Figure 5.16: a) High resolution HAADF-STEM image of a cross section of the LaAlO₃//BaTiO₃/CoFe₂O₄ film. EDX mapping of the individual elements in the region marked by white square in a): b) La; c) Al; d) Ba; e) Ti; f) Co; g) Fe; h) O; i) Ba-Ti-Co-Fe, and j) spectrum of the impurity phase.
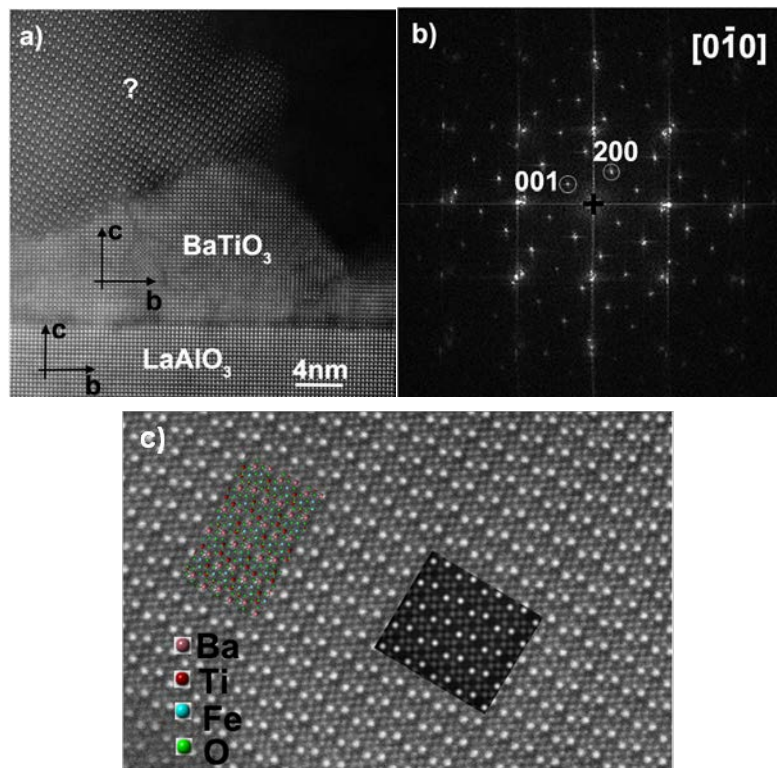
Figure 5.17: a) High resolution HAADF-STEM image of the cross section of the LaAlO$_3$//BaTiO$_3$/CoFe$_2$O$_4$ film containing the unknown phase; b) Fourier transform of this phase was indexed using the cell parameters of Ba$_2$Ti$_4$Fe$_2$O$_{13}$; c) HAADF-STEM image of the phase together with inset showing the projection and simulation in zone axis [0-10] of the crystal Ba$_2$Ti$_4$Fe$_2$O$_{13}$.

Interdiffusion of constituent phases in CoFe$_2$O$_4$-BaTiO$_3$ composites has been reported for both bulk ceramic and thin films [25-27]. Formation of undesired phases (BaFe$_{12}$O$_{19}$ or BaCo$_6$Ti$_6$O$_{19}$) is ascribed to high sintering temperatures during ceramic processing [27]. Concerning the thin films, a group of authors [25, 26] report on chemical interaction between CoFe$_2$O$_4$ and BaTiO$_3$ for the films grown by PLD. First, Aguesse et al. [25] discuss on possible diffusion between CoFe$_2$O$_4$ and BaTiO$_3$ layers in multilayer structure obtained at the deposition temperature of 700°C. In order to confirm their hypothesis, they mixed together the single phase spinel and perovskite and annealed them at 1100°C for 5 hours. XRD analysis of the mixture after thermal treatment showed presence of starting phase, CoFe$_2$O$_4$ and BaTiO$_3$, and a secondary Ba(Fe$_{10}$Ti$_2$)O$_{19}$

phase. However, when they repeated the same experiment with $SrTiO_3$ instead of $BaTiO_3$ no chemical reaction was observed which point to chemical compatibility between $CoFe_2O_4$ and $SrTiO_3$, even at high temperatures [25]. Then, Axelsson et al. [26] reported on the presence of low crystallinity interfacial layer between the $CoFe_2O_4$ thin film and $BaTiO_3$ single crystal substrate, as revealed by HR-TEM. They related the formation of this layer to interdiffusion and chemical incompatibility of $CoFe_2O_4$ and $BaTiO_3$ [25, 26]. The other composite systems were also affected by interdiffusion of phases. Thus, electron energy loss spectroscopy (EELS) results indicate diffusion of Ti and Fe in $CoFe_2O_4$ and $PbTiO_3$, respectively, in self-assembled $PbTiO_3$-$CoFe_2O_4$ nanostructures grown by PLD on a $SrTiO_3$ substrate at 630° [28].

In some of these reports, the deterioration in magnetic properties is related to chemical interaction between the phases [25, 26] demonstrating the importance of the interfacial chemistry on the final functional properties.

5.8 PFM studies

Ferroelectric properties of $BaTiO_3$-$CoFe_2O_4$ and $BiFeO_3$-$CoFe_2O_4$ composites deposited on Nb doped $SrTiO_3$ substrates were analyzed locally by piezoresponse force microscopy (PFM). This part of the research is done in collaboration with dr. Alexander Volodin from the Laboratory of Solid State Physics and Magnetism, Department of Physics and Astronomy, KU Leuven. The underlying Nb doped $SrTiO_3$ substrate, being a conductive material, is used as an electrode. PFM results of morphology and phase scans are shown in Figures 5.18 and 5.19, for $BiFeO_3$-$CoFe_2O_4$ and $BaTiO_3$-$CoFe_2O_4$ composites, respectively. An out-of-plane piezoelectric response was observed in both composite materials. Electrical poling was performed by scanning in contact mode with the conductive probe biased at -10 V and +10 V over different areas. The change of phase contrast in the polarized areas indicates that the perpendicular component of polarization can have opposite directions and can be switched between two stable states in the perovskite matrix.
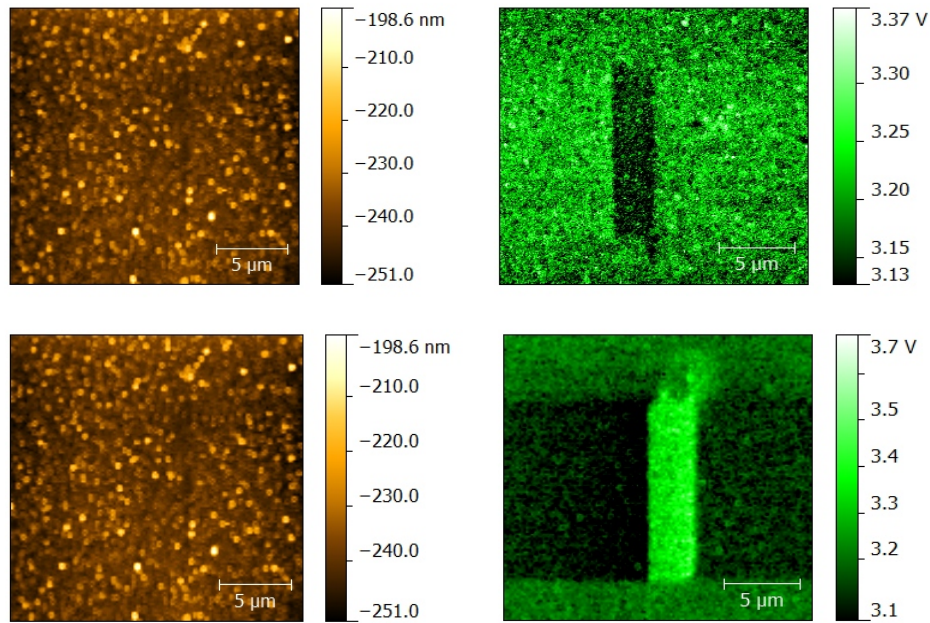
Figure 5.18: Piezoresponse force microscopy measurements of BiFeO$_3$-CoFe$_2$O$_4$ composite film on Nb doped SrTiO$_3$ substrate. Images on the left side (top and bottom) represent morphology. Images on the right side (top and bottom) are phase images of the PFM response along the vertical direction. In the different parts of the scanned area 2×10 μm^2 rectangular regions are poled by an applied voltage (-10 V) (right top image) as well as reverse voltage (+10 V) (right bottom image) leading to a contrast change.
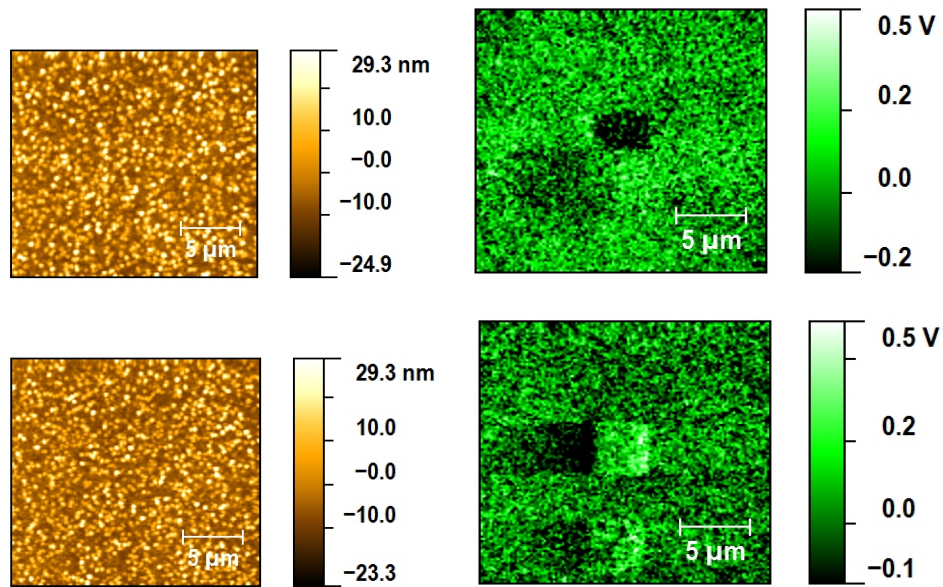
Figure 5.19: Piezoresponse force microscopy measurements of BaTiO$_3$-CoFe$_2$O$_4$ composite film on Nb doped SrTiO$_3$ substrate. Left images (top and bottom) represent morphology. Right images (top and bottom) are phase images of PFM response along the vertical direction. In the different parts of the scanned area square-like regions are poled by an applied voltage (-10 V) (right top image) as well as reverse voltage (+10 V) (right bottom image) leading to a contrast change.

5.9 Magnetic properties

Magnetic properties of the BTO-CFO and BFO-CFO composites on both macroscopic and local level were studied by superconducting quantum interference device (SQUID) magnetometry and magnetic force microscopy (MFM). SQUID measurements were performed during the Short Term Scientific Mission in the group of prof. dr. S. van Dijken at Aalto University, Finland. MFM measurements were carried out in collaboration with dr. Alexander Volodin in the Laboratory of Solid State Physics and Magnetism, Department of Physics and Astronomy, KU Leuven.

5.9.1 SQUID measurements

Measurements of magnetization as function of an applied magnetic field at room temperature were carried out on BFO-CFO and BTO-CFO composite films on (001)-oriented LAO and STO substrates using SQUID magnetometry with the magnetic field applied perpendicular (out-of-plane, OP) and parallel (in-plane, IP) to the substrate surface. The presented magnetic measurements have been adjusted by subtracting the diamagnetic part of the signal originating from the substrates.

Figure 5.20 shows magnetization curves for BFO-CFO composite films on LAO and STO substrates obtained by scanning the magnetic field back and forth between 70 and -70 kOe at room temperature.

Figure 5.20: Magnetization hysteresis loops measured at room temperature with the field applied in the plane (IP) and out of plane (OP) for the $BiFeO_3$-$CoFe_2O_4$ samples on (001) LAO and (001) STO.

144

BFO-CFO nanocomposite on STO has a coercive field in the IP direction of ~1 kOe and 750 Oe in OP direction and the nanocomposite on LAO has a coercive field of ~1 kOe. Resemblance between hysteresis loops obtained in the in-plane and out-of-plane directions suggests a small anisotropic magnetic property. The saturation magnetization values for the BFO-CFO composite film on LAO and STO substrates are ~500 emu/cm^3 and ~700 emu/cm^3, respectively. These values significantly exceed 400 emu/cm^3 which corresponds to the saturation magnetization of CFO bulk [29]. Normalization of these curves to the volume of CFO in the films is avoided since already rather high values for the film magnetization imply that CFO is probably not the only source of magnetism in these samples.

Therefore, to consider the contribution of each constituent phase in the composite to magnetization it is useful to separately analyse the magnetic response of single (i. e. no nanocomposite) BFO and CFO thin films to an applied magnetic field. Thus, we deposited CFO films on LAO, annealed them at 700°C and subjected them to SQUID measurements at room temperature. For a CFO film thickness of about 100 nm, the calculated magnetization saturates around 360 emu/cm^3 which is close to CFO bulk value, see Figure 5.21. Furthermore, in chapter 4 it is shown that BFO films annealed at 700°C exhibit a weak ferromagnetic response up to 3 emu/cm^3 at room temperature which implies the absence of ferromagnetic secondary phases. Concerning the published data on the magnetic properties and saturation magnetization of the BFO films, Béa et al. [30] report the extreme case for the BFO films containing larger amount of γ-Fe$_2$O$_3$ phase (around 80% of the film volume) when the saturation magnetization of about 380 emu cm^{-3} was measured at 10 K for 70 nm thick film. In many other studies, the authors report on the weak magnetic moment and saturation magnetization from 2 emu cm^{-3} to 30 emu cm^{-3} at room temperature [31-37]. However, it seems that in this case coexistence of CFO and BFO in the composite films results in a large magnetic response which can be compared, to a certain level with observations by Dix et al. who reported on a gradual decrease in Bi content and an increased ferromagnetic response in BFO-CFO composites when samples were processed at higher temperatures: 650°C, 675°C and 700°C [38]. They suggest that such an enhanced magnetization in BFO-CFO composites could be due to the formation of spurious

Fe_xO_y phases, although XRD analysis shows the presence of these phases only above 700°C. Moreover, they argue that CFO crystallites, due to structural and dimensional similarities, may behave as a template and promote the growth of isomorphous Fe-O magnetic oxides (such as γ-Fe_2O_3 or Fe_3O_4) on its surface. According to these authors, morphological distinction by means of SEM and AFM can be hindered by shape similarity between Fe-O and CFO crystallites. However, it is important to mention that for their study they used the PLD method to grow BFO-CFO composite films, where processing parameters are different compared to the solution-gel method used in our work. This difference is primarily related to the applied pressure during pulsed laser deposition and its influence on Bi_2O_3 volatility and sublimation of Bi at certain temperatures.

On the other hand, magnetic enhancement can also result from magnetic interactions between antiferromagnetic and ferrimagnetic nanostructures [5]. Thus, Chen et al. observed significantly higher saturation magnetization in the BFO-CFO self-assembled heterostructures compared with STO-CFO heterostructures and CFO-BFO bilayers [5]. This enhancement of magnetization suggests that antiferromagnetism of BFO matrix might have a strong influence on CFO nanopillars. By means of magnetization experiments and element-selective X-ray magnetic circular dichroism (XMCD), the authors found significant enhancement of the ordered magnetic moment of Co^{2+} ions for the BFO-CFO nanostructure. In addition, they proposed that uncompensated antiferromagnetic Fe^{3+} spins from $BiFeO_3$ are ferromagnetically aligned at the interface contributing to the exchange field that acts on the Co^{2+} together with the exchange field from B-site Fe^{3+} ions in CFO. Due to a large surface-to-volume ratio in these heterostructures, magnetic exchange coupling is induced at the interface between ferrimagnetic and antiferromagnetic nanostructures resulting in the strong enhancement of magnetization self-assembled BFO-CFO composite [5].

To be able to better understand and explain the high magnetization values observed for BFO-CFO composites in this work, more detailed characterization of the composite is necessary, including techniques offering very sensitive local probe to study valence state, as well as spin and orbit characteristics of constituent elements.
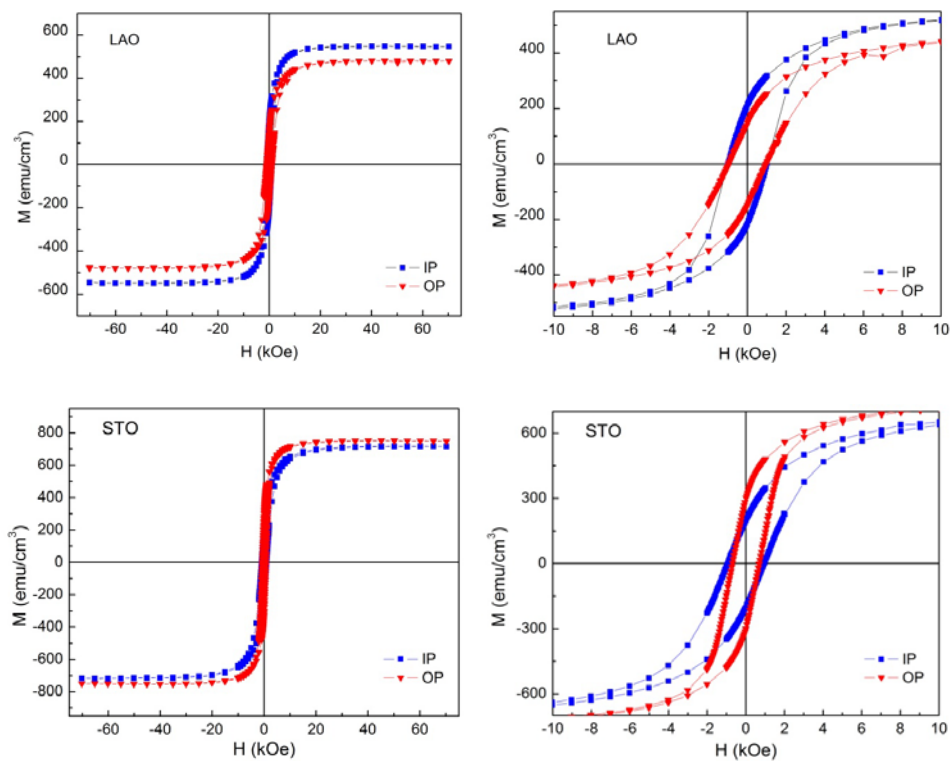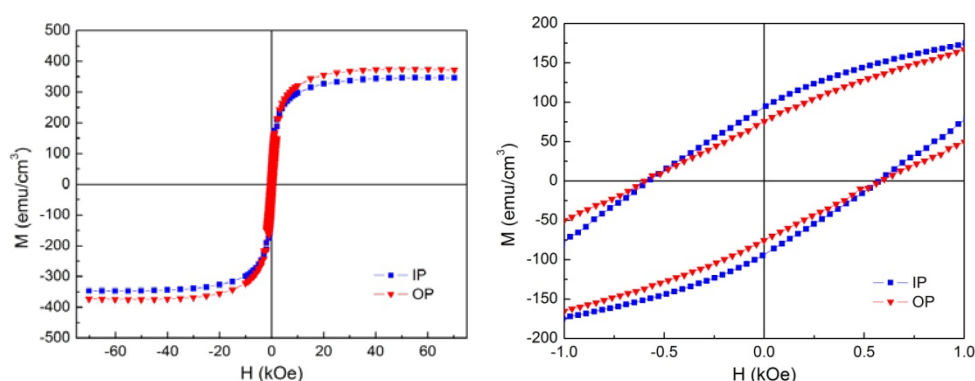
Figure 5.21: Magnetization hysteresis loops measured at room temperature with the field applied in-plane (IP) and out-of-plane (OP) to $CoFe_2O_4$ film on (001) LAO substrate.

Figure 5.22 shows the magnetization hysteresis loops corresponding to $BaTiO_3$-$CoFe_2O_4$ composite films on LAO and STO substrates. The magnetization has been normalized to the volume fraction of CFO (~30%). The general observation is that characteristics are similar along in-plane and out-of-plane directions for films on LOA substrates as well as on STO substrates, implying isotropic magnetic behavior for both. Nanocomposite films exhibit small coercive fields (H_c) of ~150 Oe and 85 Oe on LAO and STO, respectively. In the case of the films on the LAO substrate, saturation magnetization (M_s) values are about 300-350 emu/cm^3 while the films on STO exhibit a lower magnetization of about 220-250 emu/cm^3 which can be an indication of a better structural quality of the CFO phase in the composite on LAO. The M_s values reported for BTO-CFO films on STO substrate are about 350 emu/cm^3 for composites prepared by PLD [2] while Liu et al. reported 370 emu/cm^3 for the sol-gel derived composite film [13]. The results presented in this work are comparable with the results by Liu et al. in terms of the isotropic magnetic behaviour and small coercive field. The isotropic behaviour points to three-dimensionally distributed nanoparticulate heterostructures in the $BaTiO_3$-$CoFe_2O_4$ [13] which contrasts with the highly anisotropic columnar nano-composite grown by PLD [2]. Concerning the coercive field, it is known that as the particle size decreases toward some critical particle diameter (D_c) when it becomes a single-domain particle, the coercive field increases reaching its maximum. In this case, the increase of coercive field could be related to the decreasing number of domains while magnetization reversal of

the single-domain particle no longer occurs through the domain wall motion but by coherent spin rotation [29]. For CFO particles, this critical diameter is about 70 nm and its corresponding coercive field is around 2 kOe [29]. However, here the CFO grains, according to SEM and TEM studies, are larger than the critical diameter thus magnetization reversal occurs through nucleation and motion of domain walls as more energetically favourable leading to a smaller coercive field.

It is also worth mentioning that the low coercivity and large magnetostriction of the ferromagnetic phase are desirable for an enhanced magnetoelectric coupling.
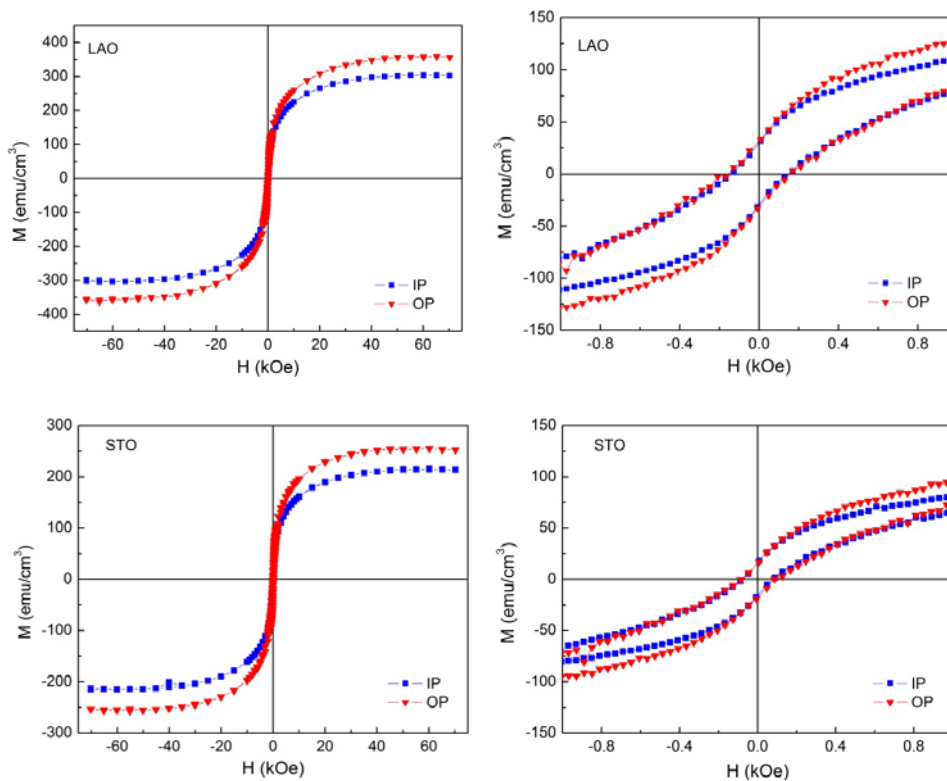
Figure 5.22: Magnetization hysteresis loops measured at room temperature with the field applied in the plane (blue squares) and out of plane (red triangle) for the BTO-CFO samples on (001) LAO and (001) STO. Normalized to CFO volume fraction of 0.3. Graphs on the right are details from the hysteresis loops. Zoom of low field region is on the right.

5.9.2 MFM measurements

Local magnetic data were acquired by magnetic force microscopy (MFM) on $BaTiO_3$-$CoFe_2O_4$ and $BiFeO_3$-$CoFe_2O_4$ composites on Nb doped $SrTiO_3$ substrates. MFM senses the vertical component of the force gradient between the sample and the tip. It is sensitive to the strength and polarity of near-surface stray fields produced by ferromagnetic samples. Figures 5.23 and 5.24 show the topography image and MFM phase response that reveals magnetic activity at the site of the outgrown CFO grains, shown as a blue contrast. In addition, the matrix of BFO-CFO composite shows an enhanced magnetic response which is in agreement with the observed high magnetization values in SQUID measurements. However, it is not yet clear what the cause of this magnetization is although it is possible to speculate that it comes from some iron-rich phase.
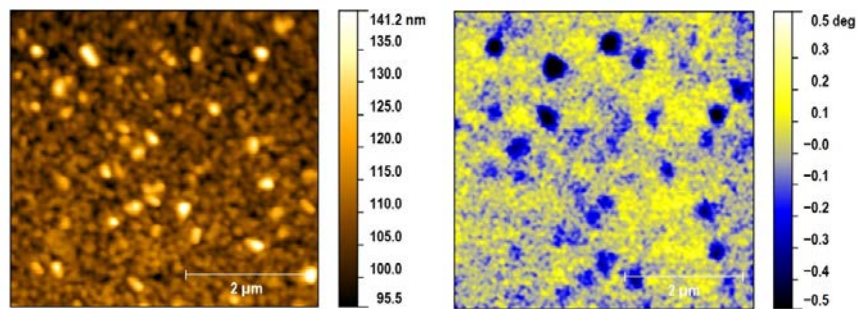
Figure 5.23: MFM measurements of BTO-CFO composite on Nb doped STO substrate. Left image presents morphology. Right image is out-of-plane MFM phase image.
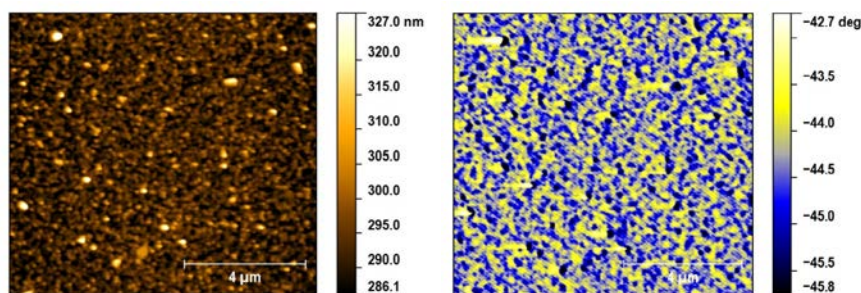
Figure 5.24: MFM measurements of BFO-CFO composite on Nb doped STO substrate. Left image presents morphology. Right image is out-of-plane MFM phase image.

149

5.10 Conclusions

The aqueous chemical solution deposition method was used to grow self-assembled $BaTiO_3$-$CoFe_2O_4$ and $BiFeO_3$-$CoFe_2O_4$ nanocomposite films on two different substrates, (001) LAO and (001) STO. Spontaneous phase separation resulted in the formation of two-phase systems where the spinel $CoFe_2O_4$ phase is embedded in a matrix of ferroelectric perovskite phase. While the perovskite phase growth follows the substrate, CFO nucleates and grows onto the perovskite $BiFeO_3$ or $BaTiO_3$ phase forming blocks and particulates in the matrices, which compared to nanopillar geometry (columnar growth) is another three-dimensional form of nanocomposites. Furthermore, an appropriate choice of substrate promotes the epitaxial stabilization of tetragonal-like $BiFeO_3$ phase offering possibility to tune polarization direction. Detailed structural analysis of the cross section of BTO-CFO films on (001) LAO point to formation of an impurity phase $Ba_2Ti_4Fe_2O_{13}$ probably as a result of phase intermixing.

The composite films exhibit both ferroelectric and ferromagnetic properties. As a result of the nanoparticulate structure of the constituent phases, the nanocomposite thin films show isotropic magnetic properties. The enhanced magnetic response of BFO-CFO composite observed by SQUID and MFM measurements suggests the presence of other magnetically active phases besides CFO or maybe magnetic coupling between antiferromagnetic and ferrimagnetic nanostructures.

With this work we showed that aqueous solution deposition applied here is a very flexible method for the preparation of composite materials with different constituent phases and further optimization of the deposition process gives a perspective for the development of a variety of composite materials not only in multiferroic but also in wider range of metal oxide materials.

5.11 Experimental

5.11.1 Precursor solution synthesis

Co(II) citrate solution

For the synthesis of an aqueous Co(II) citrate solution, Co-citrate ($C_{12}H_{10}Co_3O_{14} \cdot 2H_2O$, 98%, Alfa Aesar) was mixed with citric acid ($C_6H_8O_7$, 99.5%, Sigma Aldrich) in a ratio of 1:2. After addition of water, the mixture was refluxed at 80°C for two hours resulting in a pink precipitation (foam). After cooling to room temperature ammonia (NH_3, 32% in H_2O, extra pure, Merck) was added dropwise dissolving the precipitation and finally a dark purple solution was obtained with a pH value of 8.5. This solution is placed back for refluxing at 80°C for two hours, cooled down and the final pH value was adjusted again to 8.5 by addition of ammonia. After filtration through a 0.1 µm filter (Supor-100, Pall Life Sciences), the solution was diluted with water to obtain a ~0.6 M solution concentration.

BiFeO₃-CoFe₂O₄ precursor solution

$BiFeO_3$-$CoFe_2O_4$ precursor solutions were prepared as follows. Precursor solutions of each of constituent cations were prepared separately. Synthesis procedure of Bi(III) citrate (~1.2 M) and Fe(III) citrate (0.7 M) solutions based on references Hardy [JECS04] and Hardy et al. [JECS09] can be found in the Chapter 3, while the preparation procedure of Co(II) citrate solution (0.6 M) is described in this section. Taking care about the stoichiometric ratio of Bi and Fe for $BiFeO_3$ and stoichiometric ratio of Co and Fe for $CoFe_2O_4$ as well as a 7:3 molar ratio of $BiFeO_3$ against $CoFe_2O_4$, these monometal ion solutions were mixed to obtain the multimetal ions solution. In order to ensure complexation of the metal ions, an appropriate volume of 3 M citric acid ($C_6H_8O_7$, 99.5%, Sigma Aldrich) solution was added to obtain a 2:1 molar ratio of citric acid with respect to the total amount of metal ions. The pH value was adjusted to ~7.5 by addition of ammonia (NH_3, 32% in H_2O, extra pure, Merck) and the solution was heated to 110°C in order to decrease the volume and reach a ~0.6 M concentration of metal ions. The dark red BFO-CFO precursor solution was again

adjusted to a pH value of ~7.5 and a 0.6 M concentration by adding ammonia and water respectively.

BaTiO₃-CoFe₂O₄ precursor solution

$BaTiO_3$-$CoFe_2O_4$ precursor solutions were prepared as follows. First a stoichiometric $BaTiO_3$ precursor solution was prepared according to the procedure described in Chapter 4. The next step in preparation was to mix $BaTiO_3$ precursor solution with Co(II) citrate and Fe(II) citrate (Chapter 3) solutions to achieve the desired composition where the molar ratio of $BaTiO_3$ to $CoFe_2O_4$ was 7:3 and the proper stoichiometric ratio of Co to Fe in $CoFe_2O_4$ was achieved. An appropriate volume of 3 M solution of citric acid ($C_6H_8O_7$, 99.5%, Sigma Aldrich) was added to obtain a 2:1 molar ratio of citric acid with respect to the total amount of metal ions. After addition of ammonia (NH_3, 32% in H_2O, extra pure, Merck) and reaching pH ~7.5, the solution was evaporated at 110°C in order to decrease the volume and obtain metal ion concentration of ~0.6 M. Finally, the pH value was again adjusted to 7.5 and concentration to 0.6 M by adding ammonia and water, respectively.

CoFe₂O₄ precursor solution

Stochiometric CoFe2O4 precursor solution was prepared starting from Co(II) citrate and Fe(II) citrate (Chapter 3) solutions. To achieve a 2:1 molar ratio of citric acid with respect to the total amount of metal ions, a 3 M solution of citric acid was added to this mixture. By dropwise adding of ammonia (NH_3, 32% in H_2O, extra pure, Merck) the pH value was increased to ~7.5 and solution was further evaporated at 110°C to decrease volume and reach the metal ion concentration of ~0.6 M. Finally, pH was again adjusted to 7.5 and the concentration to 0.6 M by adding ammonia and water, respectively.

5.11.2 Thin film deposition

Thin films were deposited on single crystal substrates, (001) $LaAlO_3$ and (001) $SrTiO_3$ by spin coating. The one-side polished substrates with dimensions of 10x10 mm² and thickness of 0.5 mm were purchased from Neyco, France. Prior

to deposition, hydrophilicity of the substrate surface was optimized through a chemical treatment with SPM/APM (sulphuric acid peroxide/ammonia peroxide mixture) [39] resulting in improved surface wettability. All solutions were filtered through a syringe filter of 0.2µm (Acrodisc Premium, Pall Life Sciences) for their deposition onto the substrates and thin layers were spin coated at a rotation speed of 6000 rpm for 30 s, with an acceleration of 1000 rpm/s. After spin coating, the thin layers were treated on three different hot plates: 1 min at 110°C, 2 min at 260°C and 2 min at 480°C. The cycle of deposition and hot plate treatment was repeated three times prior to a final annealing in a tube furnace in a dry air using a gas flow of 0.5 l/min. BFO-CFO and CFO as-deposited films were annealed at 700°C for 1 hour, while BTO-CFO as-deposited films were annealed at 900°C for 1 hour.

5.11.3 Characterization techniques

The exact concentration of the metal ion in the monometal precursors was determined by means of inductively coupled plasma atomic emission spectroscopy (ICP–AES, Optima 3300 DV, PerkinElmer). Samples were prepared by diluting the precursor solutions with 5% HNO_3 (J.T. Baker, 69-70%, Baker Instra-analyzed Reagent) so that the expected concentrations fall within the calibration range of 1 to 10 ppm.

Thermal gravimetric analysis (TGA) is performed on TGA 51 Thermogravimetric analyzer (TA Instruments) to study thermal decomposition of obtained gels. The samples were heated from room temperature to 800°C with the heating rate of 10°C/min in a dry air.

Powder crystallization is studied in situ by means of high-temperature XRD (Bruker D8, Cu K with an Anton Paar heating module) in static air. The samples were heated from 450 to 900°C with the heating rate of 10°C/min while XRD patterns were recorded every 50°C. The crystal structure of the obtained composite films was analyzed using a Bruker D8 Discover diffractometer operating in θ–2θ mode with the parallel beam geometry using a Göbel mirror (line focus, Cu K_α radiation).

SEM images of the thin films were taken with a FEI Quanta 200 FEG-SEM. The film topography was analyzed by atomic force microscopy, AFM, Veeco Dimension Microscope with Digital Instrument Nanoscope III controller in tapping mode using a Si cantilever tip.

The TEM samples for electron microscopy were prepared by Focused Ion Beam (FIB) using a Helios NanoLab 650 with a Ga^+ focused ion beam (500eV- 30keV). The $BiFeO_3$-$CoFe_2O_4$ or $BaTiO_3$-$CoFe_2O_4$ composite films on $LaAlO_3$ substrate were coated with 22 nm of a carbon amorphous layer, in order to protect them during the milling. The samples were investigated by transmission electron microscopy, using a FEI Tecnai G2 instrument operated at 200kV. HAADF-STEM imaging and EDX measurements were performed using a FEI Titan microscope operated at 200 kV/300kV.

PFM measurements were carried out at ambient conditions with an Agilent 5500 microscope. PFM images were acquired in contact mode at 30 kHz, with AC voltage amplitudes of 2–5V using PPP-EFM probes from NanoAndMore with PtIr coating.

Magnetic properties of the samples were measured with superconducting quantum interface device (SQUID) magnetometer of Quantum Design MPMSXL-5 at room temperature with the magnetic field in plane and out of plane of the thin films. Magnetic force microscope (MFM) was used for investigation of local magnetic properties of composite films. MFM measurements were made at ambient conditions with a Agilent 5500 microscope. MFM images were acquired in non-contact ("flying") mode using PPP-MFM probes from NanoAndMore with Co-Cr coating.

References

[1] C.A.F. Vaz, J. Hoffman, C.H. Anh, R. Ramesh, Magnetoelectric Coupling Effects in Multiferroic Complex Oxide Composite Structures, Adv. Mater., 22 (2010) 2900-2918.

[2] H. Zheng, J. Wang, S.E. Lofland, Z. Ma, L. Mohaddes-Ardabili, T. Zhao, L. Salamanca-Riba, S.R. Shinde, S.B. Ogale, F. Bai, D. Viehland, Y. Jia, D.G. Schlom, M. Wuttig, A. Roytburd, R. Ramesh, Multiferroic $BaTiO_3$-$CoFe_2O_4$ nanostructures, Science, 303 (2004) 661-663.

[3] N. Dix, R. Muralidharan, J.M. Rebled, S. Estrade, F. Peiro, M. Varela, J. Fontcuberta, F. Sanchez, Selectable Spontaneous Polarization Direction and Magnetic Anisotropy in $BiFeO_3$-$CoFe_2O_4$ Epitaxial Nanostructures, ACS Nano, 4 (2010) 4955-4961.

[4] H.M. Zheng, F. Straub, Q. Zhan, P.L. Yang, W.K. Hsieh, F. Zavaliche, Y.H. Chu, U. Dahmen, R. Ramesh, Self-assembled growth of $BiFeO_3$-$CoFe_2O_4$ nanostructures, Adv. Mater., 18 (2006) 2747.

[5] Y.J. Chen, Y.H. Hsieh, S.C. Liao, Z.W. Hu, M.J. Huang, W.C. Kuo, Y.Y. Chin, T.M. Uen, J.Y. Juang, C.H. Lai, H.J. Lin, C.T. Chen, Y.H. Chu, Strong magnetic enhancement in self-assembled multiferroic-ferrimagnetic nanostructures, Nanoscale, 5 (2013) 4449-4453.

[6] Y.H. Hsieh, H.H. Kuo, S.C. Liao, H.J. Liu, Y.J. Chen, H.J. Lin, C.T. Chen, C.H. Lai, Q. Zhan, Y.L. Chueh, Y.H. Chu, Tuning the formation and functionalities of ultrafine $CoFe_2O_4$ nanocrystals via interfacial coherent strain, Nanoscale, 5 (2013) 6219-6223.

[7] A. Imai, X. Cheng, H.L.L. Xin, E.A. Eliseev, A.N. Morozovska, S.V. Kalinin, R. Takahashi, M. Lippmaa, Y. Matsumoto, V. Nagarajan, Epitaxial $Bi_5Ti_3FeO_{15}$-$CoFe_2O_4$ Pillar-Matrix Multiferroic Nanostructures, ACS Nano, 7 (2013) 11079-11086.

[8] W.I. Liang, Y.M. Liu, S.C. Liao, W.C. Wang, H.J. Liu, H.J. Lin, C.T. Chen, C.H. Lai, A. Borisevich, E. Arenholz, J. Li, Y.H. Chu, Design of magnetoelectric coupling in a self-assembled epitaxial nanocomposite via chemical interaction, Journal of Materials Chemistry C, 2 (2014) 811-815.

[9] S.C. Liao, P.Y. Tsai, C.W. Liang, H.J. Liu, J.C. Yang, S.J. Lin, C.H. Lai, Y.H. Chu, Misorientation Control and Functionality Design of Nanopillars in Self-

Assembled Perovskite-Spinel Heteroepitaxial Nanostructures, ACS Nano, 5 (2011) 4118-4122.

[10] Z.G. Wang, Y.X. Li, R. Viswan, B.L. Hu, V.G. Harris, J.F. Li, D. Viehland, Engineered Magnetic Shape Anisotropy in $BiFeO_3$-$CoFe_2O_4$ Self-Assembled Thin Films, ACS Nano, 7 (2013) 3447-3456.

[11] N. Dix, V. Skumryev, V. Laukhin, L. Fabrega, F. Sanchez, J. Fontcuberta, Sputtering growth and characterization of $CoFe_2O_4$-$BaTiO_3$ nanostructures, Materials Science and Engineering B-Solid State Materials for Advanced Technology, 144 (2007) 127-131.

[12] H.M. Luo, H. Yang, S.A. Bally, O. Ugurlu, M. Jain, M.E. Hawley, T.M. McCleskey, A.K. Burrell, E. Bauer, L. Civale, T.G. Holesinger, Q.X. Jia, Self-assembled epitaxial nanocomposite $BaTiO_3$-$NiFe_2O_4$ films prepared by polymer-assisted deposition, J. Am. Chem. Soc., 129 (2007) 14132-+.

[13] B. Liu, T. Sun, J.Q. He, V.P. Dravid, Sol-Gel-Derived Epitaxial Nanocomposite Thin Films with Large Sharp Magnetoelectric Effect, ACS Nano, 4 (2010) 6836-6842.

[14] A. Hardy, J. D'Haen, H. Van den Rul, M.K. Van Bael, J. Mullens, Crystallization of alkaline earth zirconates and niobates from compositionally flexible aqueous solution-gel syntheses, Mater. Res. Bull., 44 (2009) 734-740.

[15] A. Hardy, S. Gielis, H. Van den Rul, J. D'Haen, M.K. Van Bael, J. Mullens, Effects of precursor chemistry and thermal treatment conditions on obtaining phase pure bismuth ferrite from aqueous gel precursors, J. Eur. Ceram. Soc., 29 (2009) 3007-3013.

[16] I. Truijen, A. Hardy, M.K. Van Bael, H. Van den Rul, J. Mullens, Study of the decomposition of aqueous citratoperoxo-Ti(IV)-gel precursors for titania by means of TGA-MS and FTIR, Thermochim. Acta, 456 (2007) 38-47.

[17] R.J. Zeches, M.D. Rossell, J.X. Zhang, A.J. Hatt, Q. He, C.H. Yang, A. Kumar, C.H. Wang, A. Melville, C. Adamo, G. Sheng, Y.H. Chu, J.F. Ihlefeld, R. Erni, C. Ederer, V. Gopalan, L.Q. Chen, D.G. Schlom, N.A. Spaldin, L.W. Martin, R. Ramesh, A Strain-Driven Morphotropic Phase Boundary in $BiFeO_3$, Science, 326 (2009) 977-980.

[18] N. Dix, R. Muralidharan, M. Varela, J. Fontcuberta, F. Sanchez, Mapping of the epitaxial stabilization of quasi-tetragonal $BiFeO_3$ with deposition temperature, Appl. Phys. Lett., 100 (2012).

[19] H. Ryu, P. Murugavel, J.H. Lee, S.C. Chae, T.W. Noh, Y.S. Oh, H.J. Kim, K.H. Kim, J.H. Jang, M. Kim, C. Bae, J.G. Park, Magnetoelectric effects of nanoparticulate $Pb(Zr_{0.52}Ti_{0.48})O_3$-$NiFe_2O_4$ composite films, Appl. Phys. Lett., 89 (2006).

[20] S.M. Ayguen, J.F. Ihlefeld, W.J. Borland, J.-P. Maria, Permittivity scaling in $Ba_{1-x}Sr_xTiO_3$ thin films and ceramics, J. Appl. Phys., 109 (2011).

[21] C.T. Shelton, P.G. Kotula, G.L. Brennecka, P.G. Lam, K.E. Meyer, J.P. Maria, B.J. Gibbons, J.F. Ihlefeld, Chemically Homogeneous Complex Oxide Thin Films Via Improved Substrate Metallization, Adv. Funct. Mater., 22 (2012) 2295-2302.

[22] H.M. Zheng, J. Kreisel, Y.H. Chu, R. Ramesh, L. Salamanca-Riba, Heteroepitaxially enhanced magnetic anisotropy in $BaTiO_3$-$CoFe_2O_4$ nanostructures, Appl. Phys. Lett., 90 (2007).

[23] H. Zheng, J. Wang, L. Mohaddes-Ardabili, M. Wuttig, L. Salamanca-Riba, D.G. Schlom, R. Ramesh, Three-dimensional heteroepitaxy in self-assembled $BaTiO_3$-$CoFe_2O_4$ nanostructures, Appl. Phys. Lett., 85 (2004) 2035-2037.

[24] R.D. Adams, R. Layland, M. Danot, C. Payen, A new mixed metal titanate: The synthesis and characterization of $Ba_2Fe_2Ti_4O_{13}$, Polyhedron, 15 (1996) 2567-2571.

[25] F. Aguesse, A.-K. Axelsson, M. Valant, N.M. Alford, Enhanced magnetic performance of $CoFe_2O_4$/$BaTiO_3$ multilayer nanostructures with a SrTiO3 ultra-thin barrier layer, Scr. Mater., 67 (2012) 249-252.

[26] A.-K. Axelsson, F. Aguesse, V. Tileli, M. Valant, N.M. Alford, Growth mechanism and magnetism of $CoFe_2O_4$ thin films; Role of the substrate, J. Alloys Compd., 578 (2013) 286-291.

[27] M. Fiebig, Revival of the magnetoelectric effect, Journal of Physics D-Applied Physics, 38 (2005) R123-R152.

[28] J.H. Li, I. Levin, J. Slutsker, V. Provenzano, P.K. Schenck, R. Ramesh, J. Ouyang, A.L. Roytburd, Self-assembled multiferroic nanostructures in the $CoFe_2O_4$-$PbTiO_3$ system, Appl. Phys. Lett., 87 (2005).

[29] B.D. Cullity, C.D. Graham, Introduction to Magnetic Materials, second ed., Wiley, New Jersey, 2009.

[30] H. Bea, M. Bibes, A. Barthelemy, K. Bouzehouane, E. Jacquet, A. Khodan, J.P. Contour, S. Fusil, F. Wyczisk, A. Forget, D. Lebeugle, D. Colson, M. Viret,

Influence of parasitic phases on the properties of BiFeO$_3$ epitaxial thin films, Appl. Phys. Lett., 87 (2005).

[31] H. Bea, M. Bibes, S. Petit, J. Kreisel, A. Barthelemy, Structural distortion and magnetism of BiFeO$_3$ epitaxial thin films: A Raman spectroscopy and neutron diffraction study, Philos. Mag. Lett., 87 (2007) 165-174.

[32] C.-J. Cheng, C. Lu, Z. Chen, L. You, L. Chen, J. Wang, T. Wu, Thickness-dependent magnetism and spin-glass behaviors in compressively strained BiFeO$_3$ thin films, Appl. Phys. Lett., 98 (2011).

[33] Z.X. Cheng, X.L. Wang, H. Kimura, K. Ozawa, S.X. Dou, La and Nb codoped BiFeO(3) multiferroic thin films on LaNiO$_3$/Si and IrO$_2$/Si substrates, Appl. Phys. Lett., 92 (2008).

[34] J. Dho, X. Qi, H. Kim, J.L. MacManus-Driscoll, M.G. Blamire, Large electric polarization and exchange bias in multiferroic BiFeO$_3$, Adv. Mater., 18 (2006) 1445-+.

[35] W. Eerenstein, F.D. Morrison, J. Dho, M.G. Blamire, J.F. Scott, N.D. Mathur, Comment on "Epitaxial BiFeO$_3$ multiferroic thin film heterostructures", Science, 307 (2005) 1203-1203.

[36] J.F. Ihlefeld, A. Kumar, V. Gopalan, D.G. Schlom, Y.B. Chen, X.Q. Pan, T. Heeg, J. Schubert, X. Ke, P. Schiffer, J. Orenstein, L.W. Martin, Y.H. Chu, R. Ramesh, Adsorption-controlled molecular-beam epitaxial growth of BiFeO$_3$, Appl. Phys. Lett., 91 (2007).

[37] P. Jalkanen, V. Tuboltsev, B. Marchand, A. Savin, M. Puttaswamy, M. Vehkamaki, K. Mizohata, M. Kemell, T. Hatanpaa, V. Rogozin, J. Raisanen, M. Ritala, M. Leskela, Magnetic Properties of Polycrystalline Bismuth Ferrite Thin Films Grown by Atomic Layer Deposition, J. Phys. Chem. Lett., 5 (2014) 4319-4323.

[38] N. Dix, R. Muralidharan, B. Warot-Fonrose, M. Varela, F. Sanchez, J. Fontcuberta, Critical Limitations in the Fabrication of Biferroic BiFeO$_3$-CoFe$_2$O$_4$ Columnar Nanocomposites Due to Bismuth Loss, Chem. Mater., 21 (2009) 1375-1380.

[39] M.K. Van Bael, D. Nelis, A. Hardy, D. Mondelaers, K. Van Werde, J. D'Haen, G. Vanhoyland, H. Van den Rul, J. Mullens, L.C. Van Poucke, F. Frederix, D.J. Wouters, Aqueous chemical solution deposition of ferroelectric thin films, Integr. Ferroelectr., 45 (2002) 113-122.

Summary, conclusions and outlook

Magnetoelectric multiferroics are materials with a simultaneous presence of ferroelectric and (anti)ferromagnetic orders while mutual coupling between the order parameters enables controlling magnetization by an applied electric field or polarization by an applied magnetic field. Therefore, these materials in thin films are very attractive for applications in multifunctional devices where a single element can perform multiple tasks leading to miniaturization of electronic devices and an enhanced performance. Facing the challenge for functional materials at room temperature, the research in the multiferroic field has evolved in two directions, one of which concerns single phase ("intrinsic") multiferroics where bismuth ferrite ($BiFeO_3$) thin films have gained considerable attention while the other pathway leads towards composite multiferroics which comprise ferroelectric and magnetic constituent phases. However, one of the most promising room-temperature single-phase multiferroics, $BiFeO_3$, has issues concerning phase formation, phase purity and thermal stability which have a tremendous influence on the material properties and its applicability. Furthermore, the scarcity of room-temperature intrinsic multiferroics contributes to an intensive search for new composite materials and heterostructures with enhanced magnetoelectric properties.

The work presented in this thesis deals with the deposition and characterization of solution-derived $BiFeO_3$ thin films as well as different composite heterostructures using aqueous chemical solution deposition as a cost-effective and environmentally friendly method. The first part of the project aims at understanding the influence of different processing parameters and substrate selection on the $BiFeO_3$ phase formation and thermal stability of the obtained thin films. In the second part of the project, the goal was creating self-assembled composite heterostructures with various constituent phases using the flexibility of solution chemistry and to further investigate the potential of such solution-derived nanostructures in the field of multiferroics.

Chapter 3 focuses on the influence of various processing conditions on the thermal stability of $BiFeO_3$ films obtained via aqueous solution deposition on platinised silicon substrates. From the perspective of secondary phase formation as a result of the $BiFeO_3$ decomposition process, investigated parameters such as annealing temperature and time, film thickness, Bi excess and Ti substitution had different effects. First indications of thermal instability of the $BiFeO_3$ thin film appeared at an annealing temperature of 650°C as some microstructural inhomogeneities, while a significant amount of iron-rich $Bi_2Fe_4O_9$ phase formed at 700°C as a result of $BiFeO_3$ film decomposition. $Bi_2Fe_4O_9$ grains which were embedded in the $BiFeO_3$ matrix nucleate at the film/substrate interface and continue to grow towards the film surface through depletion of $BiFeO_3$ grains, only changing their size and shape as a function of film thickness. The obtained results suggest a loss of Bi from the films at higher temperatures, possibly not only due to volatilization but also due to high diffusion towards the substrate and possible interaction with the Pt electrode. Formation of a Bi-rich layer under the Pt electrode during annealing of a film deposited from only Bi precursor solution proves the tendency of Bi to diffuse into the substrate at higher processing temperature.

To suppress the decomposition of $BiFeO_3$ and the formation of the iron rich phase, the strategy is to avoid Bi deficiency in the film resulting from the Bi diffusion. Thus, shorter annealing times or addition of Bi up to 30 mol% in precursor solution could be considered as possible solutions. Another approach for improving the stability of the BFO phase is substitution of Fe by aliovalent Ti where a limitation of the Bi diffusion occurs probably due to inhibition of oxygen vacancies formation or even some nanoscale Ti precipitation. The findings presented here are applicable not only to other thin films with Bi-based compounds but also to films that contain highly diffusible compounds when control over phase formation is crucial.

Further results on the phase formation and thermal stability of $BiFeO_3$ thin films presented in chapter 4 concern the influence of different substrates and buffer layers. Here, deposition of $BiFeO_3$ precursor solution on silicon based substrates, single crystal substrates and buffered silicon substrates and subsequent processing at higher temperature points to two opposite aspects of film/substrate relation. One aspect is related to the decomposition of the $BiFeO_3$

films on silicon substrates which in some cases goes to such an extreme level that $BiFeO_3$ was not detectable any more as a constituent phase of the film. As a result, different secondary phases form depending on the type of silicon substrate used whereby some of the compounds are products of interactions between film and substrate. However, rather different film/substrate relation was observed in the case of $BiFeO_3$ films on (001) $LaAlO_3$ and (001) $SrTiO_3$ single crystal substrates since there was no evidence of film decomposition. Moreover, the films deposited on these perovskite based substrates were highly epitaxial with a (001) orientation. The stabilized $BiFeO_3$ phase is a result of epitaxial growth on substrates with which the film has similarities in terms of structure and lattice parameters. The obtained films exhibit a weak ferromagnetic response (~2-3 emu/cm^3) at room temperature which is a characteristic of $BiFeO_3$ film when epitaxial strain is induced. Furthermore, the results of magnetic measurements point to the absence of impurity phases with a strong magnetic response. Regarding the buffer layers effect on the thermal stability of a BFO film, TiO_2 buffer and BFO films exhibit a strong tendency to interact, while the films on perovskite $BaTiO_3$ or $SrTiO_3$ retain the $BiFeO_3$ phase. Thus, structural resemblance between film and substrate, as well as chemical compatibility should be taken into account during substrate selection for the deposition of $BiFeO_3$ film processed at elevated temperatures.

Second part of the presented work focuses on the potential of aqueous chemical solution deposition to obtain $BiFeO_3$-$CoFe_2O_4$ and $BaTiO_3$-$CoFe_2O_4$ composite multiferroics in which ferroelectric and magnetic materials coexist as separate phases in self-assembled heterostructures. For this study, $BiFeO_3$ and $BaTiO_3$ are chosen for their ferroelectric properties and lead-free content, while $CoFe_2O_4$ exhibits good magnetic properties and large magnetostriction. Multimetal ion solutions as precursors for $BiFeO_3$-$CoFe_2O_4$ and $BaTiO_3$-$CoFe_2O_4$ composites were deposited onto single crystal (001) LAO and (001) STO substrates. Spontaneous phase separation during annealing resulted in the formation of two-phase systems where spinel $CoFe_2O_4$ phase is embedded in a matrix of ferroelectric perovskite phase. While the perovskite phase growth follows the substrate, the CFO nucleates and grows onto perovskite $BiFeO_3$ or $BaTiO_3$ forming blocks and particulates in the matrices, what compared to nanopillar geometry (columnar growth) is another three-dimensional form of nanocomposites.

In case of BFO-CFO composite deposited on (001) LAO substrate, epitaxial stabilization of the tetragonal-like $BiFeO_3$ phase occurs leading to coexistence of T- and R-phases in the $BiFeO_3$ film. The presence of T-phase can have great impact on piezoelectric and magnetoelectric properties of the material increasing its potential in many application fields. Detailed structural analysis of the cross section of BTO-CFO films on (001) LAO by means of STEM revealed the presence of impurity phase $Ba_2Ti_4Fe_2O_{13}$, whose formation is probably a result of phase intermixing at higher temperature.

Composite films display both ferroelectric and ferromagnetic properties. As a result of the nanoparticulate structure of the constituent phases, nanocomposite thin films show mostly isotropic magnetic properties. In the case of the BTO-CFO composite, magnetization values are comparable with the ones obtained for composites grown by other deposition techniques. On the other hand, the enhanced magnetization of the BFO-CFO composite observed by SQUID and MFM measurements suggests the presence of other magnetically active phases besides the CFO or can result from strong interface-mediated coupling between ferromagnetic and antiferromagnetic heterostructures.

With this work we showed that aqueous solution deposition applied here is a very flexible and cost-effective method for preparation of composite materials with different constituent phases. The applied deposition process gives a perspective for the development of a variety of composite materials not only in the multiferroic field but also in the wider range of metal oxide materials.

Concerning further work, it would be interesting to investigate the coupling of magnetic and electric properties in obtained composite nanostructures through measurement of the magnetoelectric coefficient. In this way, the potential of solution-derived composite could be better evaluated and compared with the composite grown by other deposition techniques.

Furthermore, the fabrication of composites with better structural and dimensional control is desired. There is a high degree of randomness in the position and size of the $CoFe_2O_4$ blocks and grains embedded in perovskite matrix. On the other hand, highly ordered multiferroic arrays could be achieved by nucleation induced self-assembly where the growth of magnetic phase would be ordered for a large area. For this purpose the $CoFe_2O_4$ nucleation centers

should be deposited on the single crystal substrate prior to the deposition of composite solution precursor. Ordered $CoFe_2O_4$ nanoparticles as nucleation centers could be synthesized and deposited using block-copolymer based micelles. This approach was used in our group for the synthesis and deposition of various metal or metal-oxide nanoparticles with a good hexagonal order. In this way, since the deposited nanoparticles are the seeds for nucleation and growth of the $CoFe_2O_4$ crystallites it may be possible to decrease the annealing temperature and prevent intermixture of the constituent phases, especially for the BTO-CFO composites. Finally, highly ordered multiferroic arrays of CFO crystallites in the perovskite matrix would facilitate the study on interfacial phenomena and related magnetoeletric properties.

Nederlandstalige samenvatting

Magnetoelektrische multiferroïcs zijn materialen waarbij gelijktijdig een ferro elektrisch en (anti)ferro magnetisch moment optreedt en waarbij er een koppeling is tussen beide momenten zodat de magnetisatiegraad met een extern elektrisch veld kan gecontroleerd worden en de polarisatiegraad met een extern magnetisch veld. Daarom zijn deze materialen erg interessant voor toepassingen in multifunctionele onderdelen waar één enkel element verschillende taken moet kan vervullen, hetgeen dan leidt tot miniaturisatie van elektronica in combinatie met verhoogde prestaties. In de uitdaging om multiferroïsche materialen te ontwikkelen op kamertemperatuur heeft het onderzoek twee richtingen genomen. De eerste richting spits zich toe op de intrinsieke enkelfasige multiferroïca waar dunne films bestaande uit bismut ferraat ($BiFeO_3$) zeer veelbelovend zijn. De tweede richting ontwikkelt composiet multiferroïca met aparte ferro elektrische en magnetische fasen. Bismut ferraat kent echter problemen naar fasevorming, fasezuiverheid en temperatuursstabiliteit die een negatieve invloed hebben naar de uiteindelijke materiaaleigenschappen en de toepassingsgeschiktheid van het gesynthetiseerde materiaal. Bovendien is het aantal alternatieven voor enkelfasige intrinsieke multiferroïcs die actief zijn bij kamertemperatuur zeer schaars zodat steeds meer nadruk komt te liggen op het ontwikkelen van nieuwe composieten en nieuwe mengstructuren met verbeterde magnetoelektrische eigenschappen.

In deze thesis wordt uitgegaan van waterige oplossingen als goedkoop en milieuvriendelijk alternatief voor de afzetting van dunne films van bismut ferraat alsook van composieten. In het eerste deel van het project ligt de nadruk op het begrijpen van de invloed van de verschillende procesparameters en het onderliggende substraat op de fasenvorming en temperatuursstabiliteit van de $BiFeO_3$ dunne films. In het tweede deel worden composietstructuren gecreëerd met behulp van zelfassemblage en de flexibiliteit van natchemische depositie en wordt het potentieel van natchemisch gedeponeerde nanostructuren in de multiferroïca onderzocht.

Hoofdstuk 3 handelt over de invloed van verschillende procesparameters op de thermische stabiliteit van $BiFeO_3$ dunne films verkregen door natchemische depositie op geplatineerde silicium substraten. Anneal temperatuur en duur, filmdikte, bismut overmaat en vervanging van ijzer door titanium hadden elk een verschillend effect op de vorming van een secundaire fase door ontbinding van het $BiFeO_3$. Eerste aanwijzingen voor thermische instabiliteit waren er vanaf 650°C door de vorming van microstructurele inhomogeniteiten. Vanaf 700°C vormde zich een beduidende hoeveelheid ijzer rijk $Bi_2Fe_4O_9$ als secundaire fase door decompositie van het $BiFeO_3$. $Bi_2Fe_4O_9$ korrels waren ingekapseld in een matrix van $BiFeO_3$ en ontstonden steeds aan de grens tussen de film en het onderliggende substraat. Zij groeiden naar het oppervlak van de film toe door depletie van de omliggende $BiFeO_3$ matrix en hun vorm en grootte was afhankelijk van de gedeponeerde filmdikte. De bekomen resultaten wijzen op een verlies van bismut in de film bij hogere temperaturen. Dit is mogelijk door verdamping maar ook door diffusie naar het onderliggende substraat en reactie met het platina daar. De vorming van een bismut rijke laag onder het platina tijdens annealen van een zuivere bismut film bewijst dat het bismut bij hogere temperaturen in het substraat diffundeert.

Om de ontbinding van $BiFeO_3$ tot de ijzer rijke nevenfase tegen te gaan is het dus zaak het verlies van bismut in de films door verdamping of diffusie zoveel mogelijk te beperken. Daarom zijn kortere annealtijden en het gebruik van een 30 mol% overmaat aan bismut in de precursoroplossing mogelijke oplossingen. Een andere aanpak om de stabiliteit van de $BiFeO_3$ film te verhogen is het vervangen van het ijzer door aliovalent titanium omdat dan diffusie van het bismut waarschijnlijk verhinderd wordt doordat er minder zuurstofvacatures gevormd worden of zelfs door precipitatie van het titanium op nanoschaal. Deze bevindingen zijn niet enkel geldig voor andere dunne films met bismut houdende componenten, maar voor alle films die elementen bevatten met een hoge diffusiecoëfficiënt waarbij controle over de fasevorming cruciaal is.

In hoofdstuk 4 wordt dieper ingegaan op de invloed van verschillende substraten en bufferlagen. Hier wijst het gebruik van silicium substraten, monokristallijne substraten en substraten met bufferlagen op twee tegenstrijdig aspecten van de film-substraat interactie van $BiFeO_3$ films indien zij bij hoge temperatuur

behandeld worden. Een eerste aspect is gerelateerd aan de ontbinding van het $BiFeO_3$ op silicium substraat dat soms zo uitgesproken is dat er geen $BiFeO_3$ meer gedetecteerd wordt in de uiteindelijke film. Daardoor bestaat de film voornamelijk uit secundaire fases die, afhankelijk van het gebruikte type silicium substraat, in meerdere of mindere bestaan uit de reactieproducten uit de interactie tussen de film en het substraat. In het geval van monokristallijne substraten zoals (001) $LaAlO_3$ of (001) $SrTiO_3$ daarentegen werd geen ontbinding van de $BiFeO_3$ laag waargenomen. Bovendien vertoonde de afgezette film een hoge graad van epitaxie met een (001) oriëntatie. De $BiFeO_3$ fase wordt in deze gevallen gestabiliseerd doordat de film en het onderliggende substraat een gelijkaardige kristalstructuur en roosterparameters hebben. De films vertonen een zwakke ferromagnetische respons van ongeveer 2 tot 3 emu/cm^3 bij kamertemperatuur hetgeen karakteristiek is voor $BiFeO_3$ films met geïnduceerde expitaxiale spanning. Daarenboven duiden de magnetische metingen op de afwezigheid van secundaire fasen door een sterke magnetische respons. Betreffende het gebruik van bufferlagen werd vastgesteld dat een TiO_2 bufferlaag een sterke neiging heeft tot interactie met de $BiFeO_3$ film, terwijl de film op perovskiete bufferlagen zoals $BaTiO_3$ en $SrTiO_3$ wel goed behouden blijft. Als conclusie kan men stellen dat structurele overeenkomsten tussen film en substraat en chemische compatibiliteit wenselijk zijn en dus nagestreefd moeten worden bij de substraatkeuze voor het afzetten van $BiFeO_3$ films behandeld bij hoge temperaturen.

Het tweede deel van dit werk focust op het potentieel van waterige chemische oplossingsdepositie om $BiFeO_3$-$CoFe_2O_4$ and $BaTiO_3$-$CoFe_2O_4$ composiete multiferroïcs te creëren waarin ferroelektrische en magnetische materialen gecombineerd worden tot heterostructuren met behulp van zelfassemblage. Voor dit onderzoek worden $BiFeO_3$ and $BaTiO_3$ gekozen voor hun ferroelektrische eigenschappen en omdat ze loodvrij zijn, terwijl $CoFe_2O_4$ goede magnetische eigenschappen vertoont en een grote magnetostrictie. Oplossingen van multimetaal ionen werden afgezet op monokristallijne (001) $LaAlO_3$ en (001) $SrTiO_3$ substraten als precursoren van $BiFeO_3$-$CoFe_2O_4$ en $BaTiO_3$-$CoFe_2O_4$ composieten. Tijdens het annealen trad spontane fase ontbinding waardoor een tweefasig systeem gevormd werd bestaande uit een spinelstructuur van $CoFe_2O_4$ die ingebed was in een ferroelektrische perovskiet fase. De groei van de

167

perovskiet fase volgt het substraat, terwijl het cobalt ferriet nucleëert op de perovskiet fase en daarin geïsoleerde partikels vormt.

In het geval van $BiFeO_3$-$CoFe_2O_4$ composieten gedeponeerd op een (001) $LaAlO_3$ wordt epitaxiale stabilisatie waargenomen van de $BiFeO_3$ fase hetgeen leidt tot co-existentie van T en R fases in de film. De aanwezigheid van deze T fase heeft een grote impact op de piezoelektrische en magnetoelektrische eigenschappen van deze films hetgeen de toepassingsmogelijkheden sterk verhoogt. Een gedetailleerde structuuranalyse met behulp van STEM toont de aanwezigheid aan van de nevenfase $Ba_2Ti_4Fe_2O_{13}$. Deze ontstaat waarschijnljk door reactie tussen beide primaire fasen bij hogere temperatuur.

De composietfilms vertonen zowel ferroelektrische als ferromagnetische eigenschappen. Als gevolg van de nanopartikelstructuur van de $CoFe_2O_4$ fase zijn de magnetische eigenschappen van de dunne film isotropisch. In het geval van de $BaTiO_3$-$CoFe_2O_4$ composieten worden magnetisatiewaarden gemeten gelijkaardig aan deze bekomen door het composiet op andere manieren af te zetten. Anderzijds vertoont het $BiFeO_3$-$CoFe_2O_4$ composiet wel een verhoogde magnetisatie wanneer gemeten met SQUID of MFM. Dit suggereert de aanwezigheid van bijkomende magnetische fases naast het $CoFe_2O_4$ mar kan ook het gevolg zijn van een sterke koppeling tussen de ferromagnetische en antiferromagnetische heterostructuren door hun groot interfaseoppervlak.

Met dit onderzoek werd aangetoond dat natchemische depositie een flexibele en kostenbesparende methode is voor de bereiding en afzetting van composietmaterialen bestaande uit verschillende fasen. The gebruikte depositietechnieken bieden perspectieven voor de ontwikkeling van een hele waaier aan composietmaterialen, die zich niet enkel beperkt tot de multiferroïcs maar het hele gebied van de metaaloxide materialen omvat.

In de toekomst is het zeker interessant het koppelingsmechanisme tussen de magnetische en de elektrische eigenschappen in composieten verder te onderzoeken door metingen van de magnetoelektrische coëfficiënt. Op deze manier zou met de natchemische depositie als techniek beter kunnen vergelijken met de andere depositietechnieken voor composietmaterialen.

Bovendien moeten de structuur en dimensies van de composieten nog beter controleerbaar worden. Er is nog een hoge mate van willekeur in de plaats en grootte van de $CoFe_2O_4$ korrels in de perovskiet matrix. Sterker geordende arrays zouden geïnduceerd kunnen worden met behulp van zelfassemblage waarbij de groei van de magnetische fase gecontroleerd zou kunnen worden over een groot oppervlak. Daarom zouden eerst $CoFe_2O_4$ nucleatiekiemen gedeponeerd moeten worden op het monokristallijne substraat alvorens de depositie van de composiet precursor plaatsheeft. Met het gebruik van blokcopolymeermicellen kunnen nanodeeltjes in een vast patroon gedeponeerd worden en dienst doen als kiem. Deze methode werd reeds in onze groep gebruikt voor de synthese en geordende depositie van verschillende metaal en metaaloxide nanodeeltjes. Op deze manier kan de annealtemperatuur waarschijnlijk verlaagd worden aangezien er dan reeds kiemen aanwezig zijn voor de groei van de $CoFe_2O_4$ fase. Dit voorkomt dan waarschijnlijk ook de nevenreacties voor de $BaTiO_3$-$CoFe_2O_4$ composieten. Tenslotte zal een hooggeordende multiferroïsch array van $CoFe_2O_4$ kristallieten in de perovskiet matrix de studie van interfase fenomenen en de daaraan gerelateerde magnetoelektrische eigenschappen vergemakkelijken.

Scientific contributions

Publications

N. Pavlovic, J. D'Haen, H. Modaressi, A. Riskin, C. De Dobbelaere, M.J. Van Bael, K. Temst, A. Hardy, M.K. Van Bael, $BiFeO_3$ thin films via aqueous solution deposition: a study of phase formation and stabilization, Journal of Materials Science 50 (2015) 4463-4476

N. Pavlovic, H. Modarresi, J. D'Haen, C. De Dobbelaere, K. Temst, A. Hardy, M. K. Van Bael, Influence of the substrate on the phase formation and thermal stability of BFO thin films. Manuscript in preparation.

N. Pavlovic, R. Paria, A. Volodin, Q. Qin, J. D'Haen, A. Riskin, S. van Dijken, J. Hadermann, A. Hardy, M.K. Van Bael, Self-assembled multiferroic nanostructured composites by ACSD. Manuscript in preparation.

Oral presentations

N. Pavlovic, C. De Dobbelaere, J. D'Haen, A. Hardy, M.K. Van Bael, Thermal stability and phase formation of $BiFeO_3$ films, EMF 12, Bordeaux, France, 26 jun-02 july 2011.

N. Pavlovic, C. De Dobbelaere, J. D'Haen, A.M. Abakumov, J. Hadermann, A. Hardy, M. Van Bael, $BiFeO_3$ films: evolution of phase formation, COST SIMUFER, Bordeaux, France, 30 jun-01 july 2011

N. Pavlovic, C. De Dobbelaere, N. Peys, J. D'Haen, A. Volodin, C. Van Haesendonck, A. Hardy, M.K. Van Bael, $BiFeO_3$ thin films: between decomposition and phase stability, ESR COST SIMUFER, Novi Sad, Serbia, 16-18 november 2011

S. Gielis, N. Peys, D. Dewulf, C. De Dobbelaere, **N. Pavlovic**, S. Van Elshocht, S. De Gendt, P.M. Vereecken, A. Hardy, M.K. Van Bael , Aqueous chemical solution deposition of LuFeO3 thin films in view of energy storage applications, ESR COST SIMUFER, Novi Sad, Serbia, 16-18 november 2011

N. Pavlovic, C. de Dobbelaere, J. D'Haen, A. Hardy, M.K. Van Bael, Influence of different substrates on phase stability of $BiFeO_3$ thin films obtained by aqueous solution deposition, ISAF ECAPD PFM 2012, Aveiro, Portugal, 9-13 July 2012

C. De Dobbelaere, **N. Pavlovic**, A. Hardy, M. Van Bael, Ferroelectrics from Aqueous Chemical Solution Deposition, MS&T'12, Pittsburgh, USA, 7-11 October 2012

N. Pavlovic, Q. Qin, J. D'Haen, C. De Dobbelaere, A. Riskin, S. van Dijken, A. Hardy, M.K. Van Bael, Self-assembled $BaTiO_3$-$CoFe_2O_4$ and $BiFeO_3$-$CoFe_2O_4$ film composites: structural and magnetic studies, ESR COST SIMUFER, Novi Sad, Serbia, 06-09 november 2013

N. Pavlovic, H. Modarresi, J. D'Haen, C. De Dobbelaere, K. Temst, A. Hardy, M.K. Van Bael, Phase formation control in $BiFeO_3$ films through substrate selection, COST SIMUFER Final Worshop, Genoa, Italy, 30 January -1 February 2014

N. Pavlovic, R. Paria, H. Modarresi, Q. Qin, J. D'Haen, C. De Dobbelaere, A. Riskin, S. van Dijken, K. Temst, J. Hadermann, A. Hardy, M.K. Van Bael, Multiferroic thin films and self-assembled heterostructures via solution-gel chemistry, Electroceramics14, Bucharest, Romania, 16-20 June 2014

S. Gielis, M. Ivanov, N. Peys, J. van den Ham, **N. Pavlovic**, P. Robaeys, M. Nesladek, J. Banys, A. Hardy, Marlies K. Van Bael, Aqueous chemical solution deposition of $LuFeO_3$ ultra high-k films, 39th ICACC, Daytona Beach, Florida, USA, 25 – 30 January 2015

Poster presentations

N. Pavlovic, C. De Dobbelaere, A.M. Abakumov, J. Hadermann, A. Hardy and M.K. Van Bael, Phase formation in the perovskite-based bismuth- and lead-ferrite obtained by the aqueous solution-gel route, COST SIMUFER, Edinburgh, Scotland, 12-13 August, 2010

N. Pavlovic, C. De Dobbelaere, J. D'Haen, D. Batuk, A.M. Abakumov, J. Hadermann, A. Hardy, M. Van Bael, Phase formation in bismuth- and lead ferrite films obtained by chemical solution deposition, COST SIMUFER, Hasselt, Belgium, 21-23 March, 2011

M. Menghini, **N. Pavlovic**, B. Ydens, S. Thayumanasundaram, V. S. Rangasamy, C. De Dobbelaere, A. Hardy, M. K. van Bael, J. P. Locquet, Oxide nanostructures by soft e-beam lithography, E-MRS 2011 spring meeting, Nice, France, 9-13 May, 2011

N. Pavlovic, C. De Dobbelaere, N. Peys, J. D'Haen, A. Volodin, C. Van Haesendonck, A. Hardy, M.K. Van Bael, From aqueous solution to multiferroic thin films, E-MRS 2011 fall meeting, Warsaw, Poland, 19-22 September, 2011

S. Gielis, N. Peys, D. Dewulf, C. De Dobbelaere, **N. Pavlovic**, H. Damm, S. Van Elshocht, S. De Gendt, P. M. Vereecken, A. Hardy, M.K. Van Bael, Aqueous chemical solution deposition of $LuFeO_3$ thin films in view of energy storage applications, E-MRS 2011 fall meeting, Warsaw, Poland, 19-22 September, 2011

N. Pavlovic, C. De Dobbelaere, J. D'Haen, A. Hardy, M.K. Van Bael, Structural and microstructural changes in $BiFeO_3$ films by varying processing parameters, ESMF 2012, Ascona, Switzerland, 29 January -3 February, 2012

N. Pavlovic, C. De Dobbelaere, J. D'Haen, A. Hardy, M.K. Van Bael, 'Stability windows' for bismuth ferrite thin films, COST SIMUFER Workshop, Vilnius, Lithuania, 23 April, 2012

N. Pavlovic, H. Modarresi, C. De Dobbelaere, J. D'Haen, K. Temst, A. Hardy, M.K. Van Bael, Effect of perovskite-based buffer layers on phase stability of $BiFeO_3$ thin films, Annual meeting of the Belgian Ceramic Society, Diepenbeek, Belgium, 19 April, 2013

S. Gielis, N. Peys, **N. Pavlovic**, S. Van Elshocht, S. De Gendt, A. Hardy, M.K. Van Bael, Aqueous chemical solution deposition of $LuFeO_3$ thin high-k films, Annual meeting of the Belgian Ceramic Society, Diepenbeek, Belgium, 19 April, 2013

N. Pavlovic, C. De Dobbelaere, J. D'Haen, A. Hardy, M.K. Van Bael, Multiferroic nanocomposite films from aqueous solutions, COST SIMUFER Workshop, Faenza, Italy, 22-23 April, 2013

E. Peeters, C. De Dobbelaere, H. Damm, K. Schellens, **N. Pavlovic**, A. Hardy and M. K. Van Bael, Exploration of single-phase layered perovskites as candidate magnetoelectrics, COST SIMUFER Workshop, Faenza, Italy, 22-23 April, 2013

K. Chybczyńska, B. Andrzejewski, B. Hilczer, M. Matczak, **N. Pavlovic**, M. van Bael, A. Hardy, B. Łęska, R. Pankiewicz, Microwave- hydrothermal synthesis vs hydrothermal synthesis of $BiFeO_3$ micro and nanostructures, 13th International Meeting on Ferroelectricity – IMF-13, Krakow, Poland, 2-6 September, 2013

N. Pavlovic, C. De Dobbelaere, J. D'Haen, A. Hardy, M.K. Van Bael, Self-assembled epitaxial composite films of $BaTiO_3$-$CoFe_2O_4$ and $BiFeO_3$-$CoFe_2O_4$ from aqueous solutions, MS&T'13, Montreal, Canada, 27-31 October, 2013

R. Paria, **N. Pavlovic**, A. Hardy, M.K. Van Bael, J. Hadermann, G. Van Tendeloo, Electron Crystallography School – Introduction to electron diffraction tomography, TEM investigation of multiferroic compounds: $LaAlO_3$//$BaTiO_3$/$CoFe_2O_4$ and $LaAlO_3$//$BiFeO_3$/$CoFe_2O_4$, Darmstadt, Germany, 7-11 April, 2014

N. Pavlovic, R. Paria, Q. Qin, J. D'Haen, C. De Dobbelaere, A. Riskin, S. van Dijken, J. Hadermann, A. Hardy, M.K. Van Bael, Multiferroic heterostructures from aqueous solution processing, COST Action SIMUFER Showcase, Electroceramic14, Bucharest, Romania, 16-20 June, 2014
POSTER AWARD

K. Chybczyńska, B. Andrzejewski, B. Hilczer, M. Matczak, **N. Pavlovic**, M. Van Bael, A. Hardy, Influence of the different synthesis methods on the magnetic properties of micro-and nanostructures of $BiFeO_3$, Electroceramics14, Bucharest, Romania, 16-20 June, 2014

H. Modarresi, E.M. Dalmau, M.K. Van Bael, M.J. Van Bael, K. Temst, A. Vantomme, V. Lazenka, **N. Pavlovic**, M. Bisht, M. Lorenz, M. Grundmann, A. Hardy, Ion-induced coercivity enhancement in $BiFeO_3$, 19th International Conference on Ion Beam Modification of Materials - IBMM2014, Leuven, Belgium, 14-19 September, 2014